FLASH SINTERING OF ZINC OXIDE AND THE GROWTH OF ITS NANOSTRUCTURES

by

Xin Li Phuah

A Dissertation

Submitted to the Faculty of Purdue University

In Partial Fulfillment of the Requirements for the degree of

Doctor of Philosophy

School of Materials Engineering

West Lafayette, Indiana

August 2021

THE PURDUE UNIVERSITY GRADUATE SCHOOL
STATEMENT OF COMMITTEE APPROVAL

Dr. Haiyan Wang, Chair
School of Materials Engineering

Dr. R. Edwin Garcia
School of Materials Engineering

Dr. Rodney Trice
School of Materials Engineering

Dr. Xinghang Zhang
School of Materials Engineering

Approved by:
Dr. David Bahr

ACKNOWLEDGMENTS

Firstly, I would like to thank my advisor, Dr. Haiyan Wang, for all her guidance and support for my PhD studies. I would also like to thank my committee members, Dr. Edwin García, Dr. Rodney Trice and Dr. Xinghang Zhang, for their valuable support and encouragement throughout my graduate studies. The research was made possible by funding from the Office of Naval Research from the support of Dr. Antti Makinen under contract numbers N00014-17-1-2087 and N00014-20-1-2043.

I would like to thank my team members, including Dr. Han Wang, Dr. Jaehun Cho, Bo Yang, Dr. Zhongxia Shang, Dr. Sichuang Xue, Dr. Jin Li and Dr. KSN Vikrant. Their assistance and support have allowed the completion of many of my published work. I would also like to thank my external collaborators, Dr. Harry Charalambous, Dr. Shikhar Jha, Kent Christian, and Dr. Thomas Tsakalakos from Rutgers University, Dr. Amiya K. Mukherjee at UC Davis and Dr. Steve Hellberg and Dr. Noam Bernstein at Naval Research Lab.

I would like to acknowledge Dr. Wolfgang Rheinheimer for his extremely helpful discussions during his time as a visiting professor at Purdue University. I also want to thank Dr. John Blendell for being my mentor during my teaching assistantship and providing endless valuable advice for my graduate studies. I am also thankful for all my fellow current and former group members in the Wang Thin Film group for their support. My deepest gratitude goes to my parents and family who have always supported my career path.

TABLE OF CONTENTS

LIST OF TABLES

LIST OF FIGURES

ABSTRACT

Flash sintering was first demonstrated in 2010, where a ceramic green body was rapidly densified within seconds by applying an electric field during the heating process. The ultra-fast densification can occur as current abruptly flows through the material and self-heats by Joule heating. This process has potentials for large energy savings due to the reduction in furnace temperatures and shortened sintering time compared to conventional sintering. In addition, the ultra-high heating and cooling rates, along with the impact of electric field and current leads to the formation of unique non-equilibrium features in ceramics, which could greatly enhance their properties. Despite the potential of flash sintering, there are many challenges in moving this technique towards practical applications, such as the microstructure inhomogeneity and lack of understanding of the defects characteristics.

In this dissertation, flash sintering was performed on ZnO to investigate the influence of various electrical conditions on the microstructure and defects. Detailed characterization was performed on flash sintered ZnO with and without a controlled current ramp, and contrasting types of current (DC and AC). These parameters show significant impact on the gradient microstructure and defects, and provide a way to tailor the desired characteristics for a wide range of applications. On the other hand, flash sintering of ZnO performed with a high electric field and low current density resulted in the growth of nanostructures. These nanostructures are unique compared to other growth techniques as they contain high density basal-plane stacking faults, and exhibit ultraviolet excitonic emission and red emission at room temperature. The nanostructure growth mechanism was investigated by varying the current density limit and revealed the formation of liquid phases which allowed growth by the vapor-liquid-solid mechanism. These findings present

a new exciting route for flash sintering to produce highly defective nanostructures for device applications with new functionalities.

CHAPTER 1. INTRODUCTION

Ceramics are highly desirable materials for a wide range of applications as they have excellent mechanical strength and chemical inertness. However, their high melting points and brittle characteristics make processing of ceramics extremely challenging and costly compared to metals and polymers. They usually require a high temperature thermal treatment process, known as sintering, to transform a packed powder compact into a dense bulk form which is mechanically strong enough for applications. Sintering has existed since the prehistoric era of civilization for firing pottery and it is one of the oldest human technologies. Till now, sintering is still a highly important process to produce traditional ceramics and functional ceramics for mechanical, electrical, optical, chemical, magnetic, thermal, biological, and nuclear applications.

The general steps involved in conventional dry ceramic processing are shown in Figure 1.1. The process starts from ceramic powder, which is either commercially available or synthesized from precursor materials. Typically, powder processing is a necessary step in order to modify the powder characteristics, such as the particle size, distribution and shape, and degree of agglomeration. The following step is powder compaction, where the powders are loaded into a die and pressed using uniaxial force to pack the powder as tightly as possible into a green body. Achieving a high green body density is desirable as it will ease the removal of any remaining porosity in the next and final step, i.e., the sintering process. Sintering transforms the green body into a dense ceramic by heating in a furnace. This process involves high furnace temperatures and long holding time to provide thermal energy for mass transport via diffusional processes. Although this is a technically simple process, it can be challenging to find the right sintering conditions due

to various competing diffusion mechanisms. Thus, sintering has been extensively studied as it is the most critical step to achieve the desired final microstructure and properties of ceramics.

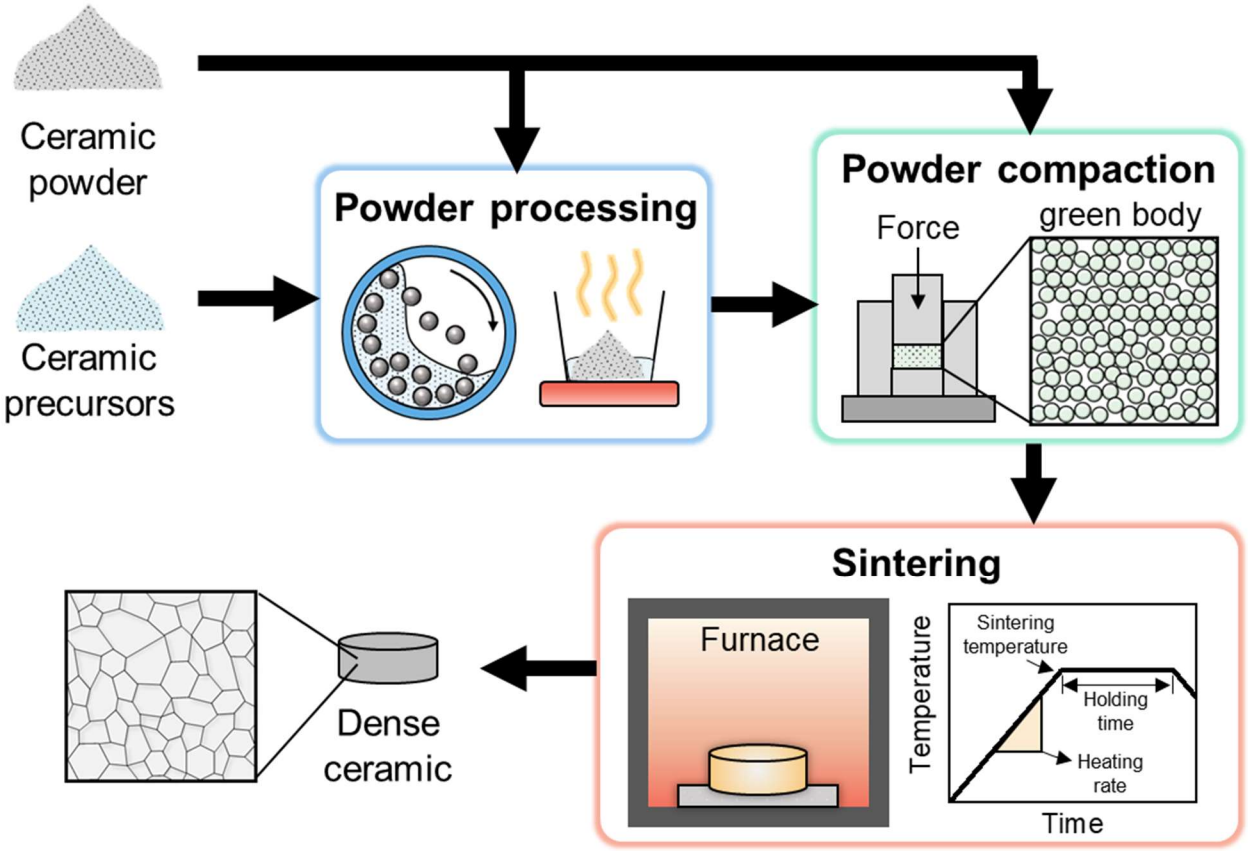

Figure 1.1 Steps in conventional ceramic processing.

There are two main types of sintering process: solid state sintering and liquid phase sintering. Solid state sintering refers to the transformation of the powder compact into its dense state purely in solid state, while liquid phase sintering requires a liquid phase present in the powder compact which will aid the sintering process. As the dissertation work pertains to solid state sintering, sintering will always be referred to as solid state sintering here after. In this introduction chapter, the fundamentals of sintering are presented along the advancement of sintering techniques. This background will provide useful information in understanding flash sintering, the main focus of the dissertation, which will be reviewed in Chapter 2.

1.1 Sintering and grain growth

The goal of the sintering process is to densify the material, or in other words, remove the porosity from the material. By providing thermal energy, mass transport can occur by diffusion of atoms, ions and other charged species through various pathways [1], as shown in Figure 1.2. In order for densification to occur, mass needs to be transported from the bulk or grain boundaries to the pores, which results in sample shrinkage. This primarily occurs through lattice and grain boundary diffusion, and less often plastic flow through dislocations. However, it is also possible to move mass along the grain boundaries or surfaces through lattice or surface diffusion, and vapor transport. Since these processes are not moving mass to the pore regions, they are non-densifying mechanisms and result in coarsening. Both densification and coarsening mechanisms actively occur simultaneously during sintering and the final microstructure usually results in a dense microstructure with grain growth.

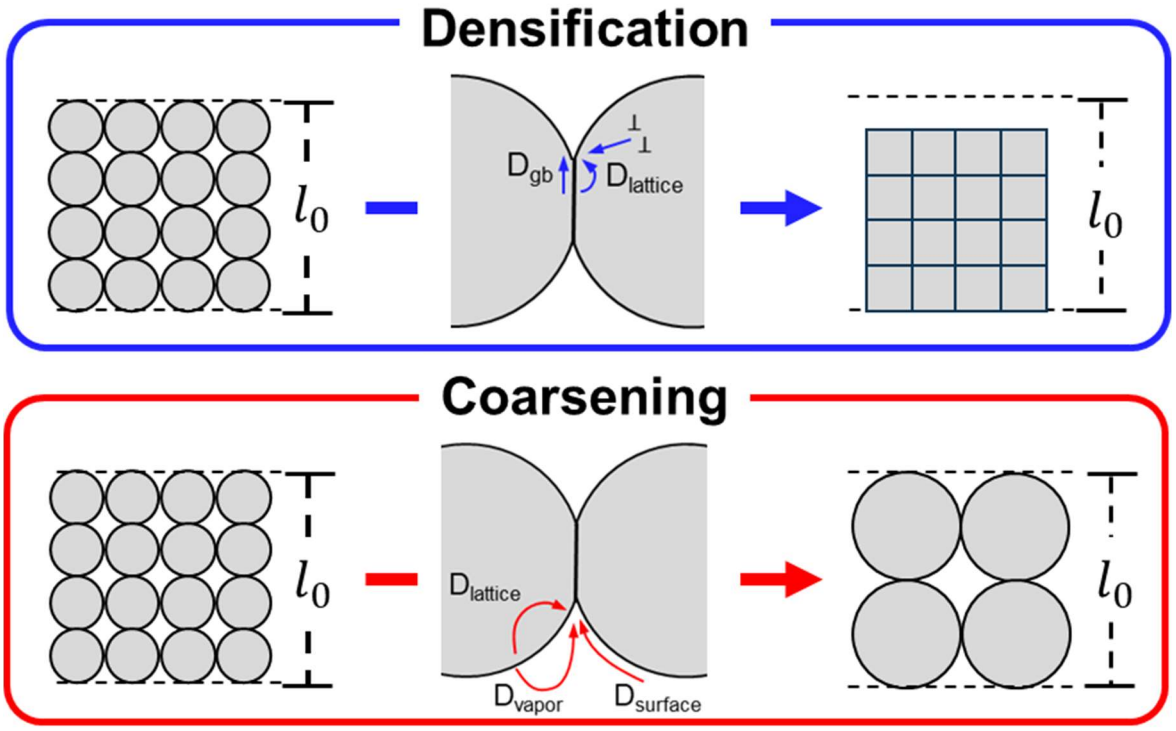

Figure 1.2 Schematic of the diffusion mechanisms involved in coarsening and densification.

To understand how the microstructure evolves during the sintering process, we must consider the thermodynamics and kinetics of the process. The thermodynamic driving force of sintering is the reduction of free energy of the system, which are provided by the curvature of the free surfaces. For both densification and coarsening mechanisms, all the diffusion processes offer a way to minimize the free energy by reducing the surfaces or interface areas, or forming necks between the particles. On the other hand, the kinetics determine if the process can be completed within reasonable magnitude of time. This is dependent on the rate of diffusion, and the type and concentration of defects in the solid. Hence, it is important to maximize the driving force and rate of the process by adjusting the sintering variables, which will be discussed next.

1.2 Sintering variables

Due to the interplay of multiple diffusion mechanisms, ceramic systems have to be meticulously studied through the process parameters. The final goals would vary between different applications, but most often, a dense microstructure with a fine grain size is desired. There are many sintering variables which can be modified, starting from the raw material itself. The most common sintering variables are summarized in Figure 1.3 and can be categorized as a material or process variable.

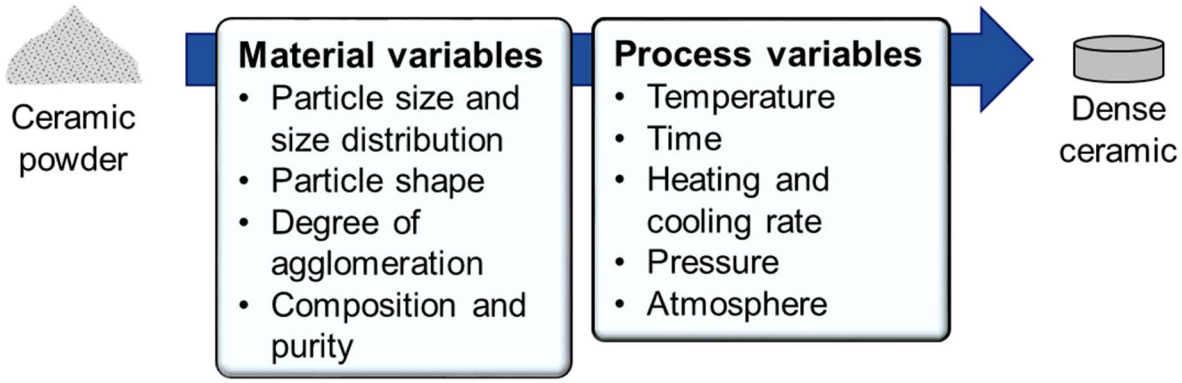

Figure 1.3 Sintering variables categorized as material or process variables.

While process variables directly impact the sintering process, material variables can also significantly impact the powder packing before sintering and the sinterability of the material. One of the most critical material variables is particle size, as it determines the initial surface energy. Starting with nanosized powder will provide a larger surface energy as driving force compared to micrometer powders. Additionally, having high surface areas will result in higher concentration of defects and dangling bonds which provides enhanced atomic mobility [2]. Thus, nanosized ceramic powders are very commonly used as starting materials since they can sinter at lower

temperatures and achieve finer grain structure after sintering. It is also very important for the powder to be free from agglomeration as they can create severe inhomogeneity in the sample.

On the contrary, process variables rely primarily on the furnace heating profile. The well-studied process variables are the heating rate, sintering temperature and holding time, as they can be easily devised to modify the relative contribution of densification and coarsening. Figure 1.4 shows the relative rate of densification and coarsening mechanisms with inverse temperature [3]. In general, surface diffusion and vapor transport are dominant in the low temperature region, while grain boundary and volume diffusion are dominant in the high temperature region. Hence, densification can be maximized by reaching higher temperatures and coarsening can be minimized by reaching higher temperatures by a faster heating rate.

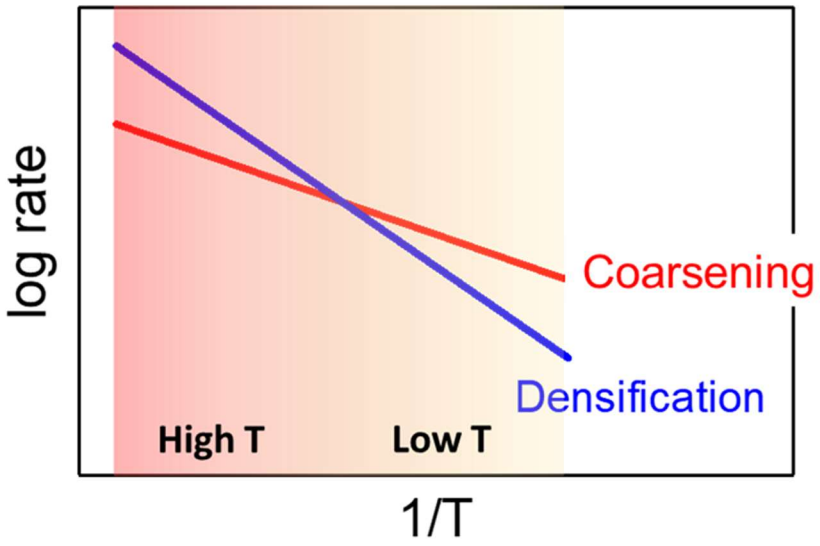

Figure 1.4 Rate of coarsening and densification vs. 1/T.

Using a faster heating rate is an effective method to prevent the initial coarsening at low temperatures and maximize the driving force for the densification process. Fast firing was proposed by Brook [4] to increase the heating rate by rapidly inserting the green body into a pre-heated furnace, and thus the heating rate is as fast as thermal conduction allows. However, thermal gradients are often observed due to low thermal conductivity of ceramics [5,6]. Another unique sintering profile is the two step sintering technique, which was first demonstrated by Chen and Wang [7]. This starts off with a high sintering temperature for a short time, followed by a lower sintering temperature for a longer time. This helps to minimize grain growth at the later stage of the sintering process which keeps the final grain sizes finer.

Although modifications to the sintering temperature profile can improve the densification process, there are still many challenges in predicting the densification behavior for each ceramic system. One of them being the densification process is driven solely by the reduction of surface energy. Thus, it will still require high sintering temperatures and several hours of holding time, which can be highly energy intensive. Moreover, the densification rate is slow, which will always contribute to unnecessary grain growth. This is what has motivated the development of advanced sintering techniques, which could densify ceramics while maintaining finer grain sizes and using a less energy intensive process.

1.3 Advancement of sintering techniques

Various new sintering techniques have been introduced and developed to improve the processing of ceramics. Figure 1.5 shows the timeline of the development of sintering techniques, where a majority of these new techniques came about recently in the past decade [8]. These techniques utilize external stress or fields, such as pressure, electric field and electric current. The

main benefit of these techniques over conventional sintering is the reduction of energy required to process the ceramics by lowering temperature and reducing sintering time. They also offer additional sintering variables, which can better control the densification process.

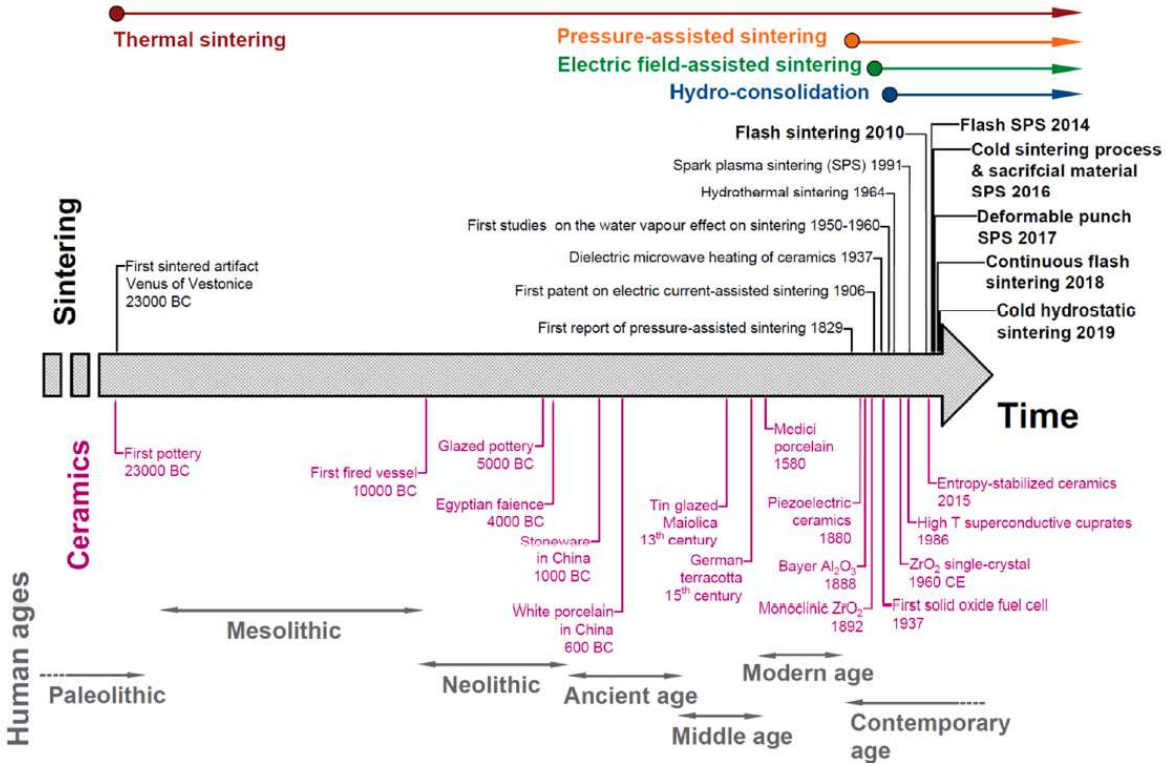

Figure 1.5 Timeline of the development of various sintering techniques. [8]

1.3.1 Pressure-assisted sintering

Using an externally applied pressure has proven to be one of the most effective techniques in reaching fully dense samples during sintering. Examples of pressure-assisted sintering techniques include hot pressing, hot isostatic pressing and sinter forging. The success of this technique in densifying ceramics is contributed largely by the applied pressure which provides an additional driving force for densification to occur without any grain growth through activated creep and plastic flow mechanisms [3]. These pressure-assisted techniques are especially beneficial for ceramic fabrication which requires full density, such as optically transparent ceramics [9–11]. This technique is also highly advantageous for materials difficult to sinter through conventional methods, such as nitrides and carbides [12,13].

Although the pressure-assisted process is extremely advantageous, there are many challenges in using the process for upscale manufacturing. Producing large scale objects would be difficult since it will require extremely high pressures for large surface areas. In addition, complex 3D-shaped components are very challenging to produce with an applied pressure. As a result, the costs to produce ceramic components through pressure-assisted processes are significantly higher compared to conventional sintering since batch processing is often limited and will require intensive post-machining to achieve the final net shape.

1.3.2 Electrically-assisted sintering

Electrically-assisted sintering is another sintering technique which can rapidly densify ceramics. The most studied electrically-assisted sintering technique is spark plasma sintering (SPS), or sometimes known as electric current-assisted sintering or pulsed electric-current sintering. This technique utilizes high electric currents to heat the die while applying a pressure

onto the powder compact. Since there is pressure involved, SPS is comparable to pressure-assisted sintering techniques, particularly hot pressing (HP). Figure 1.6(a) and (b) shows the schematics for HP and SPS techniques, respectively, where both techniques show a very similar experimental setup. The major difference between these two techniques is the heating source: SPS utilizes pulsed direct current (DC) to heat up the die which contains the powder through Joule heating, whereas HP utilizes typical furnace heating elements and heats up the entire chamber through radiation. By employing electric current, SPS is highly advantageous over HP due to its ability to achieve very high heating rates. The current can be rapidly increased to achieve heating rates up to 1000°C/min [14]. Since the powder may be conductive during the heating process, it is also possible for electric current-induced effects to occur, such as electromigration which increases point defect concentration and enhance mass transport rates [14]. However, since this process is still a primarily a pressure-assisted sintering technique, this technique has similar disadvantageous to them.

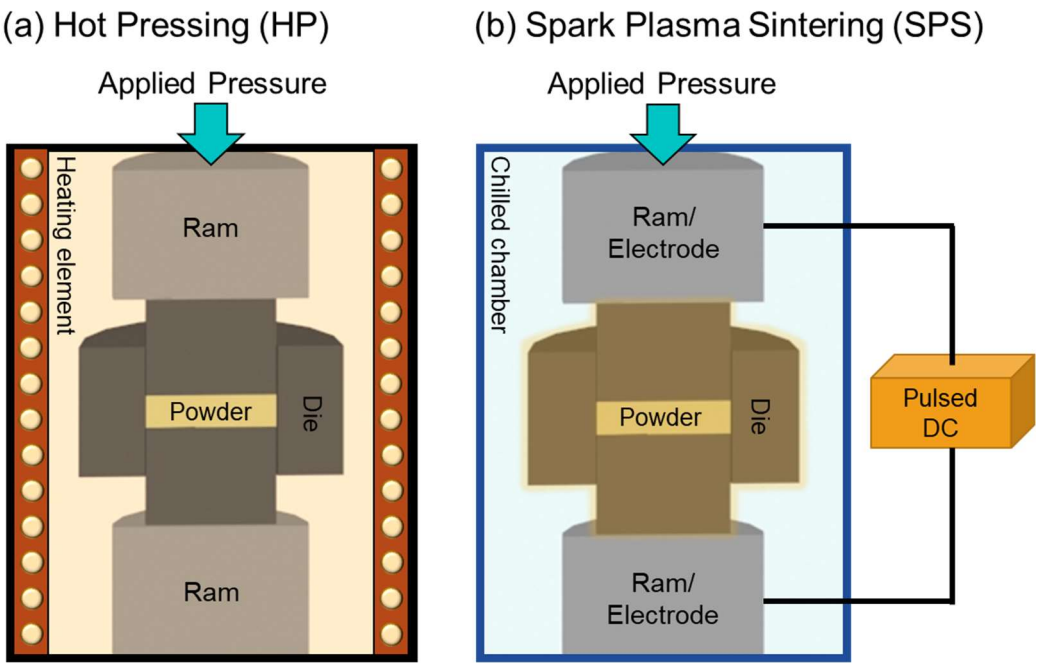

Figure 1.6 Schematics comparing (a) hot pressing (HP) and (b) spark plasma sintering (SPS) techniques.

In 2009, a study investigating the impact of a small electric field (< 20 V/cm) on microstructure evolution revealed enhancement in the rate of sintering [15]. By increasing the electric field beyond a threshold (Figure 1.7), the densification took place much more abruptly which led to the discovery of a new state-of-the-art pressureless electrically-assisted sintering called “flash sintering” in 2010 [16]. Unlike SPS, the electric current completely flows through the ceramic body, which leads to internal Joule heating (Figure 1.8). The first study of flash sintering showed rapid densification of nanograin zirconia at 850°C in < 5 s using an applied field of 120 V/cm [16]. For comparison, sintering of zirconia (3YSZ) typically requires furnace temperatures around 1100 to 1500°C for several hours [17]. This significant reduction in furnace temperature and sintering time could lead to accelerated manufacturing and potential energy savings, which presents many exciting opportunities for ceramic processing. The next chapter will review the literature on flash sintering in more details and discuss the remaining challenges.

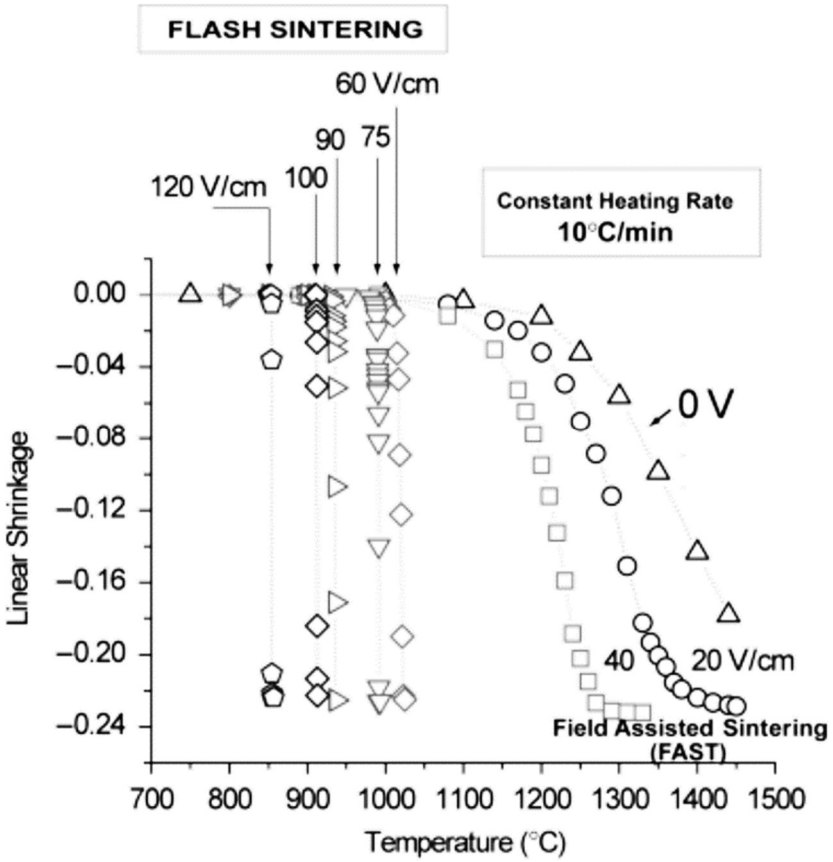

Figure 1.7 Sample shrinkage as a function of furnace temperature and electric field strength. [16]

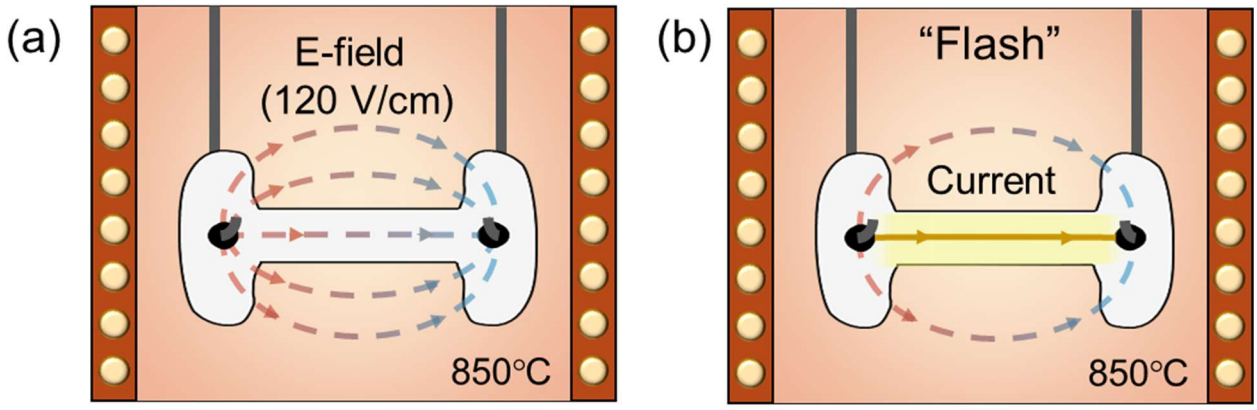

Figure 1.8 Schematic demonstrating flash sintering experiment. (a) Electric field is applied during the furnace heating process and (b) “flash” occurs when current flows through the sample.

CHAPTER 2. REVIEW ON FLASH SINTERING

Flash sintering is performed by heating a ceramic in a furnace while an electric field is applied to the sample. Since most ceramics have a negative temperature coefficient (NTC) of resistivity, ceramics become less resistive at higher temperatures and makes it is possible for ceramics to conduct current [18]. When the sample begins to conduct current, the "flash" event occurs where the sample experiences large thermal runaway due to Joule heating resistively heat the ceramics. This is accompanied by a non-linear increase in conductivity, bright light emissions and abrupt sample shrinkage within seconds.

Flash sintering has been successfully performed on a wide range of ceramic materials. Zirconia (ZrO_2) was the first material densified through this technique [16] and has led to majority of the published work based on this material (Figure 2.1). Most of the other flash sintering studies are focused primarily on oxides, including zinc oxide (ZnO) [19–40], ceria (CeO_2) [41–49], titania (TiO_2) [50–59], perovskites ($SrTiO_3$, $BaTiO_3$, $BiFeO_3$) [60–75] and alumina (Al_2O_3) [76–79]. Flash sintering has also been successfully demonstrated on various silicates [80–88], nuclear materials [89–93] and multiphase composite systems [94–97].

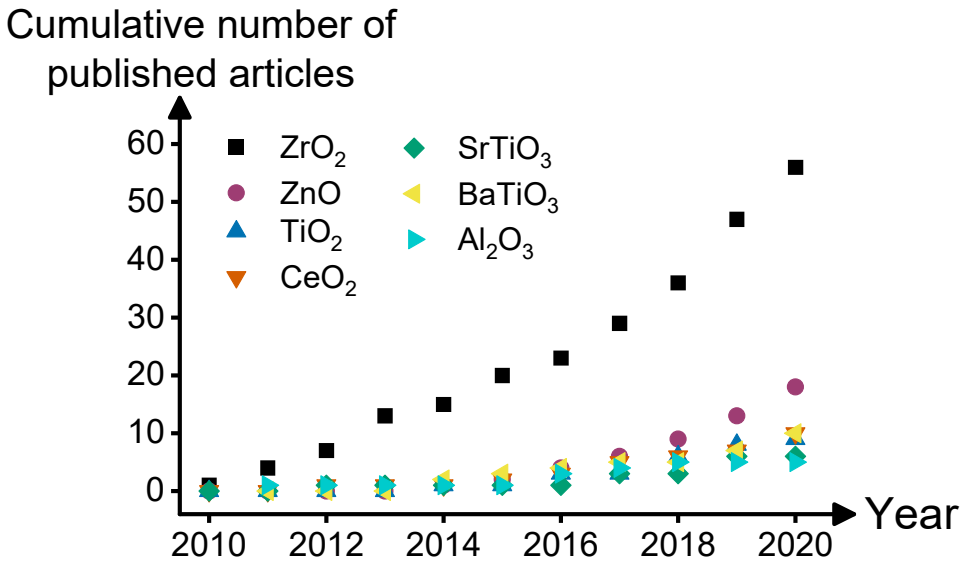

Figure 2.1 Cumulative number of published articles for the most common oxide systems studied for flash sintering.

In this review chapter, flash sintering will be discussed in several aspects, including experimental details, proposed mechanisms and characteristics of flash sintered ceramics. The goal of the review is to provide an in-depth knowledge of the current literature of flash sintering and background for the motivation of the dissertation work.

2.1 Experimental setup

There are many variations of experimental setups in order to perform flash sintering, as there are yet to be any commercial or standardized flash sintering equipment. The basic requirement to perform flash sintering would be electrical connections on the opposing ends of a ceramic sample to a power supply and it should be placed in a furnace in order to be heated. In order to obtain any data from the experiment, such as voltage, current and shrinkage, additional monitoring tools are used along with the necessary equipment. The electrical data are usually

recorded by connecting the power supply to a computer software such as LabView or an external monitoring equipment. The shrinkage can be estimated by either a charge-coupled device (CCD) camera or linear variable differential transformer (LVDT), depending on the sample geometry. Figure 2.2 shows the most commonly used sample geometry with their corresponding furnace setups.

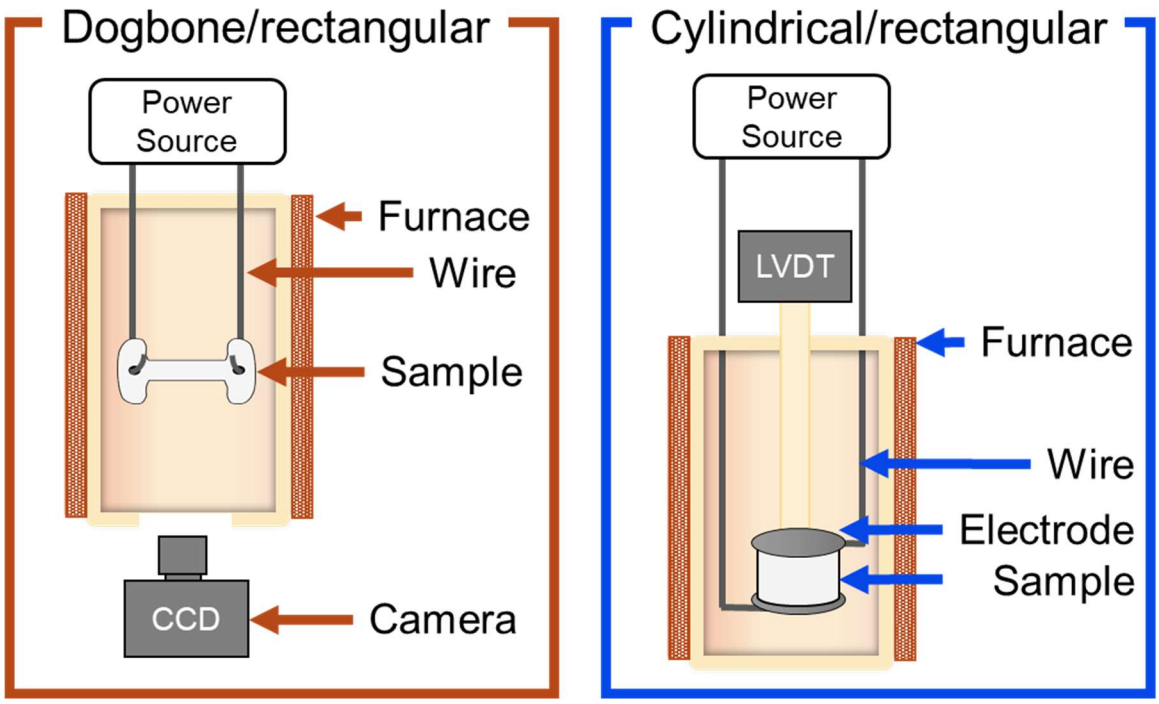

Figure 2.2 Variation of common flash sintering setups based on sample geometry.

The dogbone geometry is the most often used in flash sintering studies. A dogbone sample usually has holes at the opposite ends of the gauge area, where the wires are inserted through. This geometry is highly preferred mainly due to the reduced cross sectional area at the gauge, which helps to concentrate the flow of current through. The shrinkage is recorded using a CCD camera since the sample is suspended and the shrinkage only occurs in the gauge length. However, this geometry has no practical application, as only the neck region of the dogbone is sintered. In addition, the complex green body is difficult to produce and has no ability to scale up. Rectangular-shaped geometry can also be flash sintered using a similar setup to the dogbone sample [18,98–100]. This geometry is slightly easier to produce compared to the dogbone but still has the same limitations for practical applications.

Cylindrical samples are the most practical geometry and have been successfully flash sintered. The electrical contacts are placed on the opposing flat surfaces of the cylinder. This geometry is often used in a dilatometer which has a LVDT to track the linear shrinkage. However, having a significantly larger cross-sectional area, surface area, and volume than the other geometries makes it extremely difficult to sinter uniformly. For comparison, the cross-sectional area of typical dogbone-shaped samples (3 mm x 1.58 mm) is approximately 5 mm^2 [16], while cylindrical sample (6 mm diameter) is approximately 28 mm^2 [20]. With such a large increase in contact area, there is a very high possibility for high contact resistance and preferential current pathways to exist in cylindrical samples which can result in spikes in electrical plots and formation of voids and cracks [101,102]. In addition, surface cooling effects could be varied between sample geometries, depending on the sample surface area to volume ratio, which can result in a microstructure gradient between the surface and the core [103–106].

Besides sample geometry, there are several other considerations for the flash sintering setup, such as the type and quality of electrical contacts. Platinum (Pt) is most commonly used to provide contacts and electrical wire. Although Pt is a costly and may induce blocking effects during flash sintering, it is still the best material choice for flash sintering due to its high electrical conductivity, chemical stability and resistance to oxidation up to high temperatures. The quality of the interface between the sample and electrical contacts can also strongly impact the flash sintering process. Usually what is considered a "good" contact is when the interface has limited contact resistance and have uniform electric potential across the sample [100]. On the contrary, a "bad" contact configuration would have high contact resistance and lead to significantly inhomogeneous and asymmetric samples [100]. Most often, the quality of the contact can be improved by using conductive paste or suspension on the contact area. Careful material selection for this ink or paste is also necessary as it can play a role during the flash sintering process [77,107]. Further testing with 4-point conductivity measurements can be performed to investigate and mitigate the issue of contact resistance if necessary [108].

There are also several other modifications of flash sintering experimental setup which has been demonstrated. Figure 2.3(a) shows thermally-insulated flash sintering, where the sample is wrapped with alumina felt or embedded in a zirconia powder bed inside the furnace during flash sintering [109]. This technique was proposed to avoid excessive heat loss from the sample and has shown improvement on the sample densification process. Other modified flash sintering processes include sliding contact flash sintering (Figure 2.3(b)) [110] and contactless flash sintering FSPS (Figure 2.3(c)) [111]. Both of these techniques were proposed to improve the scalability of the process by approaching continuous flash sintering. Flash sintering has also been combined with other pressure-assisted techniques, such as sinterforging ((Figure 2.3(d)) [112] and SPS (Figure

2.3(e)) [113–117]. The hybrid flash SPS has been well-studied as it allows for flash sintering of materials which have higher conductivity, such as borides and carbides [113–117], since SPS systems have built-in high current density and low voltages.

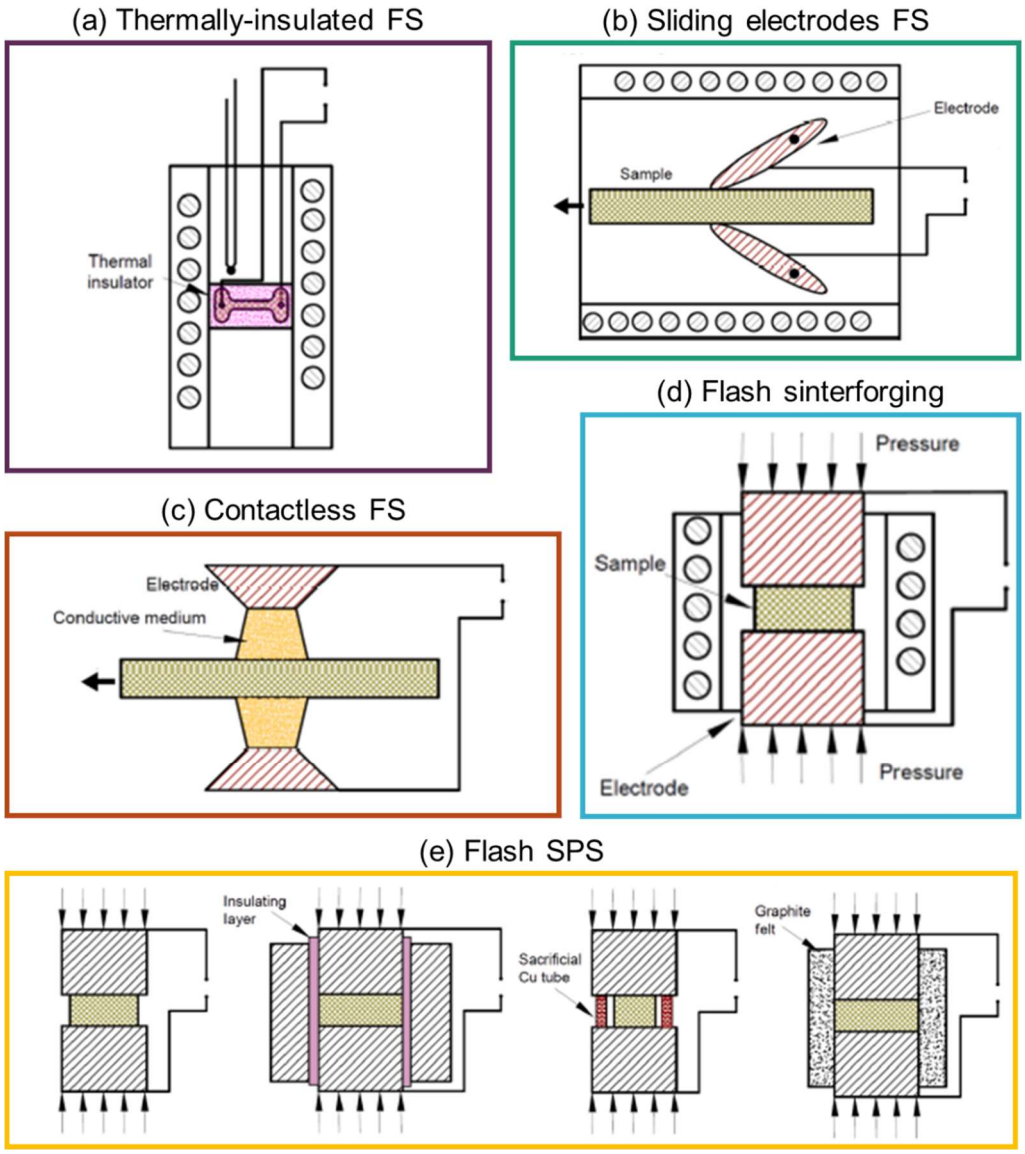

Figure 2.3 Schematic of modified flash sintering (FS) processes: (a) Thermally-insulated FS, (b) sliding electrodes FS, (c) contactless FS, (d) flash sinterforging and (e) flash spark plasma sintering. [8]

2.2 Three stages of flash sintering

The flash sintering process can be explained in three main stages [118]. Figure 2.4 shows the electrical plots corresponding to the three stages of flash sintering. In general, Stage I is attributed to when the power supply is in "voltage control" mode, while Stage II is during the non-linear rise of current and Stage III is during the holding time in "current control" mode.

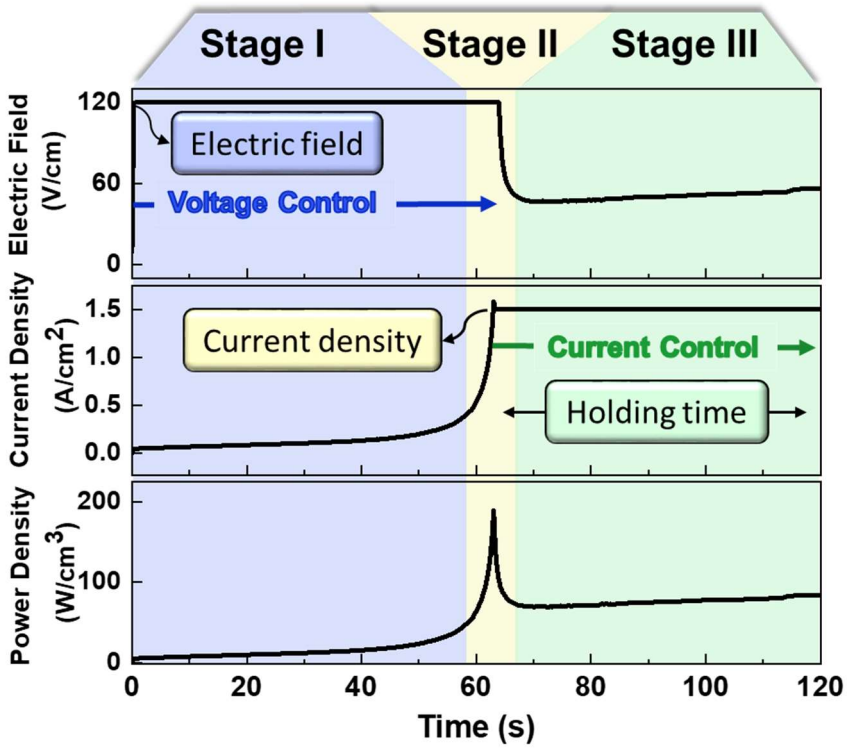

Figure 2.4 Three stages of flash sintering. [56]

2.2.1 Stage I

Stage I begins when the electric field is applied across the sample and ends when the current begins to increase in a non-linear trend. The Stage I behavior is dependent on the initial sample resistivity, which is determined by several experimental factors [119]. Most often, the combination of electric field strength and furnace temperature are the dominant factors contributing to the varied length of Stage I, which can vary from several seconds up to several hours. The initial sample resistivity can also be influenced by powder chemical composition, particle size, green body density and furnace atmosphere [120–122]. As this stage pertains to the behavior before the non-linear increase in conductivity, researchers have referred to this stage as an "incubation" period [123,124].

2.2.2 Stage II

Stage II is usually a brief stage lasting several seconds when the current rises in a non-linear trend. During this time, the power supply needs to be switched from a voltage control to current control mode in order to prevent the current increasing indefinitely. This action can be performed by setting a feedback loop for the power supply when the current has reached the limit set. The abrupt current increase and switch to current control forms a sharp spike in the power density curve. During this stage, most of the densification process occurs, as the sample experiences large thermal runaway by Joule heating and usually emits a very bright light emission. The transient behavior of this stage makes it difficult to fully understand what happens during this very abrupt moment.

2.2.3 Stage III

Stage III occurs during current control mode. This stage be held for an infinite time, as long as the sample remains conductive, which is why it is known as the "steady-state" stage. During this stage, the current is completely flowing through the sample and internally heating by Joule heating. Since the power supply is no longer under voltage control, the electric field will change according to the conductivity of the sample. It is often observed that the electric field during this stage will begin to decrease over time, since the sample conductivity increases. This stage is usually kept brief to avoid significant grain growth, from several seconds to several minutes, which is significantly shorter than conventional sintering. Many *in situ* characterization studies have been preferably performed during Stage III since it can be held more consistently for a longer time, compared to Stage I and II [45,55,97].

2.3 Proposed mechanisms

The mechanism of flash sintering was a critical discussion topic since its first report in 2010. The main motivation for the mechanistic studies is to understand the rapid mass transport process during flash sintering. Ceramic sintering is a lengthy process which rely on rate-limiting diffusional mass transport. Yet, flash sintering is able to overcome many of those obstacles and ceramics can undergo remarkably fast densification at lower temperatures. The flash phenomenon has brought up many fundamental questions of how its mass transport process would differ from conventional sintering. The investigation of the flash sintering mechanism mainly aims to explain three main events:

1. Rapid densification within seconds
2. Abrupt non-linear rise of conductivity
3. Intense light emission

Overall, the rapid densification during flash sintering can be sufficiently explained by the Joule heating phenomenon, which leads to elevated sample temperatures and ultra-high heating rates. While some believed that Joule heating was the only responsible mechanism for the rapid densification, others believed there are additional mechanisms activated during this unique phenomenon which has led to a strong debate among the community. The main mechanism, Joule heating, will be discussed further, along with other proposed mechanisms including nucleation of Frenkel-pairs and local surface and grain boundary overheating by Joule heating.

2.3.1 Joule heating

Joule heating is a notable phenomenon when current flows through a conductor and produces heat and has been the most agreed mechanism for flash sintering. Since most ceramics have a negative temperature coefficient (NTC) of resistivity, they become increasingly conductive with increasing temperatures [18]. As stated by Joule's law, the power of heating (P) is equal to the product of voltage (V) and current (I):

$$P = V \times I = \frac{V^2}{R}$$

By substituting Ohm's law (I = V/R), P is equivalent to V^2/R, where R is the resistance. Thus, the rapid drop in resistance during sample heating would explain the increase in power dissipation (Figure 2.5). This leads to a thermal runaway event, where the electrical power is converted into heat dissipation of the sample [18]. Such an event will cause a rapid increase sample temperature up to several hundreds of celcius above the furnace temperature, which explains the accelerated rates of mass transport.

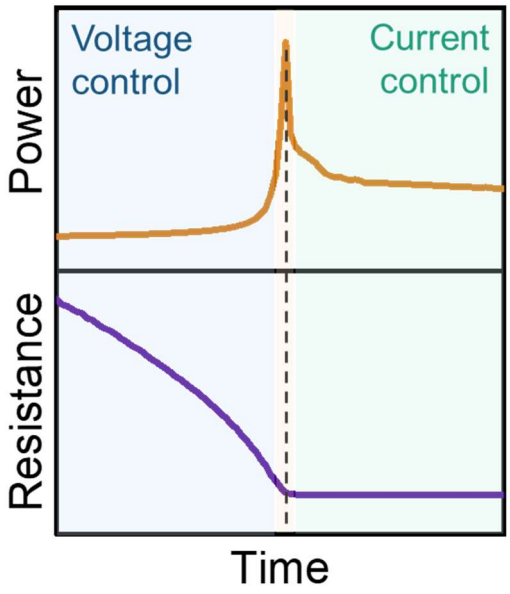

Figure 2.5 Plots of power and resistance during flash sintering.

While an increase in sample temperature contributes to higher densification rates, that should also include the grain growth process. Often, the sample grain sizes from flash sintering are smaller than conventional sintering when sintered to similar final densities [120,125]. Thus, the elevated sample temperature is most unlikely not the only reason that Joule heating expedites the densification process. Several studies have suggested that the rapid densification during flash sintering are mainly contributed by the ultra-high heating rate [98,126]. As current is increasing in a non-linear rate, the sample temperature would also increase rapidly. The first estimation of heating rate was Grasso modeled using finite element analysis (FEA) and estimated the heating rates to be approximately 10^4 °C/min during flash sintering [127]. This heating rate is orders of magnitude higher than typical conventional sintering and most sintering techniques, as shown in the heating rate comparison in Figure 2.6 [128]. The impact of ultra-high heating rate during flash sintering was compared to various techniques with similar heating rates, such as fast firing and

self-propagating high temperature synthesis. The resulting density and grain size from the various ultra-fast heating techniques are comparable to flash sintering for 3YSZ [98,126] and ZnO [126].

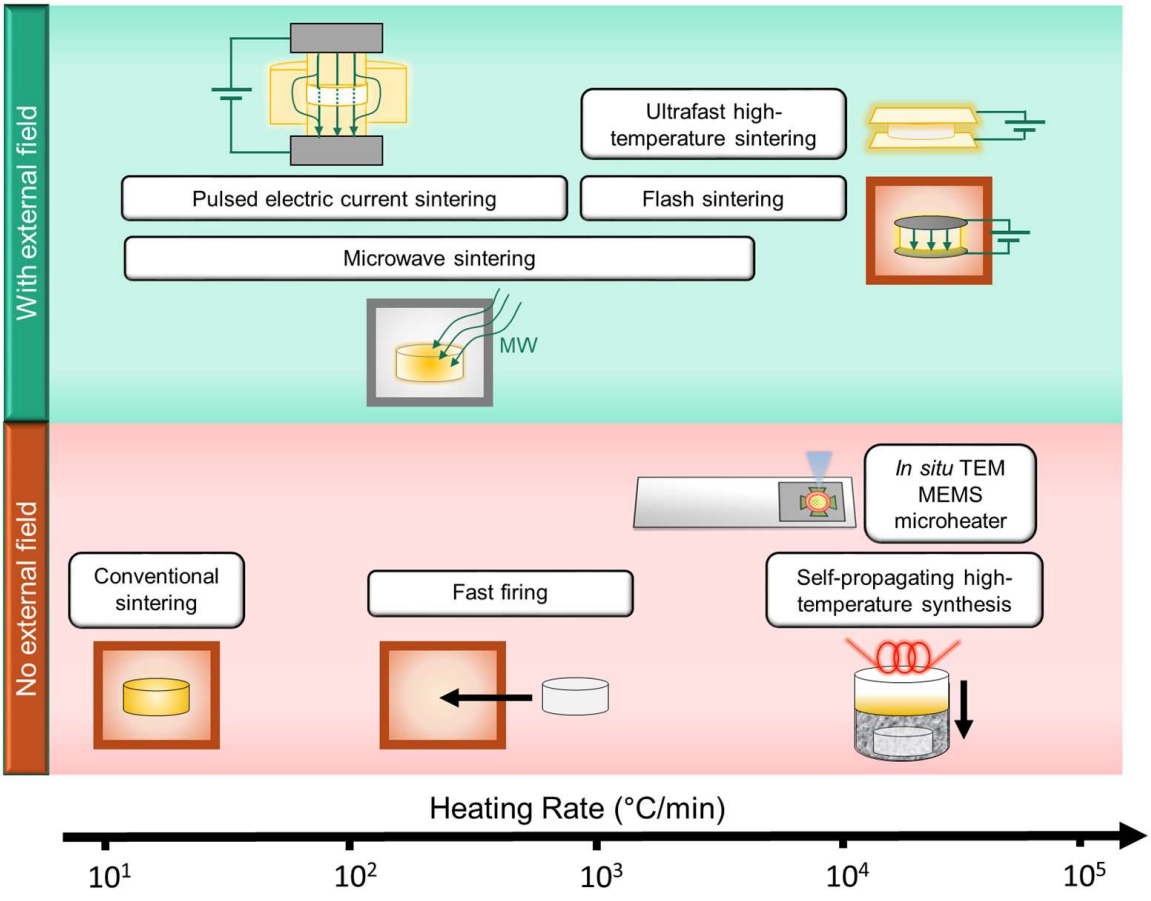

Figure 2.6 Estimated heating rates for various sintering techniques. [128]

Due to the ultra-fast heating rates involved, a recent flash sintering study discusses the possibility of plastic flow to occur which contributes to the rapid densification [129]. In conventional sintering, plastic flow is a possible densification mechanism but only if dislocations are nucleated and mobile. Since flash sintering experiences ultra-high heating rates to high temperatures, it is possible for the plastic flow mechanism to be activated. There have been

multiple previous studies which show some evidence of this event, such as superplasticity during flash sintering [130], viscosity effects [131] and presence of dislocations after flash sintering [56,69,121]. These studies point towards the existence of the plastic flow mechanism during flash sintering and it is still currently an active research topic, especially its correlation to the impact of an electric field and current (electroplasticity).

Besides the rapid densification, it is also necessary to correlate Joule heating to the non-linear increase of conductivity and bright light emission. While the sample conductivity is steadily increasing from the furnace heating process, the formation of particle necks and sample densification are possible reasons for contributing to the increase in conductivity. While this is a feasible explanation, the increase in conductivity can also be contributed by the increase in charge carriers at higher temperatures and this will be dependent on the in defect reactions of the ceramic system. Both of these are likely the main contributors to the non-linear increase of conductivity simply based on a thermal explanation, but it should be noted that this has additional complexity due to the impact by electric field- and current-induced effects which will be further discussed later in 2.4.1. On the other hand, the bright light emitted by the sample can be simply explained by the thermal radiation from the sample [132]. As materials are heated past a certain temperature, the electrons are excited and release photons, creating the bright light.

While this is a universal mechanism of flash sintering, there are many unique characteristics observed in flash sintered ceramics, such as microstructure gradients, defects, metastable phases and textures which could not be simply explained by the Joule heating effects. Thus, the discussion on flash sintering is now categorized into thermal and non-thermal effects to isolate the effects of Joule heating and those related to the defects [133]. The non-thermal effects are usually material dependent and non-equilibrium features, which can be extremely

advantageous in producing ceramics with highly enhanced properties. These effects will be further discussed in 2.4.

2.3.2 Nucleation of Frenkel-pairs

Formation of Frenkel defects was one of the earliest proposed mechanisms to explain the simultaneous rapid mass transport, increase in conductivity and bright light emission [134]. A Frenkel defect is the formation of a vacancy-interstitial pair, which can undergo in both cation and anions for ionic ceramics. This is schematically shown in Figure 2.7 and can be generally written in Kröger-Vink notation as the following:

$$M_M^x + V_i^x \rightarrow M_i^{\cdot\cdot} + V_M''$$

When these pairs form, the densification process is rapidly enhanced when the vacancies move towards the grain boundary, while the interstitials migrate towards the pores. With the formation of Frenkel pairs, this can also result in the formation of free electron and holes, contributing to the increase in conductivity. Additionally, the intense light emission was suggested to be a result of electroluminescence from the recombination from electrons and holes [135,136].

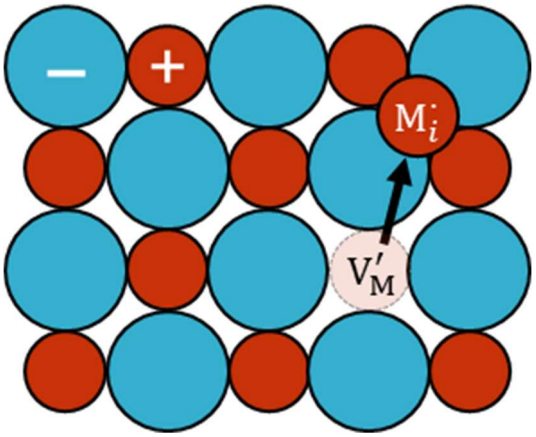

Figure 2.7 Frenkel defects forming a vacancy-interstitial pair.

However, this mechanism was highly criticized for several reasons. Firstly, the formation of single charged ions require a very large applied field, for example, the formation of Frenkel pairs for HfO_2 was estimated to be around 10 GV/m (10^8 V/cm) [137]. This strength of field required to form the Frenkel defects are significantly higher than the values used in the typical flash experiment, which is usually around 50 to 1000 V/cm. Secondly, Frenkel defects are limited to ionic compounds with low coordination numbers and significant size difference between cations and anions. This is because Frenkel-pair formation conserves mass and charge, thus the created interstitials require an unusual position in the lattice which may not be possible for all ceramic systems. Lastly, a photoemission study has showed that the optical emission spectra has a strong correlation with the sample temperatures and did not show any peaks correlated to the formation of Frenkel defects [132]. Overall, the lack of direct evidence makes this mechanism still in question. Although Frenkel defects may not necessarily be the dominant reaction, the formation and redistribution of various point defects do play a significant role during flash sintering, and will be further discussed in 2.4.

2.3.3 Local surface and grain boundary Joule heating

Another flash sintering mechanism which has been often discussed is the local surface and grain boundary Joule heating. This mechanism differs from the bulk Joule heating process since it refers to a localized effect caused by high electric field and current density near the particle contacts and grain boundaries. Consequently, local overheating near interparticle contacts are believed to occur and thus resulting in rapid densification through liquid phase [138–142]. Although this mechanism can potentially explain the rapid densification and increase in electrical conductivity, these studies are mainly supported by theoretical models and lacking of any direct microstructural evidence, such as liquid films or phases. Studies which have shown the liquid

phase formation after flash sintering are only for systems which are known to form liquid phases due to their low melting points [23], and thus this is likely not a general effect of flash sintering. It is possible that these liquid films are transient [139], or in a grain boundary transition state often described as “complexions” [23]. A recent study showed that these grain boundary complexions are likely to be formed by the presence of electric fields and currents, and can significantly impact the grain boundary diffusivities and mobility [143]. However, these effects are extremely challenging to investigate as they require sophisticated characterization tools and their correlation to flash sintering mechanism is still unclear and under investigation.

2.4 Defect characteristics of flash sintered ceramics

Many studies on flash sintered oxides have reported unusual characteristics such as grain size distributions [20,54,69,125,144], sample blackening [47,54,79,100,144,145], grain boundary segregation [69,121] and the formation of extended defects [22,56,57,121,146]. These observations are correlated to the redistribution of point defects during the flash sintering process due to the impact of an electric field and current. It is important to study the nature of these defective characteristics as with proper control and optimization can lead to many enhanced properties in ceramic materials, such as mechanical, electrical and optical properties.

2.4.1 Impact of electric field/current on point defects

Point defects in crystalline ceramics are any imperfections in the crystal lattice as single lattice points. This include missing atoms or vacancies, interstitial atoms or substitutional atoms. As sintering occurs by diffusion of mass, point defects control the rates of diffusion and will determine the rate of sintering and grain growth. The role of point defects is particularly important in the presence of electric field and current because most of the ionic and electronic defects are

charged species. Defect reactions can occur at elevated temperatures where defects are mobile, and they will rely on the flash sintering conditions and defect chemistry of the material.

In many flash sintered oxides, sample blackening has been observed, including YSZ [100,145], TiO_2 [54], Al_2O_3 [79], $MgAl_2O_4$ [144] and Gd-doped CeO_2 [47]. Examples of sample blackening are shown in Figure 2.8, where black or dark colored regions can be observed macroscopically. This is induced by a reduction defect reaction which leads to change in oxygen stoichiometry. The propagation of these dark regions appear to be dependent on the electrical conditions, and the propagation direction relative to the electric field direction varies for ceramic systems. In Figure 2.8, the blackened regions initiate from the negative side for 8YSZ while the blackened regions appear to start at the positive side for Al_2O_3 [79,145]. Such differences are associated with the material preferred conductivity and also its defects mobility.

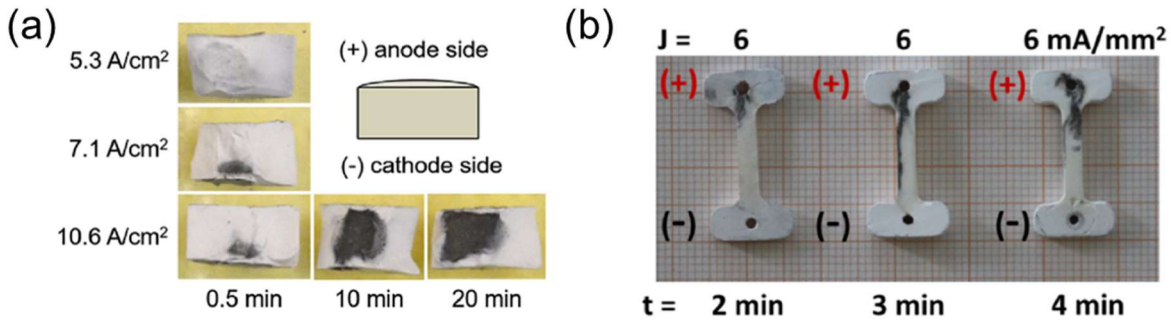

Figure 2.8 Sample blackening observed in flash sintered (a) 8YSZ [145] and (b) Al_2O_3 [79].

Most flash sintering studies which have reported sample blackening focus on investigating 8YSZ [100,147] because it is a well-known phenomenon to occur in ionic conductors with blocking electrodes [148,149]. Figure 2.9(a) shows the schematic of the internal defect reactions when an electric field is applied across the 8YSZ sample [150]. The source of electrons is at the cathode and it will travel to the anode end. As electrons are extracted out of the system, positively charged oxygen vacancies will form and migrate towards the cathode region. Since Pt electrodes are blocking for ions, oxygen vacancies will begin to accumulate near the negative electrode and a partially reduced ($ZrO_{2-\delta}$) front initiates and propagates towards the middle of the sample. This phenomenon during flash sintering not only results in a change in sample color, but also impacts the material conductivity and grain boundary mobility. As the partially reduced region forms, the material conductivity is increased with electronic contribution [151]. This would reduce the electrical resistivity of the material near the cathode side and result in less Joule heating effect, which has been captured by thermal imaging [100]. Figure 2.9(b) shows the grain size distribution of a fully sintered polycrystalline 8YSZ sample after the application of extreme current for a prolonged time [99]. Significant grain growth can be observed near the cathode region, which appears contradictory to the temperature gradient. This has been explained by the enhanced grain boundary mobility from the impact of a partial reduction on the migration energy barrier [99,152,153].

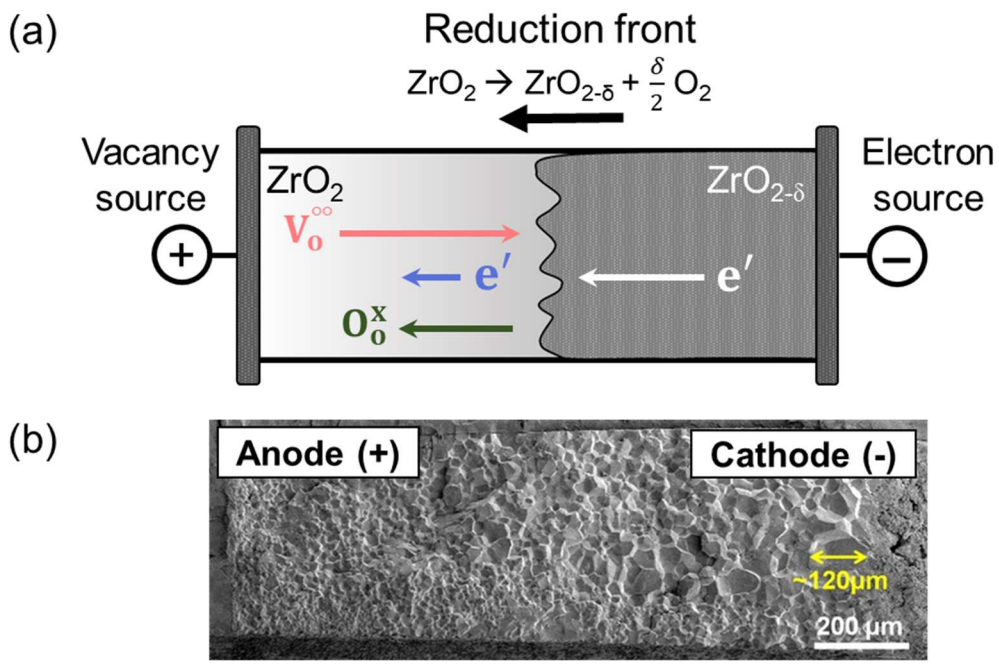

Figure 2.9 (a) Schematic showing the redistribution of defects in flash sintered 8YSZ which causes a partial reduction. (b) Microstructure gradient which exist in fully sintered polycrystalline 8YSZ after extreme current and holding time. [99,150]

A recent study on flash sintered Gd-doped CeO_2 also showed very similar electrochemical reduction behavior to the 8YSZ system [47]. While the phenomenon appears consistent in ionic conductors, this cannot be a generalized for other ceramic materials due to their contrasting conductivity behavior. For example, TiO_2 and Al_2O_3 has shown the opposite direction of sample blackening and grain size gradient after flash sintering [20,54,56]. The reduction regions would strongly depend on the formation of oxygen vacancies in the sample and also the mobility of positively charged oxygen vacancies towards the negative electrode [79]. The contrasting observation in semiconductor and insulating materials are interesting observations and still currently under investigation.

Systems with well-known space charge and segregation behavior are ideal for investigating the redistribution of point defects and have been demonstrated in several flash sintering studies [69,121,154]. Figure 2.10(a) and (b) shows contrasting grain sizes for flash sintered $SrTiO_3$ on the positive and negative electrodes, respectively [69]. The difference in grain sizes can be correlated if there are any pronounced space charge events at the grain boundary. Since it is challenging to identify any grain boundary segregations from an undoped system, Fe was added as an acceptor dopant to more clearly reveal any charge segregation. After flash sintering $SrTiO_3$ with 5 at.% Fe dopant, a pronounce Fe segregation was observed near the positive electrode (Figure 2.10(c) and (e)). Since Fe is an acceptor dopant, Sr vacancies or Fe would accumulate at the grain boundary in an oxidized state [155]. The accumulations of point defects near the positive electrode would consequently cause grain boundary diffusional drag and result in smaller grain sizes. This is in contrast to the negative electrode which had a less obvious Fe segregation (Figure 2.10(d) and (f)). This characteristic space charge would occur in a reduced $SrTiO_3$ state and have less impact on the grain boundary mobility. Overall, these space charge behaviors show a gradient in oxygen vacancy concentrations and their impact on the microstructure after flash sintering.

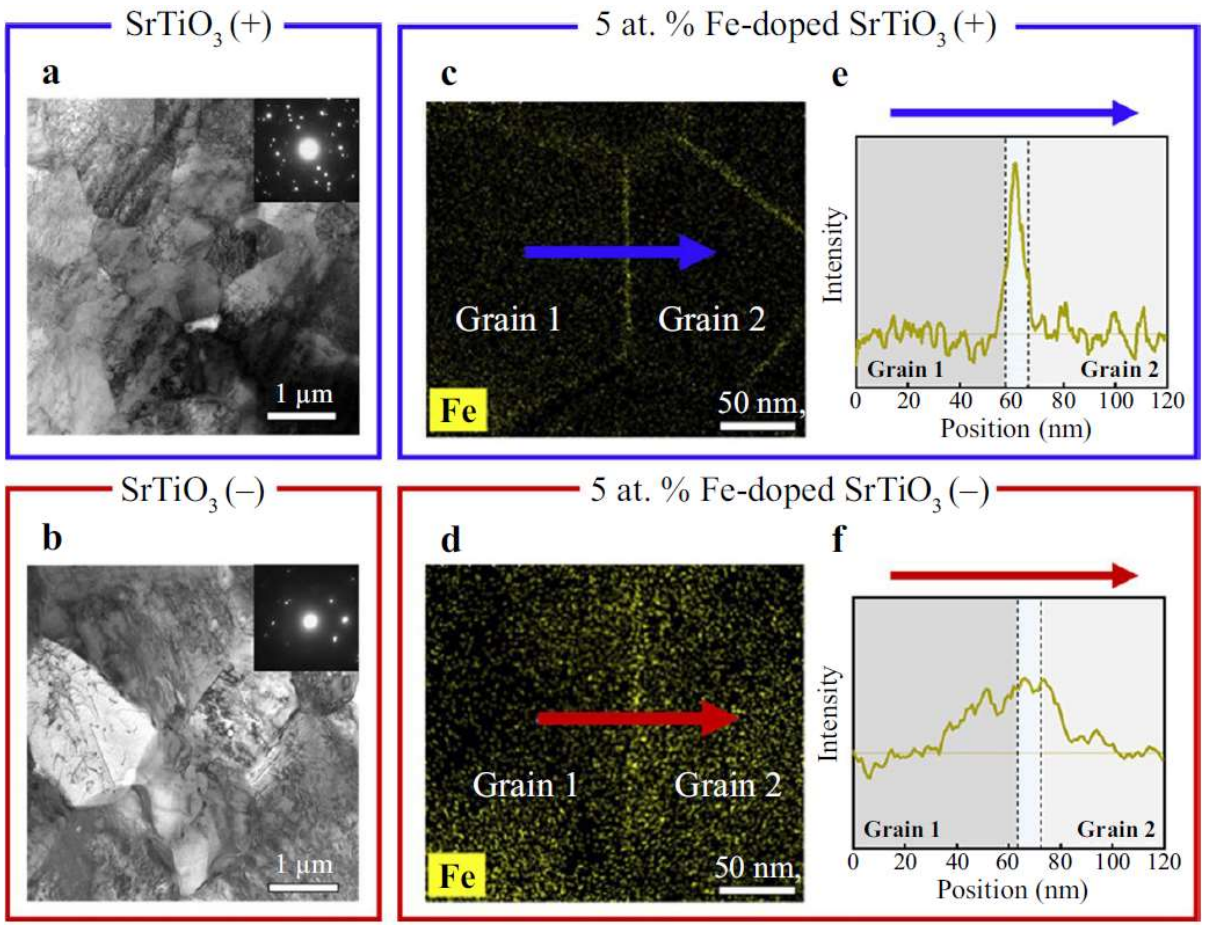

Figure 2.10 TEM images of the (a) positive and (b) negative electrodes for flash sintered $SrTiO_3$. Elemental map of Fe showing the segregation behavior near the grain boundaries after flash sintering of Fe-doped $SrTiO_3$ and the corresponding line profiles of Fe near the (c,e) positive and (d,f) negative electrodes. [150]

2.4.2 Observation of extended defects

Another characteristic of flash sintered ceramics are extended defects, such as dislocations and stacking faults. In Figure 2.11, high density of dislocations have been observed in transmission electron micrographs of flash sintered 3YSZ, TiO_2, and $SrTiO_3$ [56,69,121]. Dislocations are line defects in crystalline materials and responsible for plasticity in materials. While they are easily found in metals, they are usually less important for ceramic materials due to their rigid bonding and difficulty gliding. Since ceramics undergo ultra-fast heating rates to elevated sample

temperatures during flash sintering, this could lead to higher sintering stresses and result in nucleation of dislocations for plastic flow [129]. While this is also possible event for conventional sintered ceramics, it is more likely negligible and ceramics are often found dislocation-free.

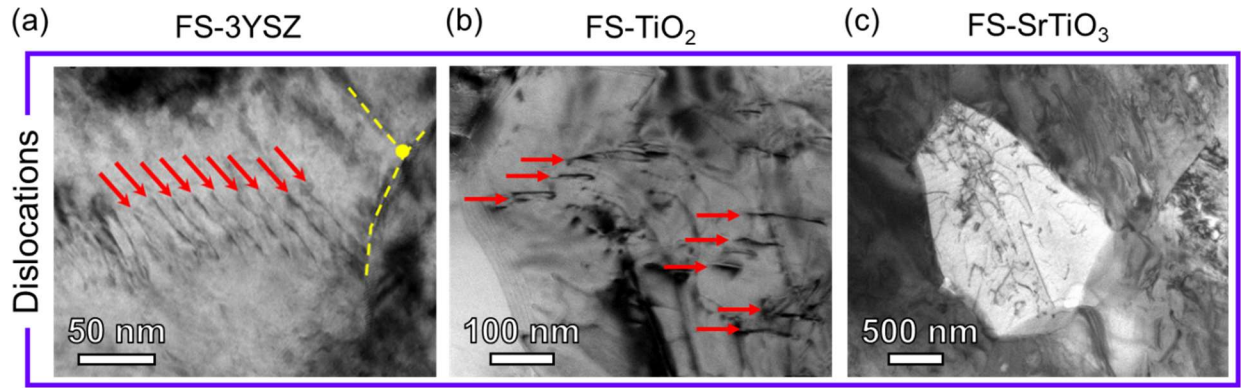

Figure 2.11 TEM image showing dislocations present in flash sintered (FS) (a) 3YSZ, (b) TiO_2 and (c) $SrTiO_3$. [150]

Planar faults have also been observed in several flash sintered ceramics [22,56,60]. These planar defects are often found as stacking faults, as a result of a pair of partial dislocations which form an incorrect stacking sequence of crystal plane. One of the flash sintered system which has shown to form high density of stacking faults is the TiO_2 system, as shown in Figure 2.12 for various electrical conditions. TiO_2 is a material which can largely deviate from oxygen stoichiometry by forming shear phases, known as the Magnéli phases. These reduced phases are formed by the ordering of oxygen vacancies or titanium interstitials to form shear planes, followed by ordering of the planes into the shear phases. For flash sintered TiO_2, only planar defects were observed and Magnéli phase was not detected [56], which would likely point towards a slightly reduced state of TiO_x where $1.999 < x < 1.9999$ [156]. It is also possible to tune the defects density by adjusting various flash sintering electrical parameters, such as electric field, current density

limit and holding time [56]. Higher defects density was achieved by utilizing a stronger electric field, lower current density and shorter holding time.

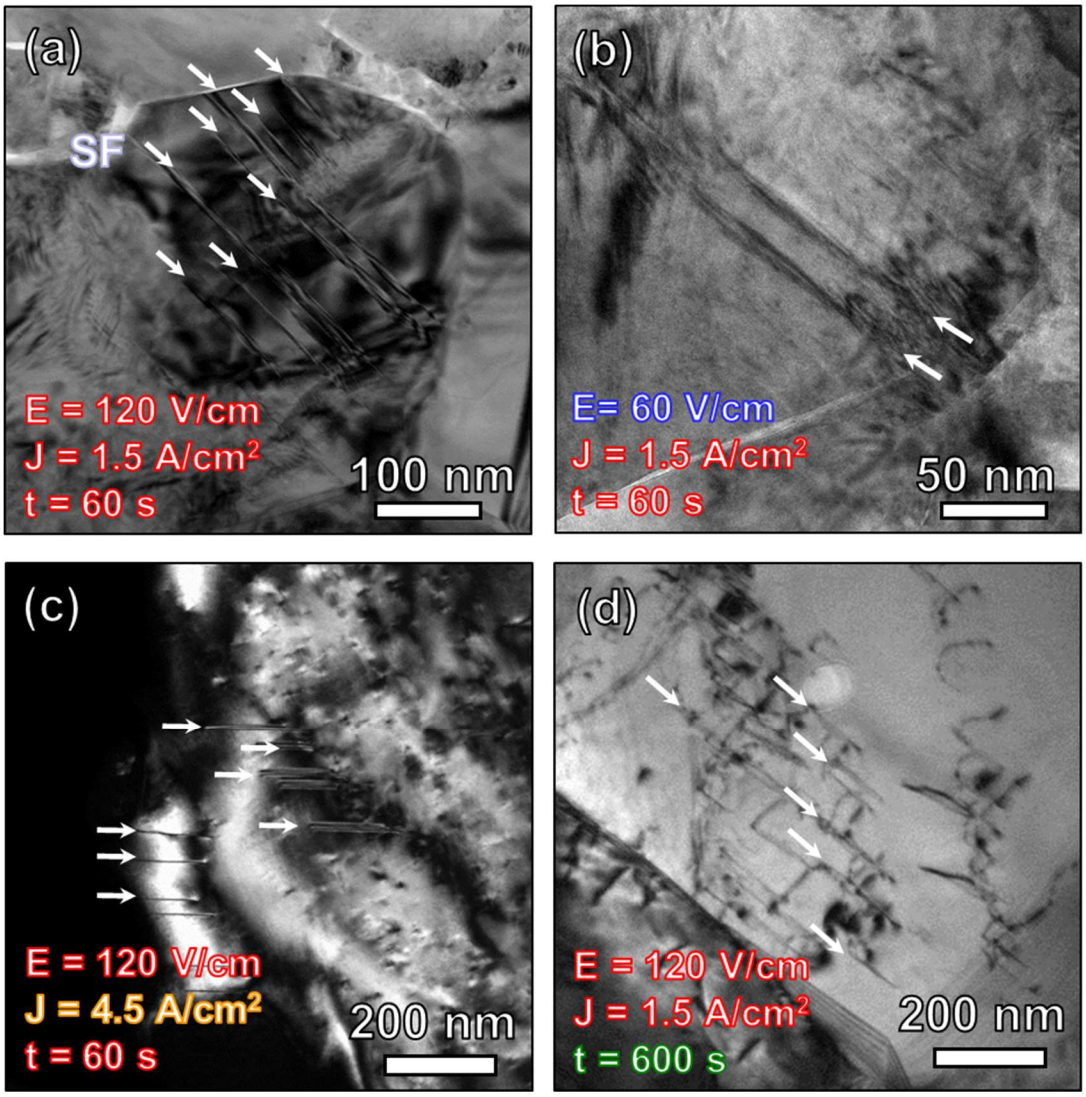

Figure 2.12 TEM showing high density stacking faults (SF) near the positive electrode of flash sintered TiO_2 with various flash sintering electrical conditions. [56]

These defects characteristics in flash sintered ceramics are very interesting and could open many new opportunities for defect engineering of ceramic materials. In addition, the electrical parameters of flash sintering offer a way to the tailor the defects density of the material, which could be highly important in controlling the properties of the material. While such systematic studies can be performed to control the defects density, it is still difficult to isolate the events during flash sintering to understand how they form during the flash sintering process. Thus, the next section will discuss the various *in situ* characterization methods that can help to probe the redistribution of defects in real-time during the flash sintering process.

2.5 *In situ* characterization

Most flash sintering studies typically utilize *ex situ* characterization techniques on post-sintered specimens. Although the information gained is useful in explaining several characteristics of flash sintering, these characterization techniques could not elucidate the various timestamps of events during the three stages of flash sintering. To investigate this dynamic and complex process, studies have employed several *in situ* characterization techniques during flash sintering to investigate the phenomenon in real time. Table 2.1 shows a summary of various *in situ* techniques which have been used to investigate flash sintering, along with their purpose and ceramic systems studied.

Table 2.1 Summary of *in situ* characterization techniques used for flash sintering.

***In situ* technique**	**Purpose(s)**	**Material(s) studied**
Diffraction	• Measure lattice expansion • Estimate sample temperature • Identify texture and chemical/phase change	3YSZ [157–159], 8YSZ [160,161], TiO_2 [51,53,55], ZnO [24,162], CeO_2 [45], UO_2 [90], $BiFeO_3$ [163,164], Al_2TiO_5 [95], TiB_2-TiO_2-$TiBO_3$ [165], $MgAl_2O_4$-8YSZ [97,166,167], $Li_{0.5}La_{0.5}TiO_3$ [168], $Li_{6.25}Al_{0.25}La_3Zr_2O_{12}$ [169]
Transmission electron microscopy	• Observe morphology change in particles due to electric field or ultra-fast heating	3YSZ [128,170], 8YSZ [128], ZnO [128,171]
Optical emission	• Analyze the optical spectra due to photoemission	3YSZ [135,136], 8YSZ [172], SnO_2 [172] , Al_2O_3 [132], silicate glasses [81,132]
Thermal imaging	• Map surface temperature distribution	8YSZ [100,173], B_6O [174], ZnO [21]
Impedance	• Estimate flash temperature	8YSZ [151,175]

A large majority of *in situ* studies employed diffraction techniques, by performing flash sintering experiments at synchrotron facilities, such as Advanced Photon Source (APS) at Argonne National Laboratory and National Synchrotron Light Source (NSLS) at Brookhaven National Laboratory. *In situ* diffraction is extremely useful for investigating the flash sintering process because it reveals critical information on the lattice structure. Most experiments are performed during Stage III of flash sintering since it is steady-state and will allow for measurements to be done in a timely manner. There are two main types of diffraction techniques used, as shown in Figure 2.13. The first one is the X-ray diffraction (XRD), which is comparable to typical XRD scan. Most studies have employed it to study lattice parameter changes and peak broadening due

to thermal expansion via Joule heating [158,159], which will allow sample temperature estimations to be performed. This *in situ* technique has also been employed to observe phase changes, such as for phase transformations during reactive flash sintering [95,97,166,168,169,176], or observing the formation of a metastable phase [157] or texture [51]. An alternative to XRD is energy dispersive X-ray diffraction (EDXRD), which utilizes a polychromatic X-ray beam with a fixed detector. EDXRD offer several advantages over regular XRD, such as detection of energy at single point and can scan across height of specimen at fixed 2-theta. This offers the possibility to investigate any inhomogeneous lattice expansion across the height of the samples [45,55], which is an important characteristic of flash sintered samples.

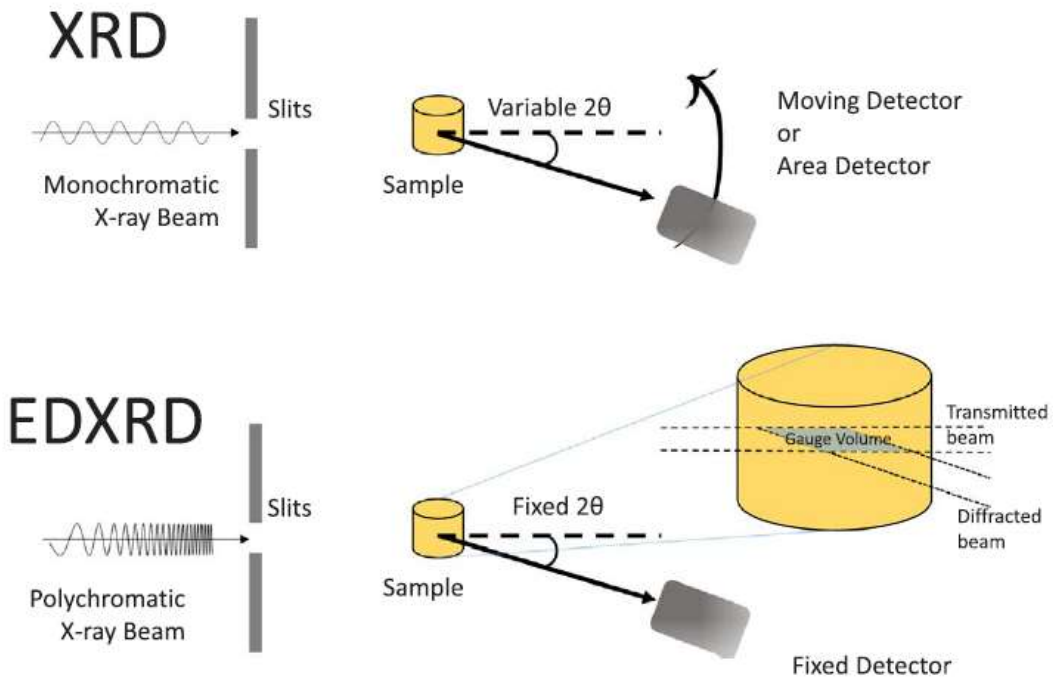

Figure 2.13 Schematic showing the difference between *in situ* X-ray diffraction (XRD) and energy dispersive XRD (EDXRD). [38]

To demonstrate the use of *in situ* diffraction during flash sintering, Figure 2.14(a) and (b) shows the flash sintering electrical profile for CeO_2 and the corresponding interplanar spacing profile across the sample before, during and after flash obtained through the EDXRD technique. The spacing appears uniform throughout the sample before flash occurred, but showed a significant expansion near the cathode during flash which continuously increased during the steady-state current hold. The schematic in Figure 2.14(c) explains the abnormal lattice expansion by the accumulation of oxygen vacancies and reduction of Ce^{4+} to Ce^{3+}. As CeO_2 is an ionic conductor, the characteristics are similar to 8YSZ as discussed in 2.4.1, where the oxygen vacancies accumulate near the cathode due to the blocking electrode. After the power supply is turned off, the interplanar spacing near the anode returned to its original value but still showed a small lattice expansion near the cathode due to the reduction. This study shows the importance for *in situ* diffraction techniques, where real-time observation of lattice changes during flash sintering is possible.

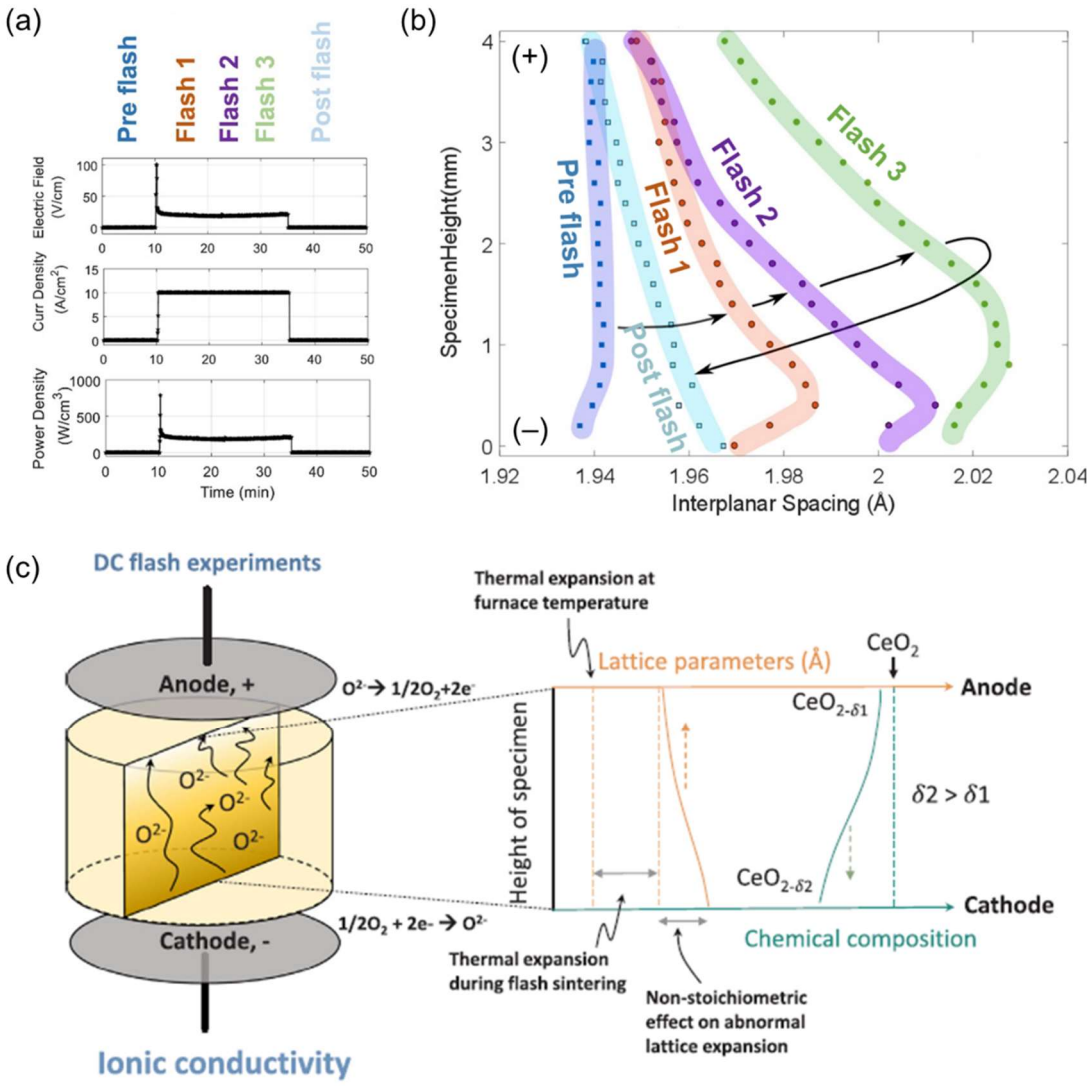

Figure 2.14 (a) Flash sintering plot for CeO_2 with labels indicating the timing of the EDXRD scans performed and the (b) corresponding lattice parameter profile. (c) Schematic showing the reduction near the cathode which resulted in the lattice expansion. [45]

Another important *in situ* technique which has been used to investigate flash sintering is transmission electron microscopy (TEM). This technique is highly advantageous as it allows for direct observations on the particle morphology due to external heat and field. In a recent study, various ceramic nanoparticles were heated using an ultra-high heating rate similar to flash sintering during TEM observation. Figure 2.15 shows the snapshots comparing heating of 3YSZ nanoparticles before and after ultra-high heating rate (1200°C/s) and slow heating rate (5°C/s). This study directly shows the rapid densification of the nanoparticles after ultra-high heating rate, which justifies it as one of the mechanisms of flash sintering. Other studies investigated the impact of an electric field during the sample heating during TEM and saw enhanced shrinkage of an agglomerate of nanoparticles [170].

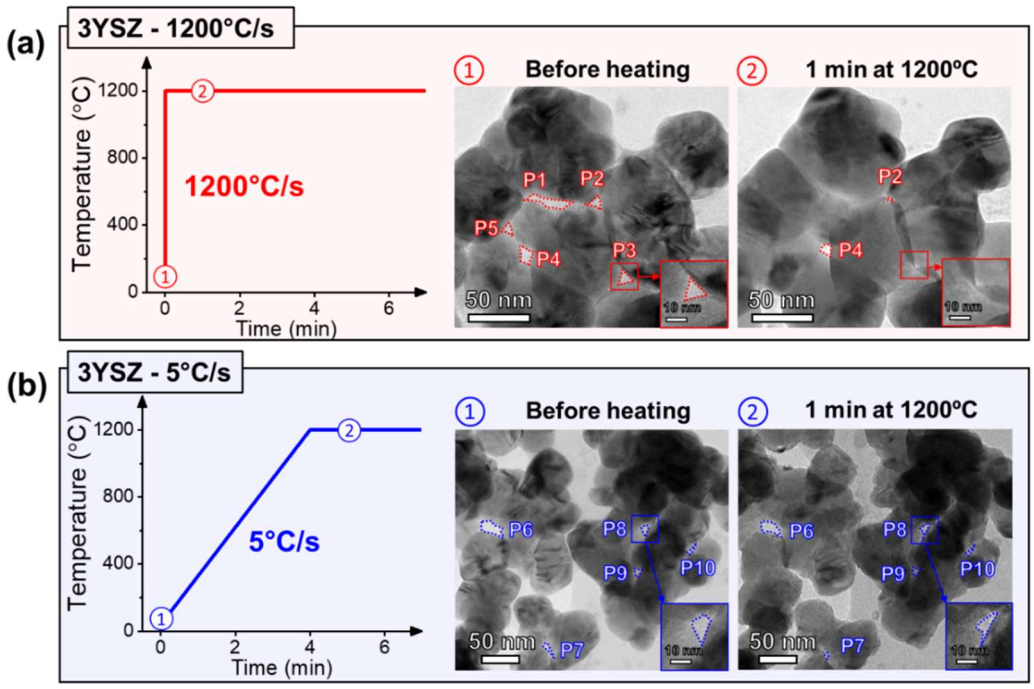

Figure 2.15 Heating profile and the corresponding snapshots of the sintering of 3YSZ nanoparticles during *in situ* TEM before and after (a) ultra-high heating rate and (b) slow heating rate. [128]

There are several other *in situ* techniques which have been used to investigate flash sintering, including optical emission spectroscopy, thermal imaging and impedance spectroscopy. The optical emission spectroscopy has helped to reveal the origin of intense light emission during flash sintering [86,132], while thermal imaging and impedance spectroscopy are mainly used to investigate the sample temperature. Overall, *in situ* techniques are highly impactful for elucidating many flash sintering characteristics not observed through *ex situ* characterization techniques.

2.6 Motivation and objectives

Flash sintering offers many advantages compared to conventional sintering techniques, but there are still challenges in moving this technique towards practical applications. One of them being the inhomogeneity across the sample, due to temperature gradients from experimental conditions [177] and non-thermal effects arising from defect redistribution [178]. The interplay of both events usually result in microstructure gradients across the sample, and thus, it is necessary for systematic and in-depth investigation on controlling the microstructure and defect characteristics of flash sintered ceramics. Another challenge for flash sintering is for the employment of flash sintering in new applications. Currently, this technique is mostly limited to sintering of basic geometries towards achieving full density. In order for flash sintering to expand its list of applications, it is necessary to explore the employment of this technique for other functions. For example, utilizing its unique ability of producing highly defective flash sintered ceramics or producing partially reduced materials or gradient structures. Additionally, many of the past flash sintering studies have been heavily focused on the YSZ system [102], which is why it is especially important to study other ceramic materials with high technological importance.

Based on the challenges, ZnO is selected as the ceramic system for investigation in this dissertation. ZnO is an n-type semiconductor material with high versatility in a wide range of applications. It has been used particularly for many optoelectronics and luminescence applications due to its wide band gap (3.4 eV) and large exciton binding energy (60 meV). The wurtzite crystal structure lacks of center of symmetry, which makes ZnO a highly important material used for piezoelectric and pyroelectric properties. One of the most unique capability of ZnO is its to grow into a diverse arrays nanostructure morphologies, such as nanowires, nanobelts and tetrapods [179]. Additionally, the impact of defects in ZnO has been intensively studied due to its ability to tune many of its optical and electrical properties. The first report of flash sintering of ZnO using an alternating current was first reported by Schmerbauch *et al.* in 2014. This study also reported photoluminescence measurements which revealed enhanced defects mobility during flash sintering of ZnO [19]. Following that study, numerous studies by Dr. Luo's group published flash sintering of ZnO using direct current and reported the effects of various electrical conditions on the microstructure gradient between the electrode ends [20]. Additionally, a study showed that current localization in the flash sintered ZnO sample led to the growth of large microrods near cracks [20].

To further explore the impact of electrical conditions on the microstructure gradient of flash sintered ZnO, Chapter CHAPTER 4 will compare the grain growth behavior and defects structures of flash sintered ZnO with and without controlled current ramp. During Stage II of flash sintering, ceramics typically undergo the rapid densification during the non-linear increase of current. The effect of an abrupt increase in current was investigated by detailed microstructure comparison between a flash sintered ZnO samples with a controlled current ramp (linear increase of current) and without (non-linear increase of current). This chapter presents a way to better

control the flash sintering process, especially during the abrupt increase in current which can lead to inhomogeneous microstructures. Since flash sintering using a direct current (DC) and alternating current (AC) have been studied separately previously, Chapter CHAPTER 5 will compare the microstructure and defects obtained from DC and AC flash sintered ZnO with similar electrical and thermal parameters. This chapter helps to contrast the characteristics from DC and AC flash sintering for future use in various applications based on their preferred microstructure and defects.

In Chapter CHAPTER 6, the unique formation of highly defective ZnO one-dimensional (1D) nanostructures through flash sintering are demonstrated. One-dimensional ZnO nanostructures have high importance in many optical and electronic applications, and most studies which grow the nanostructures use an equilibrium processes which results in low defects controlled by thermodynamic equilibrium. The nanostructures grown by flash sintering contained high density of defects and in Chapter CHAPTER 7, further investigation of the growth mechanism, and tunability of these nanostructures and defects were explored by tuning the current density limit. This unique application of flash sintering allows it to be used for growing nanostructures with the possibility of defect engineering for a wide range of applications.

CHAPTER 3. EXPERIMENTAL

3.1 Flash sintering of ZnO

Based upon the description of flash sintering experimental setup in 2.1, flash sintering will require a green body, electrical contacts and wires, furnace and power source. ZnO nanopowder used to form compacts are obtained from Sigma Aldrich (particle size < 100 nm #544906) and US Research Nanomaterials (particle size average 18 nm #US3599). The powder is packed into a 6 mm diameter stainless steel die and pressed using uniaxial force to produce a cylindrical green body with a density of ~55-60%. The green compact is placed in a furnace with the flat ends connected to platinum electrodes and wires to an external power source. Power sources which were used include B&K Precision 9115 (DC, 80V, 60A), Sorensen DLM 300-2 (DC, 300V, 2A) and Pacific Power 118-ACX (AC,150V, 10A, 45-1200 Hz). A Labview program was written to control the electrical parameters and record the plots for the flash sintering process.

3.2 Characterization

3.2.1 X-ray diffraction

X-ray diffraction (XRD) is a technique used to obtain crystal structure information in crystalline materials by analyzing scattered X-rays. X-rays are generated by accelerating electrons onto a metal target and produced X-rays are directed onto the sample. The scattered X-rays are collected by a rotating detector to collect signal from a range of diffraction angles. The diffraction angle which has higher intensity of scattered signal is dependent on the Bravais point lattice and unit cell dimensions, whereas the variation of the peak intensity will depend on the geometrical relation of atomic positions in a crystal structure [180]. XRD was used to investigate the phase and

lattice parameter information of flash sintered ZnO and was performed on a PANalytical Empyrean using Cu-kα radiation (λ = 0.154 nm) at 40 kV and 40 mA. The lattice parameter is calculated using Bragg's law:

$$\lambda = 2d \sin\theta$$

where λ is the wavelength of the radiation source, d is the interplanar spacing and θ is the diffraction angle. ZnO has a hexagonal unit cell and the relationship between interplanar spacing and lattice parameter can be described as:

$$\frac{1}{d^2} = \frac{4}{3}\frac{h^2 + hk + k^2}{a^2} + \frac{l^2}{c}$$

where h, k and l are the corresponding plane Miller indices, and a and c are the lattice parameters (a = b for hexagonal).

3.2.2 Scanning electron microscopy

Scanning electron microscopy (SEM) is a necessary tool for analyzing ceramic microstructure. This technique captures information by accelerating high energy electrons (typically ~1 to 30 kV) onto the sample, which causes photons and electrons signal to be emitted. Through various detectors in the vacuum chamber which are located strategically, the emissions can be captured. For topographical information of the sample, low energy secondary electrons are captured by an Everhart-Thornley detector (ETD) [181]. Secondary electrons are created from inelastic collisions, and are only impacted by the energy of the incident beam and the surface roughness. This technique is highly advantageous over optical microscopy techniques which uses light scattering since it can obtain images with depth of field. In this dissertation, secondary

electron imaging was captured using Thermofisher FEI Quanta 650 and Quanta 3D FEG to analyze the average grain size, grain size distribution, porosity and surface defects such as cracks and voids.

3.2.3 Transmission electron microscopy

Transmission electron microscopy (TEM) uses a high energy electron beam to obtain images of a specimen, similarly to SEM. A major difference with this technique is that the electron beam transmits through by the sample, which can provide much more information about the sample up to the atomic scale. For the electron beam to transmit through the sample, the samples often require an area where it is thinned to approximately 100 nm or less, which can be technically challenging. For conventional sample preparation technique, the sample is first mechanically grinded and polished to about ~60 um, followed by dimpling to create a thinner area near the center of the sample. The final step of sample thinning is performed by ion milling, which uses an ion beam to further thin the sample near the center to ~100 nm thickness for electron transparency. TEM samples can also be prepared through focused-ion beam (FIB) technique, which is performed in a SEM using a liquid metal ion source. An area of the sample is cut and lifted out, and mounted on a grid for further thinning and polishing.

The employment of TEM is important for this dissertation work since it allows for observations of extended defects which are nanoscale, such as dislocations and stacking faults. As extended defects cause diffraction contrast, they can be observed in the bright-field or dark-field mode with the use of an objective aperture in the beam. ZnO is known to form basal-plane stacking fault (c-axis) and it has low formation energy [182]. Thus, detailed analysis using TEM will be able to observe the existence of those defects in flash sintered ZnO. TEM was performed in this dissertation using a Thermofisher FEI Talos 200X with an accelerating voltage of 200 kV.

3.2.4 Density

Density is an important measurement for ceramic materials, as the goal of the sintering process is to densify the material. Bulk density is defined as mass over volume, which can be measured directly through the mass of the sample and geometric volume. The density of the powder compacts before sintering are measured through this technique to obtain the green density of the samples. After sintering, some porosities become isolated and trapped within the sample, while some of the porosities remain open. Both these porosities will lead to inaccuracy of volumetric density measurement after sintering and thus, the sample density after sintering is usually measured by the Archimedes immersion method. This technique relies on Archimedes' principle, which states the buoyant force of an object in an immersed liquid will equal to the weight of the fluid which it displaces. This results in the formula:

$$\rho_{apparent} = \frac{A}{A-B}(\rho_0 - \rho_L) + \rho_L$$

where A is the weight of sample in air, B is the weight of sample in the auxiliary liquid, ρ_0 is the density of the auxiliary liquid and ρ_L is the air density (0.0012 g/cm^3). For the density value to be more meaningful, a relative density is provided to describe the relationship between the density and porosity content. The relative density is calculated as a percentage of the apparent density over the theoretical density, which is 5.61 g/cm^3 for ZnO.

3.2.5 Raman spectroscopy

Raman spectroscopy is a characterization method which investigates the vibration modes of the material based upon the inelastic scattering of photons. Most often, a laser source is used to excite the molecular vibrations in the sample, resulting in energy shift. This technique is useful in

studying flash sintered ceramics since structural disorders and defects can be detected. For this dissertation, Raman spectroscopy was performed on a Renishaw InVia Raman MicroSpectroscopy with a 532 nm wavelength laser source. To analyze the Raman spectra obtained from flash sintered ZnO, the vibrational modes in ZnO needs to be known. Based on group theory, the Raman active zone-center optical phonons for a wurtzite symmetry (space group C_{6v}^4) is predicted to be $A_1 + 2E_2 + E_1$. The A_1 and E_1 symmetry are polar modes with both transverse-optical (TO) and longitudinal-optical (LO) phonons, while E_2 symmetry is nonpolar and appears at two frequencies. The symmetry of these E_2 peaks are important for the analysis as E_2^{high} is correlated to the oxygen atoms and the E_2^{low} is correlated to zinc atoms [183]. The existence of point defects can impact the symmetry of E_2^{low} and E_2^{high} peaks and detailed analysis through models such as Breit-Wagner-Fano (BWF) to predict the dominant defect in the system [184].

3.2.6 Photoluminescence

Photoluminescence (PL) is a characterization technique commonly used in characterizing semiconductor materials with interesting optoelectronic properties, such as ZnO. This technique is similar to the Raman spectroscopy, where the sample is excited by a high energy source such as a laser. This technique is different as it is based on the light emission produced by the sample, which is caused by the photoexcitation of electrons from the valence to conductance band. Such an event causes energy to be emitted in the form of spectral light. ZnO typically shows an emission peak near the UV region due to the recombination of excitons, and one or multiple peaks in the visible range from defect emissions. PL was performed in this dissertation using a Coherent OBIS laser with a wavelength of 375 nm and collected by a SpectraPro HRS-300 spectrometer at room temperature.

CHAPTER 4. COMPARISON OF THE GRAIN GROWTH BEHAVIOR AND DEFECT STRUCTURES OF FLASH SINTERED ZnO WITH AND WITHOUT CONTROLLED CURRENT RAMP

This chapter contains text and figures published in a journal article titled "Comparison of the grain growth behavior and defect structures of flash sintered ZnO with and without controlled current ramp" by X.L. Phuah, H. Wang, H. Charalambous, Shikhar K. Jha, T. Tsakalakos, X. Zhang & H. Wang, Scripta Materialia, 2019, 162, Pages 251-255. The original article has been modified to include information from the supplemental information of the published article.

The authors would like to acknowledge the support from the U.S. Office of Naval Research (Contract number: N00014-17-1-2087 for sintering effort and N00014-16-12778 for TEM). The effort at Rutgers University was supported by the U.S. Office of Naval Research (Contract number: N00014-15-1-2492).

4.1 Introduction

Flash sintering has demonstrated the ability to reduce furnace temperatures up to hundreds of degrees below conventional sintering temperature requirements and reduce the dwell time to as low as a few seconds [16]. This technique combines furnace heating and an applied electric field to achieve rapid densification, which occurs during a non-linear rise in current as the sample becomes conductive. Various ceramics have been successfully densified, including yttria-stabilized zirconia (YSZ) [16,185], TiO_2 [50,51,54], CeO_2 [45], $SrTiO_3$ [60,61], Co_2MnO_4 [186] and composite materials [94,187]. The mechanism(s) of flash sintering of ceramic materials has been extensively studied to understand the non-equilibrium nature during this rapid sintering process, including the implementation of various *in situ* characterization techniques [136,188] and development of multiscale modeling tools [18,127,140].

ZnO, an intrinsic n-type semiconductor, is one of the well-studied materials in flash sintering besides YSZ [19,20,31,34–39]. Previous studies of flash sintered ZnO have demonstrated that both the applied electrical field and current density significantly influence the grain growth

behavior [19]. One of the major challenges of flash sintering is the inhomogeneous microstructure due to non-uniform temperature and defect distribution [20,99,189]. The microstructure of flash sintered ZnO has been shown to be asymmetrical [20] due to different grain growth mechanisms across the samples, including electrochemical and Peltier effects [54,102].

Recently, several studies investigated the mechanisms of flash sintering by comparing with conventional sintering at different temperature ramp rates. Ultra-fast firing demonstrated the ability to increase the rate of sintering by over two orders of magnitude by increasing the heating rate [36,126]. On the other hand, another study compared slow flash sintering with conventional sintering and observed similarities in densification rate and microstructure [61]. Controlling current density ramping rate is a unique approach to control the flash sintering process and investigate the effect of such abrupt increase in current. The current ramp control is performed by gradually increasing the current density limit rather than allowing for the abrupt rise in current density in typical flash sintering experiments.

In this study, a detailed microstructure comparison was performed on the flash sintered ZnO samples, with and without controlled current ramp, to elucidate the effect of the non-linear rise in current on the overall sintering process. A transmission electron microscopy (TEM) study was conducted for both positive and negative electrode regions in these samples with focuses on the grain size distribution, pore morphology and extended defects analysis. Currently there is no prior report on the extended defects in the microstructure of flash sintered ZnO. The microstructure characteristics in flash sintered samples were also compared with the samples sintered without applied field to explore the fundamental flash sintering mechanisms in ZnO.

4.2 Experimental methods

To prepare the green body for flash sintering, ZnO powder (Sigma Aldrich, < 100 nm particle size) was uniaxially pressed under 150 MPa load into cylindrical pellets in a stainless steel die. The compacts measured approximately 3 mm in height and 6 mm in diameter, with a green density of 55-60%. The green pellets were loaded into a stage with platinum electrodes attached to the flat faces and heated up to the pre-flash temperature of 700 °C at a heating rate of 10 °C/min. A small pressure of 10 kPa was used to maintain consistent electrical contact between the sample and electrodes. An electric field of 60 V/cm was applied across the sample once the pre-flash temperature was reached. After the onset of flash sintering began, the current density rose until reaching the preset limit of 10 A/cm^2. The power source was switched from voltage control to current control and the current density was held constant for 60 s. Subsequently, the power supply was shut down and the furnace was cooled to room temperature.

For the current ramp sample, a sufficiently higher electric field (120 V/cm) was applied to initiate a sufficiently rapid feedback loop of temperature and conductivity for the current ramp initiate. The power supply was switched into current control mode, where the electric field rapidly dropped to maintain a linear current ramp. A current ramp rate of 0.1 A/cm^2/s was maintained until the current density limit of 10 A/cm^2 was reached, which took approximately 95 s. The current was held at 10 A/cm^2 for 10 s to ensure the electric energy used in both experiments were approximately the same. A sample without an applied field was sintered to 1100 °C at a heating rate of 10 °C/min and held for 60 s before cooling.

Table 4.1 summarizes the experimental conditions for all the sintered ZnO samples. The final densities were measured using the Archimedes method. The samples were sectioned to prepare plan-view TEM samples, with manual grinding, polishing, dimpling and final polishing in

an ion milling system (PIPS II, Gatan). Microstructure characterization was performed using an FEI TALOS 200X TEM operated at 200 kV. The average grain size was measured by direct measurements of 100 grains from multiple TEM images for each sample.

Table 4.1 Summary of experimental conditions.

Sample	**Furnace Temperature (°C)**	**Initial Electric Field (V/cm)**	**Current Density Limit (A/cm^2)**	**Current Density Ramp ($A/cm^2/s$)**	**Holding Time (s)**	**Final Density**
Flash Sintering	700	60	10	-	60	95%
Current Ramp	700	120	10	0.1	10	95%
No Applied Field	1100	-	-	-	60	94%

4.3 Results and discussion

The electric field, current density, power density and linear shrinkage plots for flash sintering and current ramp are shown in Figure 4.1. The power density plot shows a power spike reaching ~600 W/cm^3, which is typical for flash sintering and is created during the switch from voltage to current control. The majority of the linear shrinkage for flash sintering occurred during the non-linear increase in the current density as the sample becomes conductive. During the 60 s hold at the current density limit a small linear shrinkage was observed. The small spike in electric field and power density observed around 25 s was due to contact resistance, where the shrinkage resulted in the temporary reduction of contact with the electrodes. Regardless, the electrical field across the sample was sufficient to maintain the desired current during the current control stage. On the other hand, the sample under the controlled current density ramp did not experience a power

spike and thus consequently experienced a slower heating rate. The conductivity, however, increased linearly and reached higher values than that of the flash sintered ZnO at the end of 105 s. A gradual increase in linear shrinkage over a 105 s time period occurred rather than an abrupt densification over approximately 6 s for the flash sintered sample. More minor spikes were observed due to a higher probability of contact resistance as a result of continuous changes in sample dimensions.

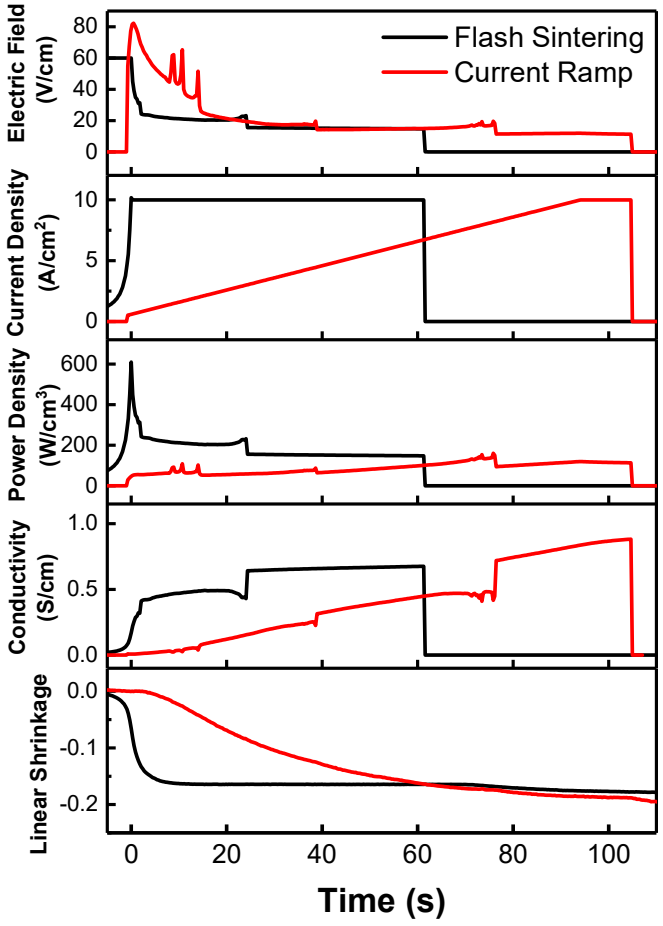

Figure 4.1 Plots of electric field, current density, power density, conductivity and linear shrinkage during flash sintering of ZnO with and without a controlled current ramp.

Figure 4.2 shows the TEM micrographs of flash sintered and controlled current ramp sintered ZnO at both positive and negative regions with their corresponding diffraction patterns. The average grain size and porosity analyzed from the micrographs are summarized in Table 4.2. To explore the microstructural differences, the positive and negative regions of both the current ramp and flash sintered samples are shown. It is notable that both flash sintered and controlled current ramp ZnO did not exhibit obvious differences in grain size between the positive and negative regions. The flash sintered sample had finer grains (average grain size of ~1.3 μm) at both electrodes compared to the current ramp sample (average grain size of ~1.7 μm). This grain size distribution was also confirmed by the diffraction patterns, where the larger grain size in the current ramp sample produced more distinguished diffraction spots. Another interesting observation is that the flash sintered ZnO had several diffraction spots which are very close together, as marked by the blue circles. The controlled current ramp sample overall had more scattered and distinguished diffraction spots. This suggests that multiple grains with similar orientations exist in the sample in the case of the flash sintered sample.

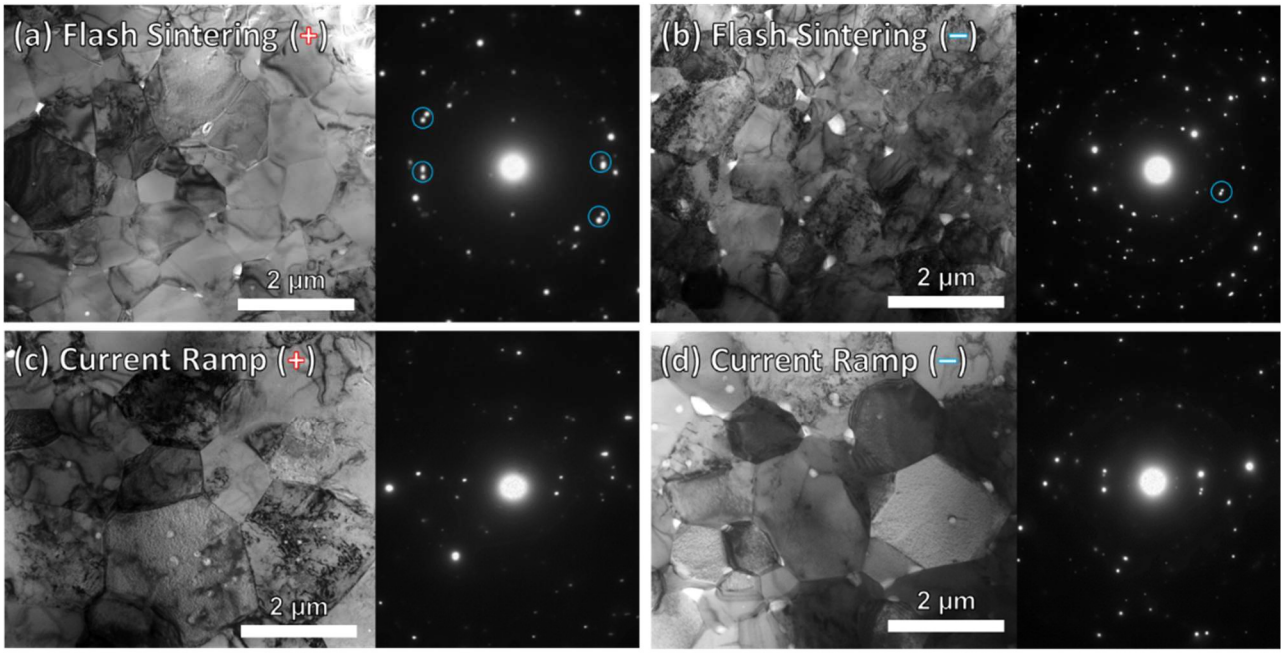

Figure 4.2 TEM micrographs of ZnO after (a)-(b) flash sintering and (c)-(d) current ramp on the positive and negative ends respectively, with their corresponding diffraction patterns. The blue circles mark diffraction spots which are very close together, suggesting subgrain texturing.

Table 4.2 Final density, grain size and porosity of ZnO after flash sintering and current ramp sintering. The grain size and porosity are measured from TEM micrographs.

Sample	**Grain size (μm)**		**Porosity (%)**	
	+	-	+	-
Flash Sintering	1.1 ± 0.2	1.1 ± 0.2	0.34	1.10
Current Ramp	1.5 ± 0.2	1.6 ± 0.3	0.21	0.99

Although there was no obvious difference in grain size between the two electrode regions, the pore content and distribution are quite different for the two electrode regions. Specifically, the amount of porosity was found to be much higher in the negative region than the positive region for both flash sintering and current ramp samples. Additionally, the pore morphology is quite different between the two samples and the two electrode regions. Figure 4.3 compares the microstructure at a higher magnification for a clear comparison of the intergranular porosity (i.e., pores between grains or at triple junctions) and intragranular porosity (i.e., pores within grains). The positive region of the flash sintered ZnO, as shown in Figure 4.3(a), has very low porosity (0.3%), mostly consisting of intergranular porosity and very few intragranular pores. On the negative electrode region, there is approximately 1.1% of porosity, which is also predominantly intergranular porosity with some intragranular porosity. The current ramp sample demonstrated a similar porosity difference in the positive and negative regions. However, there were many more intragranular pores, especially at the positive electrode region, as illustrated in Figure 4.3(c) where many entrapped pores have been observed in a single grain. The negative electrode region of the current ramp sample (Figure 4.3(d)) had an equal distribution of intergranular and intragranular porosity.

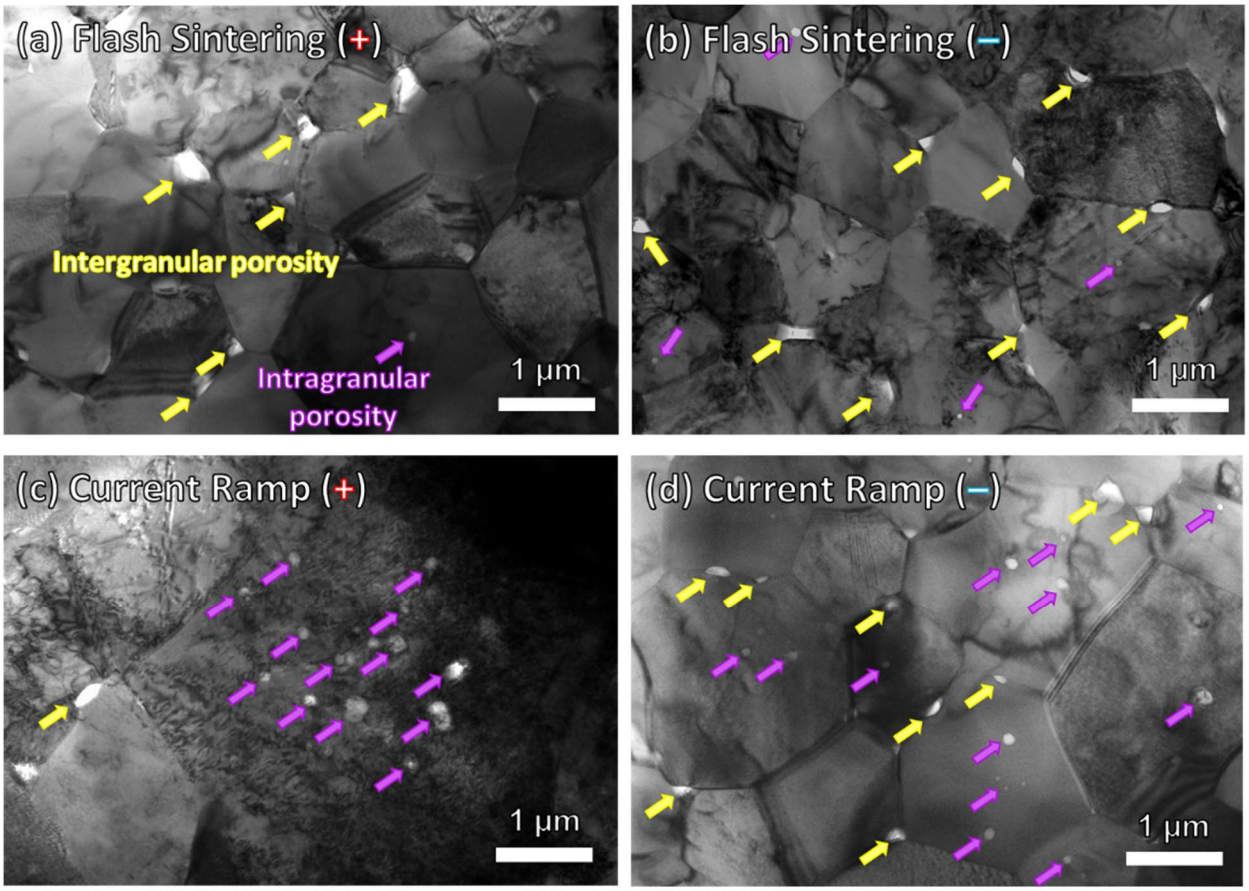

Figure 4.3 Difference in pore morphology in ZnO after (a)-(b) flash sintering and (c)-(d) current ramp at the positive and negative ends respectively. The yellow arrows mark intergranular pores and the purple arrows mark intragranular pores.

The comparison of the flash sintering and current ramp ZnO samples at the isothermal furnace temperature shows clear differences in grain size and pore morphology. Although using a controlled current ramp did not experience as high as the maximum power dissipation of the flash sintered sample, it has led to larger grain sizes. Based on sample temperature estimations using the blackbody radiation (BBR) model and *in situ* XRD lattice expansion, the sample temperature achieved by the flash sintered ZnO should be higher due to the higher power dissipation. The BBR

model has been commonly used to estimate sample temperatures during flash sintering [38,118,134,136]. The sample temperature can be estimated through the following equation:

$$T_{sample} = \left[{T_{furnace}}^4 + \frac{W_v V}{\varepsilon \sigma A} \right]^{1/4}$$

where W_v is the power dissipation (W/cm^3), V is the volume (cm^3), ε is the emissivity (assumed 0.8), σ is the Stefan-Boltzmann constant (5.67 x 10^{-8} Wm^{2}K^{-4}) and A is the surface area (cm^2). Assuming isotropic contraction and homogenous temperature of the sample, the sample temperature can be estimated using the power density and linear shrinkage data. Figure 4.4 compares the sample temperature of the flash sintered ZnO with and without current ramp using the BBR model.

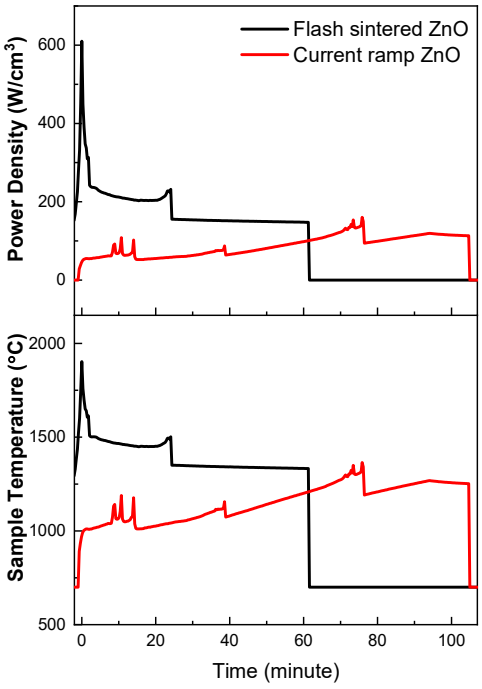

Figure 4.4 Power density and the corresponding sample temperature estimation based on the BBR model.

Based on the *in situ* XRD study by Charalambous *et al.* [S4], the dependence of sample temperature on power density plot was determined, as shown in Figure 4.5. The lattice expansion with varying current density limits (0, 5, 10, 15, 20, 25, and 30 A.cm^{-2}) was correlated to the conventional lattice expansion during conventional heating. A parabolic function was used to fit the steady-state power density to specimen temperature as follows:

$$T = -1.997 * 10^{-3}P^2 + 1.933P + 810.8$$

A discrepancy between the lattice expansion and the temperature approximation using the blackbody radiation model is clearly evident.

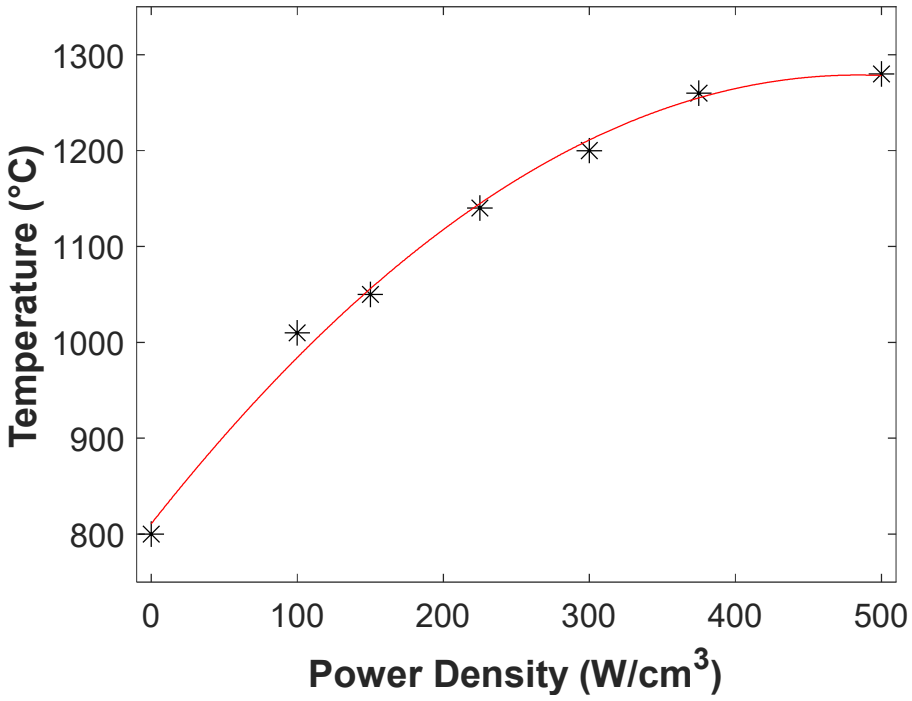

Figure 4.5 Sample temperature estimated based on power density by *in situ* XRD lattice expansion study [38].

Hence, the observed microstructural differences can be attributed to the rate of heating experienced by the samples. The power spike in flash sintering allows for a more rapid heating of the sample, and hence accelerating the densification process over grain growth. A clear indication of rapid heating is the limited grain coarsening and the small concentration of intergranular pores. Additionally, during the steady state of the current holding period, the intergranular pores cause pore drag which limits the grain growth and produces a finer grain structure for the flash sintered ZnO. The intragranular porosity found in the controlled current ramp is an indication of pore breakaway during grain growth as the boundary migration velocity exceeds the pore migration velocity [1]. This is typically observed when the pore mobility increases as the pore shrinks due to densification. The gradual densification process in the current ramp increases the probability of pores separating from the boundaries, leading to high intragranular porosity. Once the pores are separated, grain growth can occur more easily, which further supports the observation of the larger average grain size in the current ramp ZnO.

In a prior study on flash sintered ZnO, asymmetric grain sizes between the electrodes were reported due to potential induced abnormal grain growth at the anode [20]. This study could not demonstrate such difference in grain size since the electric field used was significantly lower. Nonetheless, the difference in pore content between the electrodes clearly suggests a dissimilar densification rate. Similar temperature gradients have been observed in flash sintered TiO_2, which is another n-type semiconductor, based on *in situ* EDXRD study [55]. This was attributed to the Peltier effect, where an electric current passing through a junction leads to heating and cooling effects. Based on the porosity difference between electrodes for both with and without controlled current ramp, the Peltier effect could be responsible for the difference in densification rate at the positive and negative electrodes.

Figure 4.6(a) and (b) shows the TEM images of the flash sintered and current ramp ZnO samples compared with a conventional sintered ZnO without applied electrical field (Figure 4.6(c)). High density stacking faults which are representative characteristics of the flash sintered and current ramp ZnO. The stacking faults shown here are from the positive electrode region. The negative regions in both flash sintered and current ramp samples (not shown here) also show obvious stacking faults. Stacking faults are planar defects caused by changes of atomic plane stacking sequence and are found in multiple grains for the flash sintered sample, as marked by the orange arrows in Figure 4.6(a). These stacking faults exist across the grains, i.e., begin and terminate at grain boundaries of a single grain. The current ramp ZnO also demonstrated multiple stacking faults in a grain, as shown in Figure 4.6(b), along with bands made up of short stacking fault segments going across the grain. To identify if the presence of extended planar defects was due to an applied field, the microstructure of a ZnO sample sintered without any applied field was compared. The sintering temperature selected was higher than the flash sintering ones, since a previous *in situ* energy dispersive X-ray diffraction (EDXRD) predicted the temperature at 10 Figure 4.6(c), illustrates reasonable densification without any apparent extended defects. It may be possible that defects can be annihilated due to more intensive grain growth which occurred in the sintered sample without field (average grain size ~3.1 μm). However, high density stacking faults remained even after significant grain growth in flash sintered titania [55], which confirms the formation of stacking faults due to the applied field.

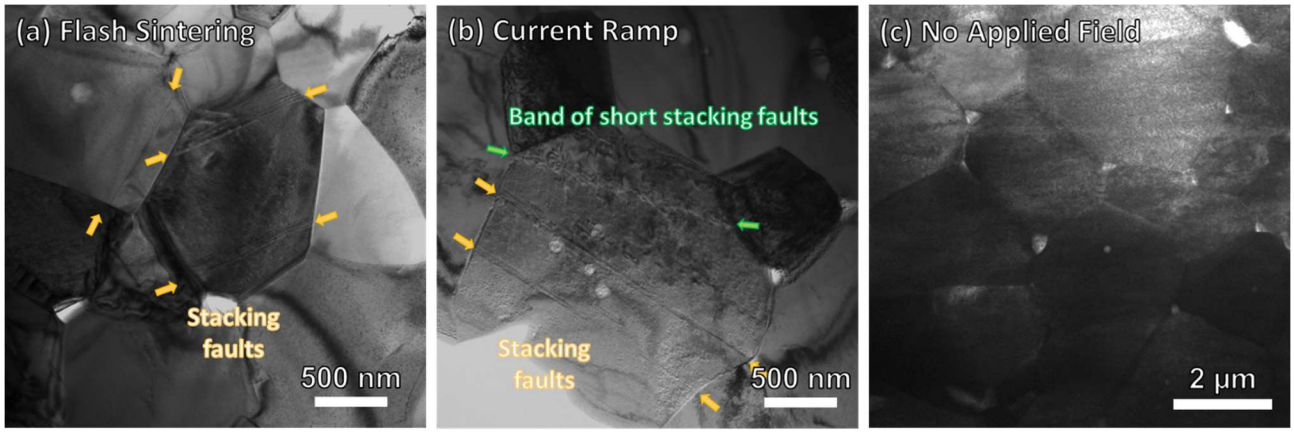

Figure 4.6 Representative micrographs of the extended defects present in the (a) flash sintered and (b) current ramp ZnO. The orange arrows indicate stacking faults while the green arrows mark a band of short stacking faults. (c) The microstructure of ZnO sintered without an applied field is poorly sintered with a larger grain size and does not contain any extended defects.

The flash sintered ZnO samples show microstructural similarities and differences compared to flash sintered YSZ ones. The diffraction pattern of flash sintered ZnO demonstrated clustered diffraction spots, i.e., several diffraction spots are very close to each other (Figure 4.2), indicating possible texturing of subgrains. A similar local texturing phenomenon has been reported in flash sintered YSZ [121]. Based on the electron diffraction data, there is a stronger texture in the positive electrode region of the flash sintered ZnO compared to the negative side, which may suggest the involvement of additional mechanisms at the positive side to assist in the densification process. The diffraction patterns of the current ramp ZnO did not show obvious texturing structure, which may imply the texturing phenomena are more pronounced in the flash sintering process.

Another difference in the features of ZnO compared to YSZ is the type of extended defects observed. Dislocation arrays were observed in the flash sintered YSZ microstructure [121,146], rather than stacking faults as shown for the case of ZnO. In ZnO thin films, the basal-plane stacking faults (i.e., (0001) plane stacking) are known to have very low formation energies [190]. As a

result, high density of stacking faults can be formed in ZnO thin films due to high point defect concentrations and consequently affect the overall electrical conductivity in ZnO [191]. A depth-resolved cathodoluminescence experiment on flash sintered ZnO has also demonstrated a higher increase in native point defects concentration within the grains compared to the grain boundaries after flash sintering [34]. This is expected as grain boundaries act as sinks for oxygen vacancies. Hence, extended defects such as stacking faults exist in the flash sintered and controlled current ramp samples due to an increase in the density of point defects and electrical conductivity introduced by the applied electrical field.

Evidently, the microstructure of ZnO sintered without any applied field did not reveal any extended defects compared to the flash sintered or controlled current ramp samples. In addition, the controlled current ramp sample also contained bands of short segments of stacking faults, which could be a consequence of the gradual increase in conductivity over a longer time during the current ramping process. Overall, the extended defects generated during the flash sintering process appear to be dependent on the nature of the materials and the defect formation energy for the materials. Further investigation of the types of extended defects present in other flash sintered ceramics under different sintering conditions and stages are critical for the study of fundamental mechanisms related to field assisted sintering.

4.4 Conclusions

In summary, the microstructure of flash sintered ZnO samples, with and without controlled current ramp were investigated and compared. Flash sintered ZnO produced fine grains by minimizing grain growth due to rapid densification during the non-linear increase in current. A controlled current ramp leads to gradual densification, resulting in larger grains with mostly

intragranular porosity. Consequently, more pores break away from the grain boundaries and accelerate grain growth. This comparison study signifies the importance of the nonlinear rise in current in order to achieve high density with fine gain structures. The applied field leads to the formation of stacking faults in both flash sintered and current ramp ZnO due to the generation of point defects during the field-assisted process.

CHAPTER 5. MICROSTRUCTURE AND DEFECT GRADIENTS IN DC AND AC FLASH SINTERED ZnO

This chapter contains text and figures published in a journal article titled "Microstructure and defect gradients in DC and AC flash sintered ZnO" by X. L. Phuah, B. Yang, H. Charalambous, T. Tsakalakos, X. Zhang & H. Wang, Ceramics International, in press. The original article has been modified to include information from the supplemental information of the published article.

The authors would like to acknowledge the support from the U.S. Office of Naval Research (Contract No N00014-17-1-2087 for the sintering effort and N00014-20-1-2043 for the TEM). H.C. and T.T. would like to acknowledge the support provided by the U.S. Office of Naval Research (Contract No. N00014-15-1-2492).

5.1 Introduction

Flash sintering has gained significant attention in recent years due to its ability to densify ceramics within seconds [16]. An electric field is applied directly across the ceramic during heating which leads to a nonlinear rise in conductivity and current flow through the ceramic. Consequently, the sample reaches a temperature above the furnace temperature due to the resultant Joule heating, with ultra-fast heating rates on the order of 10^3 – 10^4 °C/min [18,36]. Flash sintering has been successfully performed on a wide range of ceramics such as yttria-stabilized zirconia (YSZ) [16,121], ZnO [20,22,29,30], TiO_2 [54–56], CeO_2 [45,49] and multiphase systems [96,168].

The first demonstration of flash sintering utilized a direct current (DC) power supply to provide the electric field and current [16]. Since then, most flash sintering studies have continued to use DC power supplies despite the formation of asymmetric characteristics, such as grain size gradients and inhomogeneous reduction between the positive and negative electrodes [45,54,69,125]. This phenomenon occurs due to the charged characteristics of ionic ceramics, which causes redistribution of charged defects and temperature gradients after flash sintering [69,150,173,178]. In several cases, these defective features introduced by DC flash sintering has shown to enhance its properties, such as mechanical [26,57,146] and optical properties [29,30,192].

Shortly after DC flash sintering was first demonstrated, studies on alternating current (AC) flash sintering were reported [19,103,151,193]. Since the current direction switches direction periodically (Figure 5.1), this modification can avoid time-sensitive defect redistribution processes near an electrode and thus prevent asymmetric characteristics. Even for AC flash sintering, microstructure gradients have been observed from the interior to the surface of the ceramic due to the loss of heat via thermal conduction and blackbody radiation, which is inherent to an internal heating process [25,103,194]. To date, considerably less attention has been paid to the study of defect redistribution in AC flash sintered ceramics and their contrasting properties compared to DC flash sintering.

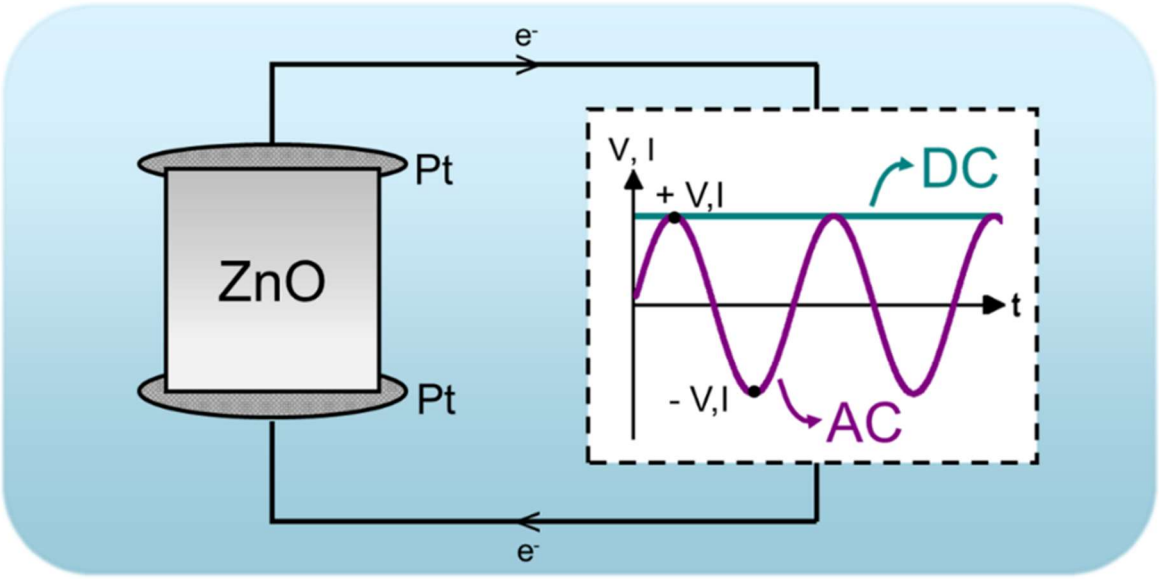

Figure 5.1 Schematic comparing the difference in voltage and current flow between direct current (DC) and alternating current (AC).

To compare DC and AC flash sintering, ZnO was selected in this work as it has been a key material for flash sintering [19,20,22,25,29,30,36,38] and also has many important technological applications for electronics, photonics, acoustics and sensing applications [179,195]. The first demonstration of flash sintering of ZnO by Schmerbauch et al. in 2014 utilized AC flash sintering [19], followed by numerous studies using DC flash sintering [20,22,29,30,36,38,39,173], and most recently studies by Liu et al. [25] and Storion et al. [32] reported AC flash sintering of ZnO. Many of these works have shown the existence of microstructure gradients in DC and AC flash sintering and they were studied separately without direct comparison. In addition, the studies focusing on defects analysis in flash sintered ceramics are very limited [19,29,30]. Thus, this direct comparison study between DC and AC flash sintered ZnO targeting the microstructure and defect gradients could elucidate the fundamental differences between the two methods. Detailed microstructure analysis was performed to obtain the grain size distribution and porosity in various regions of the DC and AC flash sintered samples. Raman spectroscopy was employed to investigate the structural disorder caused by defects correlated to the Zn and O sub-lattices in flash sintered ZnO. As the presence of defects would result in asymmetry in the Raman modes, the data was fitted using the Breit-Wagner-Fano (BWF) model to obtain the asymmetry parameter.

5.2 Experimental methods

5.2.1 Flash sintering

ZnO powder (Sigma Aldrich, < 100 nm particle size) was uniaxially pressed under 150 MPa into a cylindrical green body with 3 mm height and 6 mm diameter. The resulting green bodies were approximately 55% of theoretical density. Platinum electrodes were in contact with

the flat surfaces of the cylindrical green body using a small pressure of 10 kPa to maintain consistent electrical contact between the sample and electrodes. Platinum electrodes were connected to a DC power supply (Sorensen DLM 150-4) or AC (1000 Hz) power supply (Pacific Power 118-ACX) depending on the experiment. The green compacts were loaded into a stage and heated up to the pre-flash temperature of 700°C at a heating rate of 10°C/min. An electric field of 60 V/cm was applied across the sample thickness once the pre-flash temperature was reached. The current rapidly increased to the preset current density limit of 10 A/cm^2 and the power source was switched from voltage control to current control. The current density was held constant for 60 s and subsequently the power supply was shut down and the furnace was cooled to room temperature.

5.2.2 Characterization

The microstructure was characterized using a Thermo Fisher Quanta 650 FEG scanning electron microscope (SEM) on the fractured and polished surfaces. Grain sizes were measured using the linear intercept method based on a 300 grain statistical average for each region. The porosity area percentage was measured and averaged from 10 images. Raman analysis was performed using Renishaw InVia Raman MicroSpectroscopy equipped with a 532 nm wavelength laser.

5.3 Results and discussion

Figure 5.2(a) shows the plot of electric field (60 V/cm) and current density (10 A/cm^2) for the DC flash sintered ZnO along with the SEM of the fracture surface at the positive, middle and negative regions in Figure 5.2(b)-(d), respectively. Gradient microstructure can be observed, where the grain size was measured to be 1.84, 2.29 and 2.62 μm for the positive (+), middle (M) and negative (-) regions, respectively. For a more detailed analysis, the grain size distribution of each

region is shown in Figure 5.2(e)-(g). Along with the increasing grain sizes from the positive to negative electrodes, the broadening of the grain size distribution was also observed.

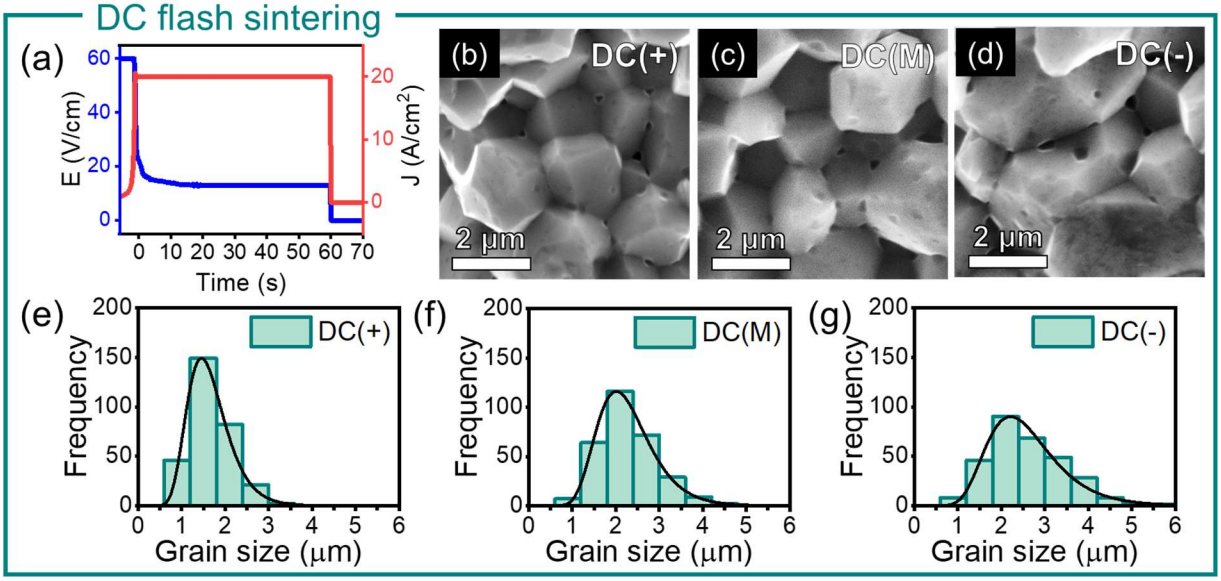

Figure 5.2 DC flash sintering of ZnO (a) electric field and current plots, (b)-(d) fracture surface SEM and (e)-(g) grain size distribution

AC flash sintering of ZnO was performed with the same furnace and electric field amplitude as those of the DC flash sintering sample, as shown in Figure 5.3(a). In contrast with DC flash sintered ZnO, AC flash sintered ZnO showed a very homogenous microstructure in Figure 5.3(b)-(d) among the different regions (E1 and E2 indicate the two opposing electrode regions). The grain sizes for E1, M and E2 are 1.42, 1.66 and 1.43 um, respectively. The middle region has a slightly larger grain size compared to the electrode ends, but the grain size differences are insignificant compared to the DC flash sintered ZnO. Moreover, the grain size distributions shown in Figure 5.3(e)-(g) are very similar among the different regions, further showing sample homogeneity.

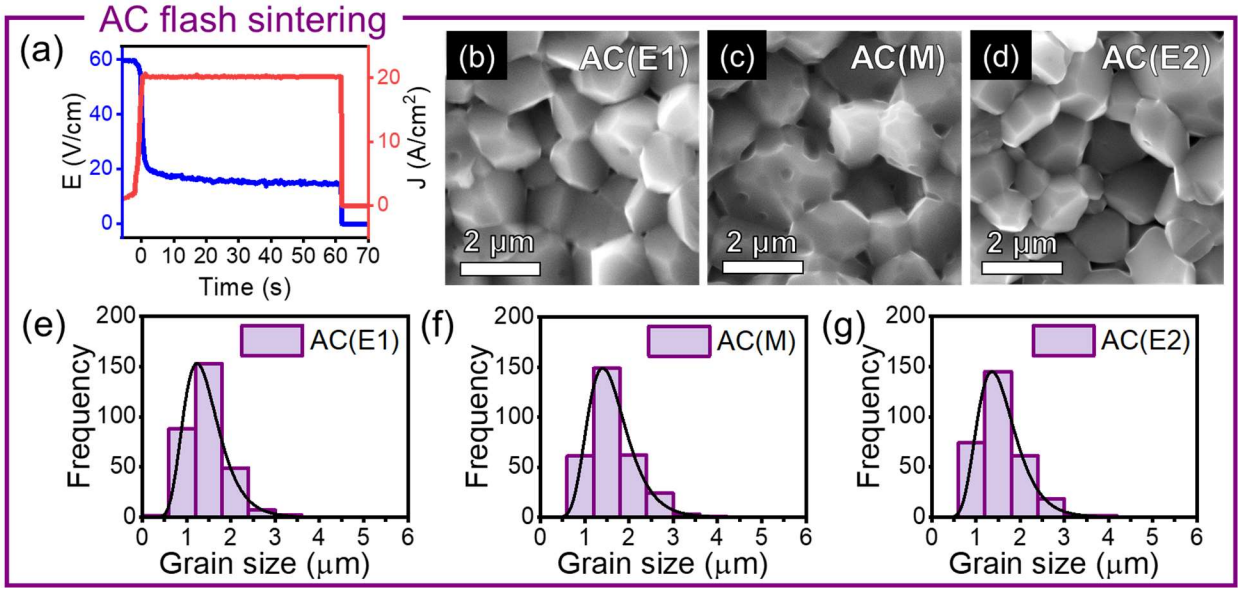

Figure 5.3 AC flash sintering of ZnO (a) electric field and current plots, (b)-(d) fracture surface SEM and (e)-(g) grain size distribution.

To directly compare DC and AC flash sintering, the average grain sizes and porosity percentages are shown side by side in

Figure 5.4. The gradient in grain size can be clearly observed in DC flash sintered ZnO, contrary to the AC flash sintered ZnO which was homogeneous throughout and had finer grain sizes. The porosity area percentage was also compared using polished surfaces (SEM images are shown in Figure 5.5). The DC sample also showed a gradient in porosity, where the positive side had the least porosity (1.0%) and the negative side had the most porosity (3.6%). The AC sample showed similar porosity throughout the sample comparable to the negative electrode of the DC sample (3.3%, 3.7% and 3.4%). Although the AC flash sintered ZnO sample was more homogeneous throughout, the densest region was found at the positive side of the DC flash sintered ZnO sample.

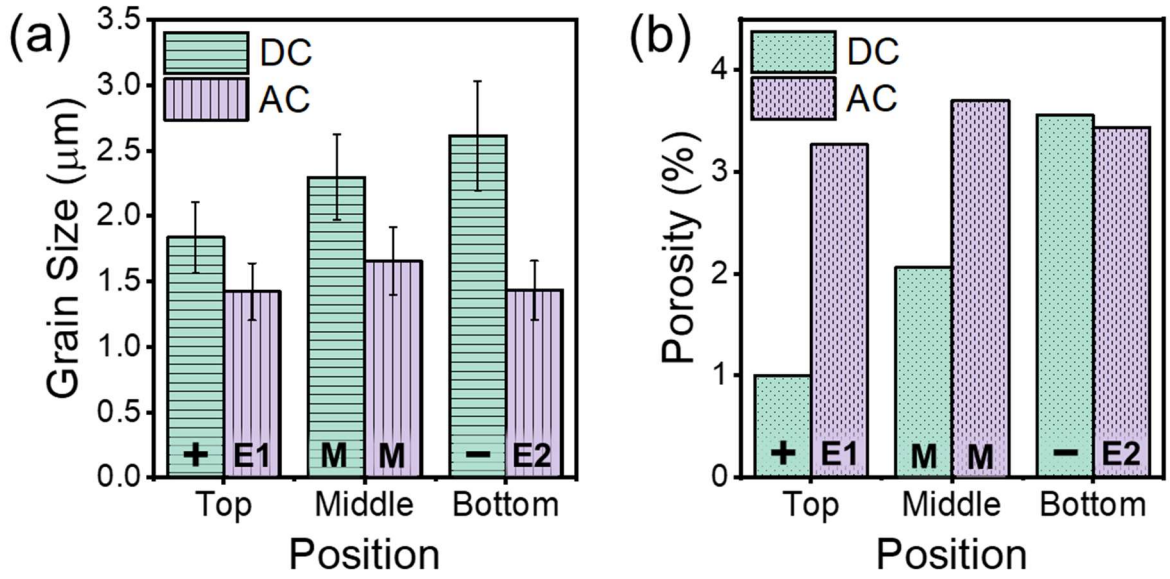

Figure 5.4 (a) Grain size distribution and (b) porosity percentage compared in the top, middle and bottom regions for DC and AC flash sintered ZnO.

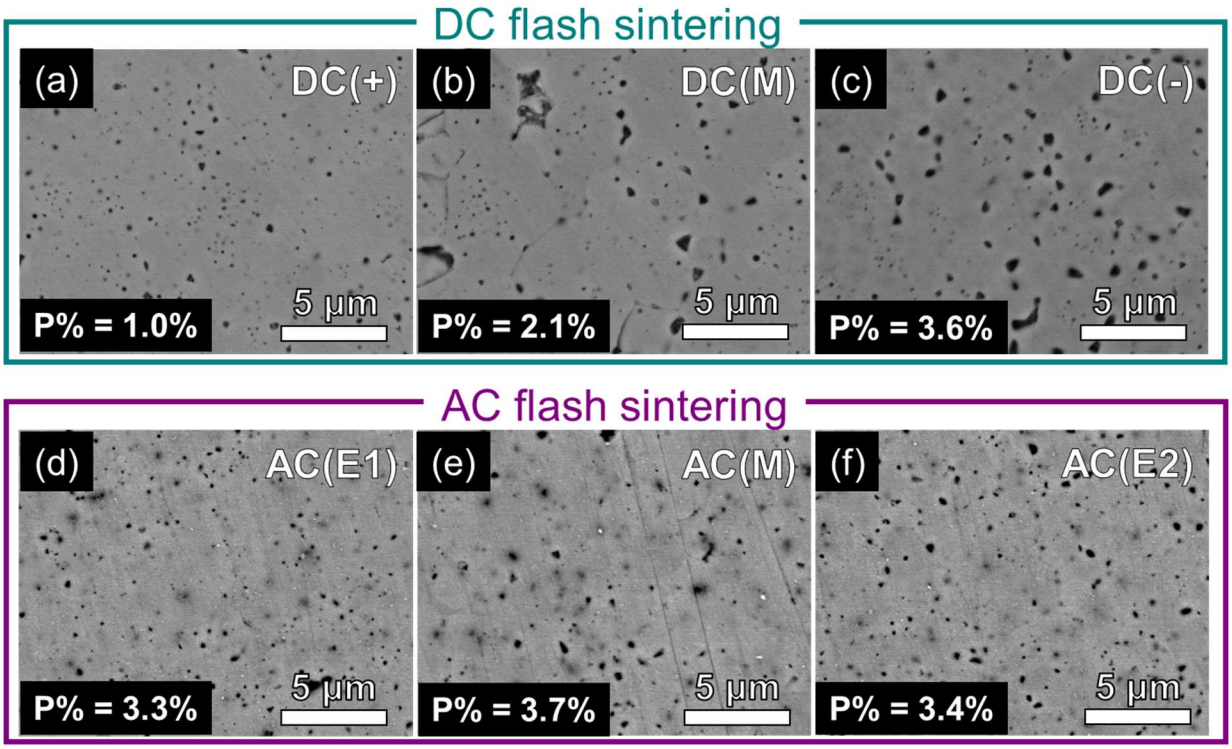

Figure 5.5 Polished surfaces of (a)-(c) DC flash sintered ZnO and (d)-(f) AC flash sintered ZnO.

The smaller grain sizes and higher porosity content observed in the AC flash sintered ZnO suggest that a lower sample temperature was reached compared to DC flash sintering. In order to estimate sample temperature, the blackbody radiation (BBR) model is often used with the assumption that all electrical power is converted into radiated heat [134,136]. The BBR model states:

$$T_{sample} = \left[T_{furnace}^{4} + \frac{W_v V}{\varepsilon \sigma A} \right]^{1/4}$$

where W_v is the power dissipation (W/cm^3), V is the sample volume (cm^3), ε is the emissivity, σ is the Stefan-Boltzmann constant (5.67×10^{-12} $W/cm^2 K^{-4}$) and A is the sample surface area (cm^2). Based on the power density curves shown in Figure 5.6, the sample temperatures were estimated through the BBR method for both DC and AC flash sintering of ZnO and shown in
Table 5.1. Since the emissivity is not known, the sample temperatures were estimated based on emissivity values of 0.5 and 0.9 to obtain a range of temperatures. For comparison, the sample temperature estimated through *in situ* energy dispersive X-ray diffraction (EDXRD) experiments for DC flash sintered ZnO is also shown in
Table 5.1 [38]. Even with different emissivity values, the sample temperature obtained from the BBR method is clearly overestimated and conflicting with the grain size difference between DC and AC flash sintered ZnO (i.e. higher temperature resulted in smaller grain size and vice versa). This inaccuracy is most likely caused by the assumptions of the model, which assumes that heat is dissipated through radiation only and the power dissipation is homogeneous throughout the sample.

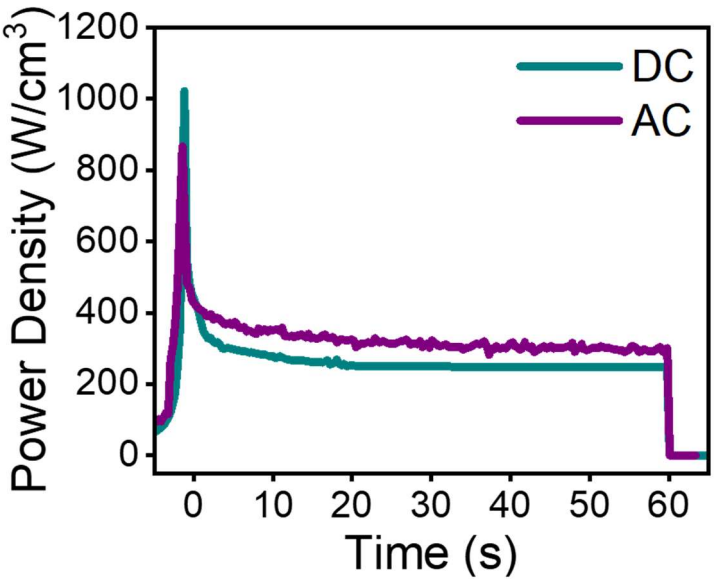

Figure 5.6 Power density curves for DC and AC flash sintering of ZnO.

Table 5.1 Sample temperatures estimated through blackbody-radiation (BBR) model, in situ energy dispersive X-ray diffraction (EDXRD) measurements and grain size extrapolation method.

Sample region	Sample temperature estimations (°C)			
	BBR (ε = 0.5)	BBR (ε = 0.9)	EDXRD (from ref. [38])	Grain size extrapolation
DC(+)	1845	1573	1260	1218
DC(M)				1231
DC(-)				1239
AC(E1)	1920	1636	-	1202
AC(M)				1212
AC(E2)				1203

There are other sample temperature measurement methods, such as thermocouples and infrared thermal imaging, which are possible to be integrated. However, measurements with sample contact are not possible due to interference with the electric circuit, while non-contact techniques are only effective in measuring the surface and local temperatures which could be inaccurate for large cylindrical samples. Thus, for this study, we employed grain size extrapolation from conventionally sintered samples to estimate the effective sample temperature of DC and AC flash sintered samples. Figure 5.7(a) shows the heating profile of the conventionally sintered samples, where the temperature was first increased to 700°C at 10°C/min, followed by a rapid increase to a higher maximum temperature at 25°C/min, which is the maximum heating rate of the furnace. This specified heating profile would more accurately represent the sample temperature experienced during flash sintering, rather than a linear temperature increase. As shown in Figure 5.7(b), the average grain sizes were obtained for the conventionally sintered samples and fitted to an exponential equation. This equation will enable sample estimations based on the measured grain sizes of the flash sintered samples. The results obtained from the grain size extrapolation method are shown in Table 5.1 with the other estimated sample temperatures. As the estimated temperatures obtained from this method are much more comparable to the *in situ* EDXRD results [38], the sample temperatures are likely more accurate compared to the BBR method. The grain size extrapolated temperatures also revealed a slightly higher sample temperature for DC flash sintered ZnO compared to AC flash sintered ZnO. The temperature differences are not very significant for the grain size differences observed, mainly because the temperature regime has a very steep grain growth rate.

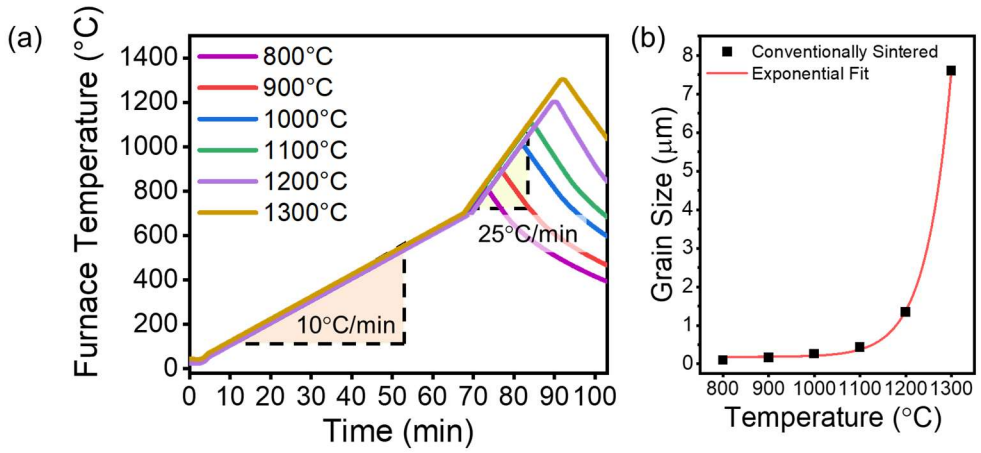

Figure 5.7 (a) Heating profile for conventionally sintered ZnO and their (b) average grain sizes.

It is also possible that the grain size differences are contributed by nonthermal effects, such as defects redistributions. A study by Conrad and Yang observed differences in grain growth behavior due to the influence of DC and AC electric fields on the grain boundary structure [196]. Several studies have also shown space charge effects in DC flash sintered ceramics, such as 3YSZ [121] and $SrTiO_3$ [69], which have impact on the microstructure gradient. However, this relationship is not well understood for ZnO and the microstructure gradients are typically less severe compared to other flash sintered oxides. Thus, Raman spectroscopy was employed in this study to detect crystal lattice disorder contributed by point defects. Figure 5.8 shows the Raman spectra for the DC and AC flash sintered ZnO samples as well as the ZnO sample conventionally sintered at 1200°C, which most closely matches the estimated sample temperature of the flash sintered samples. The prominent vibrational modes observed in all samples were E_2^{low} at 99 cm^{-1} and E_2^{high} at 439 cm^{-1}. The E_2 modes are non-polar, where E_2^{low} is associated with the vibrations of

the Zn sublattice while E_2^{high} mode is correlated to the O sublattice [197]. Other minor peaks in the spectra include E_2^{high}- E_2^{low} at 334 cm^{-1}, $A_1(TO)$ at 379 cm^{-1} and $E_1(TO)$ at 410 cm^{-1}.

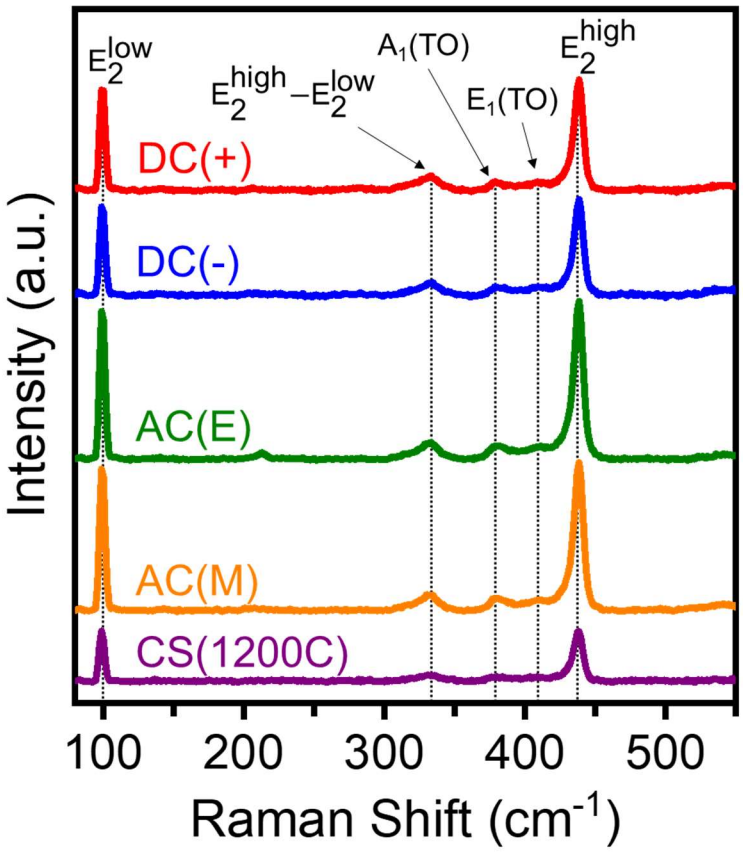

Figure 5.8 Raman spectra of AC and DC flash sintered ZnO at various regions and conventionally sintered ZnO at 1200°C.

The symmetry of the E_2^{low} and E_2^{high} peaks is highly sensitive to any variation to the lattice structure such as stress, defects and impurities. A Breit-Wigner-Fano (BWF) function has been commonly utilized to obtain the line-width, asymmetry parameter and Raman shift [184,198]. The BWF function is expressed as:

$$I(\omega) = I_0 \frac{\left[1 + \frac{2\beta(\omega - \omega_0)}{\Gamma_0}\right]^2}{1 + \left[\frac{2(\omega - \omega_0)}{\Gamma_0}\right]^2}$$

where $I(\omega)$ is Raman intensity, I_0 is the maximum intensity, ω is the Raman shift, ω_0 is the Raman shift peak frequency at maximum intensity, Γ_0 is the full width at half maximum (FWHM) and β is the asymmetry parameter ($\beta = 0$ gives a symmetric profile). Figure 5.9(a) and (b) show the BWF fitting for all the samples for the E_2^{low} and E_2^{high} peaks while the fitted parameters were compiled in Table 5.2.

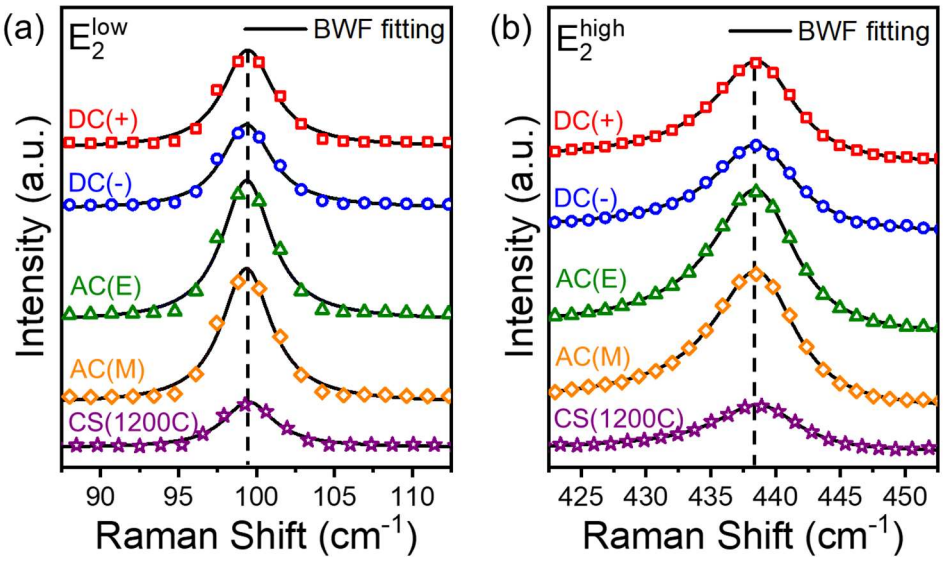

Figure 5.9 Fitting of (a) E_2^{low} and (b) E_2^{high} peaks (open symbols) using Breit-Wigner-Fano (BWF) model (line).

Table 5.2 Parameters obtained from fitting the Raman E_2^{low} and E_2^{high} peaks.

Sample (region)	E_2^{low}			E_2^{high}		
	ω_0	Γ_0	β	ω_0	Γ_0	β
DC(+)	99.406	1.974	0.00933	438.900	3.783	-0.05566
DC(-)	99.310	1.956	0.01217	438.893	3.832	-0.05391
AC(E)	99.349	1.944	0.00626	438.834	3.822	-0.05561
AC(M)	99.328	1.939	0.00699	438.886	3.841	-0.05629
NF(1200C)	99.454	1.976	0.00707	439.062	3.938	-0.06007

Based on the relative values of the asymmetry factor, the Raman shift and FWHM values were comparable between the flash sintered samples, but the asymmetry factor for E_2^{low} peak was higher in the DC flash sintered sample compared to the AC flash sintered sample, especially in the negative region. The higher deviation for the asymmetry factor from zero indicates a larger distortion of the Zn sublattice, possibly due to a higher concentration of Zn interstitials. The redistribution of Zn interstitials towards the negative electrode in ZnO under an electric field has been previously reported by Korsunska *et al.* [199]. Due to the waveform of AC, the redistribution of defects did not occur and thus resulted in a similar asymmetry factor compared to the conventionally sintered sample.

For the E_2^{high} peak corresponding to the O sublattice, all samples showed much larger asymmetry factors compared to the E_2^{low} peak. As the E_2^{high} peak is correlated to oxygen sublattice, a high asymmetric factor suggests that oxygen vacancies are the dominant defects in sintered ZnO. Similar observations have been consistently reported in studies which investigated the defects present in conventional and flash sintering of ZnO [30,184,200]. Comparable E_2^{high} asymmetry

values were found for AC and DC flash sintered samples at all positions, suggesting that the concentration of oxygen vacancies was comparable for both samples.

Overall, the DC flash sintered sample showed both microstructure gradients and defect redistribution, with a fine-grained and dense positive side. This may be an advantageous processing parameter for applications which require such gradient structure. For example, the development ZnO varistors have shown the necessity for gradient structures to obtain large voltage gradients for device minimization [201]. Another potential benefit of the gradient ZnO structure include thermoelectric applications, which is able to help optimize both high efficiency and enhance lifetime [202]. In addition, the positive region of the DC flash sintered ZnO showed the densest microstructure in this study with minimal grain growth and high density defects. This region could be ideal for specific applications, such as mechanical properties, as demonstrated in previous work by Cho et al. [26].

On the other hand, AC flash sintering produced a sample with minimal grain size gradient and no defect redistribution. It is clear that AC flash sintering is ideal for processing of homogeneous ceramics with similar properties to ceramics produced using traditional methods. Moreover, additional parameters in AC flash sintering such as the frequency [203] and waveform [65] can be employed to optimize the densification process. Further detailed investigations into the impact of these parameters on the material properties of a wide variety of material systems are needed in order to scale up AC flash sintering of ceramics.

5.4 Conclusions

This study provides a comparison of the microstructure of DC and AC flash sintered ZnO samples, along with detailed defects analysis through Raman spectroscopy. The grain size and porosity increased from the positive to the negative electrode in DC flash sintered ZnO, while the

AC flash sintered ZnO was mostly homogeneous in grain size and porosity. Along with the gradient microstructure, DC flash sintered ZnO also showed defect redistribution with a preferred accumulation of Zn interstitials near the negative electrode. On the contrary, the defect characteristics of AC flash sintered ZnO showed no obvious difference compared to a conventionally sintered sample. Based on their contrasting characteristics, DC and AC flash sintering can be used for various applications depending on their preferred microstructure and defects.

CHAPTER 6. FIELD-ASSISTED GROWTH OF ONE DIMENSIONAL ZnO NANOSTRUCTURES WITH HIGH DENSITY DEFECTS

This chapter contains text and figures published in a journal article titled "Field-assisted growth of one dimensional ZnO nanostructures with high density defects" by X.L. Phuah, J. Cho, Akriti, L. Dou, W. Rheinheimer, X. Zhang & H. Wang, Nanotechnology, 2020, 32, 095603. The original article has been modified to include information from the supplemental information of the published article.

The authors would like to acknowledge the support from the U.S. Office of Naval Research (Contract number: N00014-17-1-2087 for sintering effort and N00014-20-1-2043 for TEM). W.R. thanks the German Research Foundation for support under grant no. HO 1165/20-1 within the priority programme SPP1959 and grant no. Rh 146/1-1 within the Emmy Noether programme. Akriti acknowledges support from the Frederick N. Andrews Fellowship. L. Dou acknowledges support from Davidson School of Chemical Engineering of Purdue University.

6.1 Introduction

One-dimensional (1D) nanostructures have been immensely studied due to their well-defined crystalline orientation and high surface area to volume ratio. Among the various 1D materials studied, ZnO is one of the most widely used in a key technological applications. ZnO is a n-type seminconductor with a wide band gap and large exciton binding energy, which are excellent properties for optoelectronics and luminescence applications. ZnO also possesses a non-centrosymmetric hexagonal wurtzite structure, resulting in strong piezoelectric and pyroelectric properties. Various types of 1D nanostructures have been reported for ZnO, including nanowires [204–206], nanorods [207–210], nanotubes [211,212], nanobelts [213] and nanoribbons [214].

Engineering defects into 1D nanostructures can significantly impact the existing properties. In previous studies, presence of stacking faults in ZnO nanowires have shown to change the local band structure and mechanical properties [215,216]. However, growing defective 1D nanostructures is extremely challenging because defects are very likely to migrate to the surface and annihilate [213]. Additionally, most of the employed growth techniques are equilibrium

processes, which produced defect-free 1D nanostructures [217,218]. Thus, finding new non-equilibrium techniques to grow defective 1D nanostructures is highly desirable.

Flash sintering is a new field-assisted sintering technique where bulk ceramics are densified with the aid of an electric field and current [16]. At a certain combination of furnace temperature and electric field strength, the ceramic will become conductive and flow current through the sample. This results in rapid densification of the ceramic within seconds at a much lower furnace temperature than conventional sintering temperature. The sample usually undergoes ultra-high heating and cooling rates resulting in unique characteristics due to the impact of point defects [69,126,127]. As a result, many non-equilibrium features have been observed such as dislocations, stacking faults and metastable phases [22,121,157,188].

In this study, flash sintering of ZnO was performed using an electric field of 600 V/cm with a set current density limit of 2 A/cm^2. Due to the extremely fast densification and the high electric power dissipation, fracture occurred parallel to the electrodes. Along the current path, a hot spot with local melting and cavitation occurred. These sintering conditions led to growth of high density and well-aligned nanorods on the fractured surface around the hot spot. This demonstration presents the unexpected capability of flash sintering to form ZnO nanostructures without any additional catalyst, seed, template, single crystal substrate, Zn precursor or reducing agent. The non-equilibrium characteristics of flash sintering led to the formation of high density of defects in the ZnO nanostructures, which were further investigated by transmission electron microscopy and photoluminescence.

6.2 Experimental methods

6.2.1 Flash sintering

ZnO nanopowder (US Research Nanomaterials Inc) with average particle size of 18 nm was uniaxially pressed into cylindrical green bodies using a pressure of 350 MPa. The green body dimensions were 6 mm in diameter and 3 mm in height, with an approximate green density of 60 %. The sample was placed between two Pt coils in a horizontal dilatometer (TA Instruments DIL 801) to apply an electric field during the experiment. Due to the complex temperature profile of flash sintering, the shrinkage could not be corrected for the thermal expansion of the dilatometer. The furnace heated at 25°C/min up to 900°C while an electric field of 600 V/cm was applied across the sample via platinum wires and coils (Figure 6.1(a)). The electrical contacts were connected to a power supply (Sorensen DLM 300-2). As the sample becomes conductive, current will start flowing through the sample and the power supply will be switched from voltage to current control mode. For this study, the current density limit was set to 2 A/cm^2 and the steady state current was held for 60 seconds before turning off the power supply. The furnace was cooled after reaching the furnace temperature of 900°C.

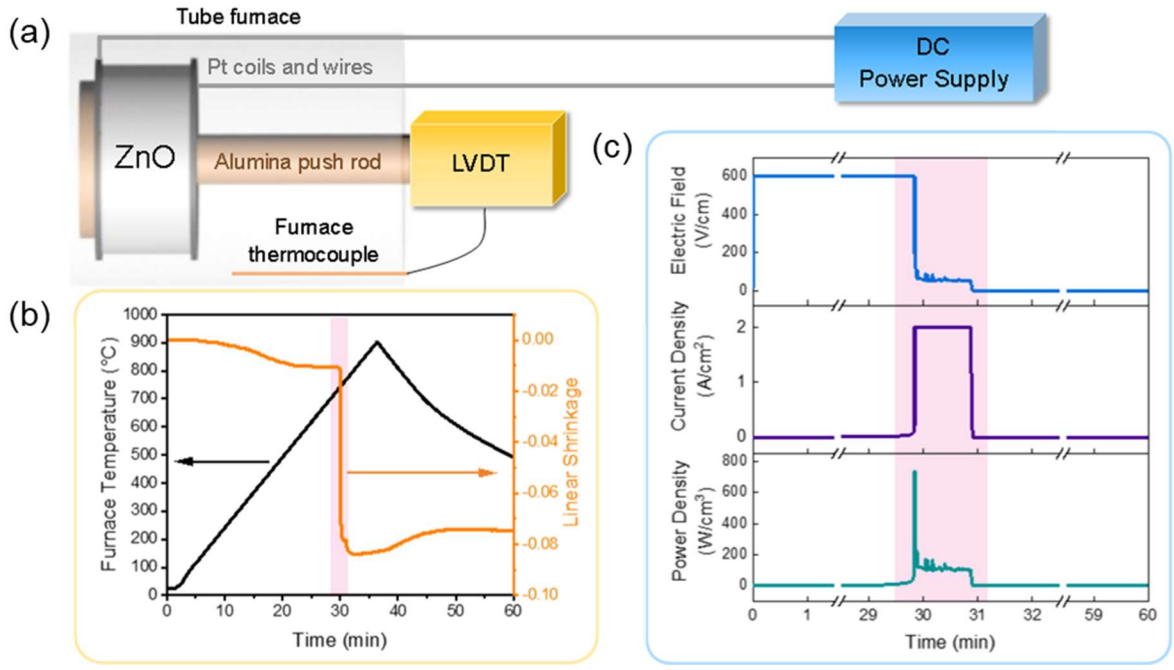

Figure 6.1 (a) Schematic of the flash sintering setup in a horizontal dilatometer. (b) Plot of the furnace heating profile and shrinkage measured by the push rod in the dilatometer. (c) Electrical data collected from the power supply during flash sintering. Note the different scale of the x-axis.

6.2.2 Characterization

X-ray diffraction (XRD) was performed on the top and bottom of the specimens, as well as the fractured surface using a PANalytical Empyrean using Cu-kα radiation (λ = 0.154 nm). The microstructure was characterized by a Quanta 650 FEG scanning electron microscope (SEM) on the fractured surfaces and FEI Talos 200X transmission electron microscope (TEM) for the nanostructures. The TEM sample was prepared by focused ion beam (FIB) sectioning, followed by lift-out and thinning for electron transparency. Photoluminescence (PL) was performed at room temperature using a Coherent OBIS laser with a wavelength of 375 nm and collected by a SpectraPro HRS-300 spectrometer.

6.3 Results and discussion

6.3.1 Flash sintering of ZnO

Figure 6.1(a)-(c) show the experimental setup, along with the data collected from the dilatometer and power supply. As the sample was heated to 900°C, an electric field of 600 V/cm was applied across the sample. After around 30 minutes, fast linear shrinkage by about 8 % (Figure 6.1(b)) and simultaneously rapid increase in current density occurred (Figure 6.1(c)). The power supply immediately switched from voltage to current control when it reached the current density limit of 2 A/cm^2. During this event, a large power spike was produced, as observed in the power density plot. The electric field dropped to maintain the steady state current which was held for 60 seconds before turning off the power. A sample without an applied field ("no-field", Figure 6.2) achieved only 5 % linear shrinkage after reaching 900°C. Moreover, the shrinkage occurred at a much more gradual rate compared to the flash sintered sample. Hence, the additional Joule heating and temperature increase from flash sintering helped to rapidly densify the green body.

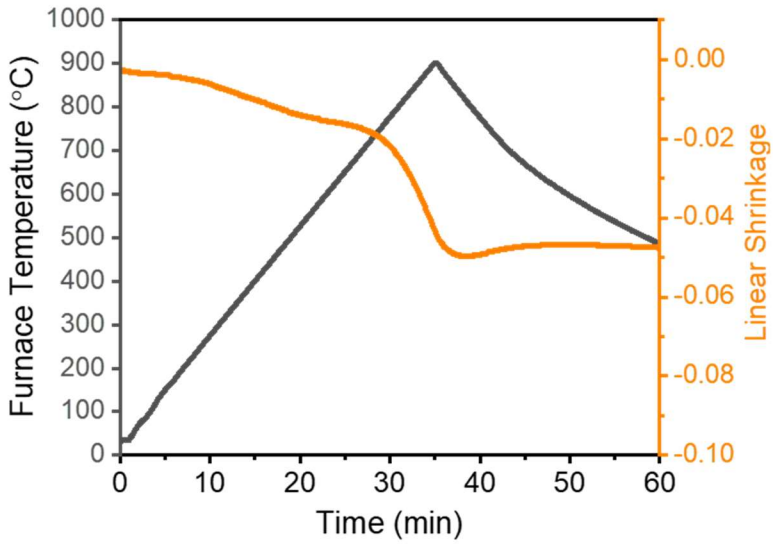

Figure 6.2 Shrinkage curve of a ZnO sample heated to 900°C without an applied field ("no-field").

It is important to note that previous flash sintering studies on ZnO utilized a much higher current density (upwards of 4 A/cm^2) to reach densities above 95% [19,22,36]. In this study, the final density of this sample (~ 85%) is much lower compared to the previous reports due to the flash sintering conditions specified. The effects of using a higher electric field is typically detrimental and undesirable because it will cause the sample to start the flash sintering process at a lower furnace temperature [219], thereby limiting its percolation path and creating hot spots throughout the sample (Figure 6.3) [124]. The current density used was also significantly lower which reduces the sample temperature [38] and consequently the final density. Although this may seem to oppose the usual goal of reaching full densities for ceramics, using this particular set of conditions resulted in the interesting phenomenon for ZnO, where the samples consistently fractured near the middle of the sample parallel to the flat surfaces.

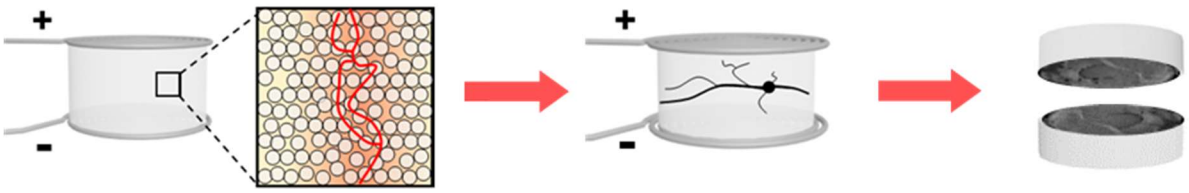

Figure 6.3 Schematic showing the formation of hot spot and sample fracture after flash sintering.

XRD spectra of the positive and negative surfaces, and fractured surfaces were performed and shown in Figure 6.4(a) and (b), respectively. All the patterns indicate single-phase wurtzite ZnO. To analyze the difference between these spectrums, the lattice parameters were calculated for all the surfaces using hexagonal lattice parameter calculation from (100) and (002) peak positions. The ratio of the lattice parameters c/a for the four surfaces are shown in Figure 6.4(c).

The positive and negative surfaces have very similar ratios of c/a, as indicated by a dashed line for reference. On the contrary, the fractured surfaces showed different ratios; the fractured surface closer to the positive side had a much lower c/a ratio while the fractured surface closer to the negative side had a slightly higher c/a ratio. Changes to the c/a ratio are correlated to the relative position of the anion sub-lattice with respect to the cation sub-lattice along the c-axis, which can be the result of point defects. Due to the fracture which occurred at a certain point during flash sintering, the separation of the sample may have led to the accumulation of contrasting defects on each side.

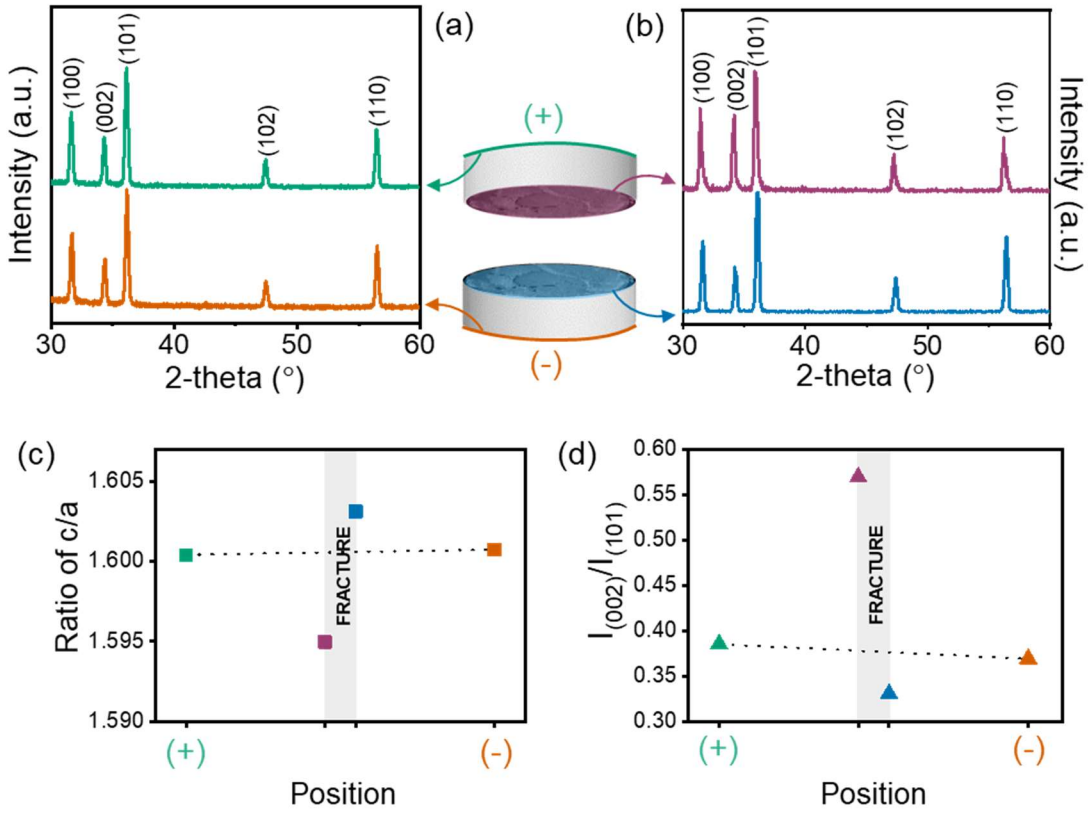

Figure 6.4 X-ray diffraction (XRD) patterns of the flash sintered ZnO sample on the (a) positive and negative surfaces, and (b) the fractured surfaces. (c) Plots of the ratio of c to a lattice parameter of each surface and (d) relative intensity of (002) to (101) peak areas.

The XRD spectra also showed differences in the relative intensity of (002) to (101) between the surfaces and thus the calculated intensity ratios ($I_{(002)}/I_{(101)}$) are shown in Figure 6.4(d). The $I_{(002)}/I_{(101)}$ for the positive and negative surfaces showed similar values, while there is a noticeable difference on the fractured surfaces. $I_{(002)}/I_{(101)}$ was found to be much higher on the positive fractured surface while the fractured side on the negative side is slightly lower. The (002) intensity in ZnO studies are well-known to be the result of c-axis growth and likely to have occurred on the positive fractured surface. It should be noted that the XRD provides the overall lattice information over a large surface area (several mm^2) and thus requires further analysis to investigate the morphology and defects characteristics.

6.3.2 Microstructure and defect analysis after flash sintering

Figure 6.5(a) shows a low magnification micrograph of the entire positive fracture surface, indicating many major cracks and a large void (~200 μm). This large void is a major hot spot, formed at the current path during flash sintering. Such currents paths are a common phenomenon during flash sintering: due to the rapid temperature increase along the initial current path at the onset of flash sintering, the conductivity along this path is much higher than the surrounding volume and therefore keeping the current in this path. As this hot spot experienced extreme local temperatures, it may be high enough to form the liquid or even gas phase. Thus volume changes would likely be the reason for the sample to experience large stresses and consequently form cracks within the sample.

Upon closer inspection of the area between the hot spot and the edge of the sample (Figure 6.5(b)), a gradient in microstructure and growth of nanostructures was observed on the fractured surface. Figure 6.5(c) shows a higher magnification of the microstructure gradient which exists

between the hot spot and the edge. Figure 6.5(c1) shows the area closest to the hot spot, where there was limited growth of short nanostructures and they were mostly found along the grain boundaries. Within the grains, there were also areas of liquid phase, which are likely to be nucleation sites for the nanostructures. Figure 6.5(c2) is an area between the hot spot and the edge of the sample. This area showed a higher density of short nanostructures than Figure 6.5(c1) and formed around grain boundaries and within the grains. Figure 6.5(c3) shows the area towards the edge of the sample and farthest from the hot spot. This area contained arrays of well-aligned and uniform nanorods.

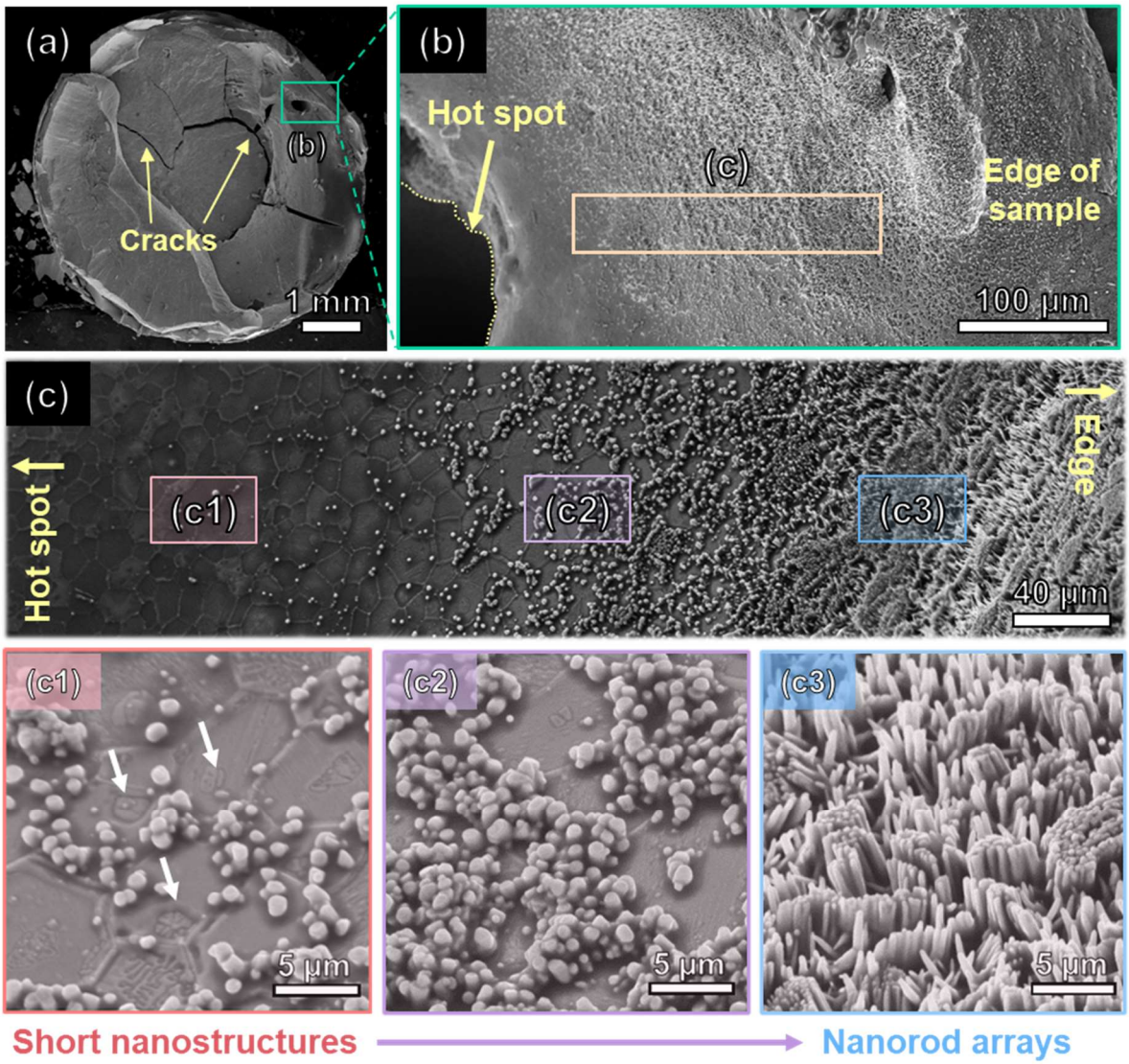

Figure 6.5 (a) Low magnification SEM image showing the formation of cracks and a large void caused by a hot spot on the positive fractured surface. (b,c) Higher magnification of the area between the hot spot and the edge of the sample showing a gradient of microstructure. (c1-c3) The gradient of microstructure consisted of short nanostructures near the hot spot and these nanostructures grew more frequently and longer towards the edge of the sample. The white arrows marked in (c1) shows liquid phases formed within the grains.

These nanostructures only exist near the hot spot of the sample towards the edge of the sample in vicinity of the current path. As a comparison to a region far away from the hot spot, Figure 6.6 shows a grain size which is only in the range of ~100 nm, which is much smaller than the grain size close to the hot spot as seen in Figure 6.5(c1), which is in the range of 2 to 10 µm.

Outside of the current path, there was probably limited current flow and much less Joule heating comparted to close to the current path, resulting in lower temperature and only slight densification and grain growth.

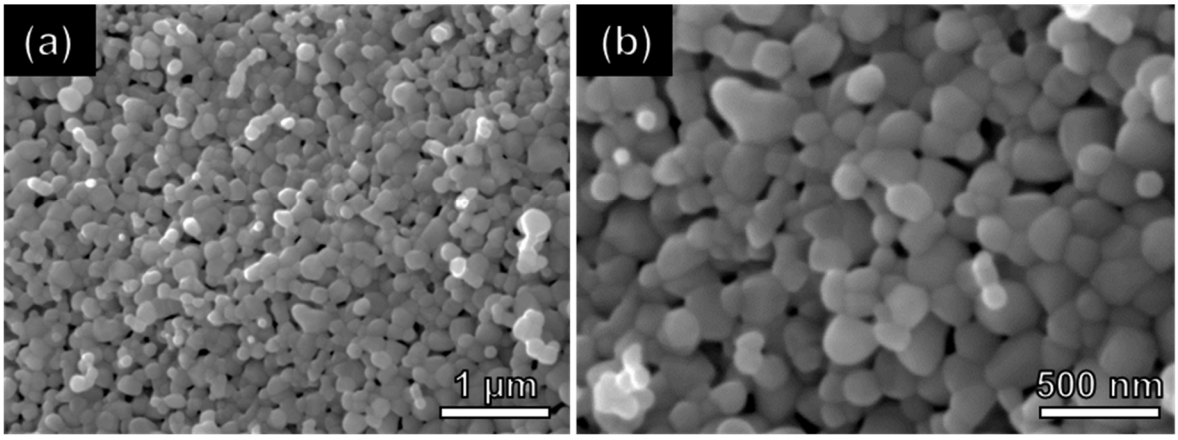

Figure 6.6 (a)-(b) SEM images of the positive fractured surface away from the hot spot region towards the middle.

Figure 6.7(a) shows the surface morphology near the hot spot for the negative fractured surface where there is also some growth of nanostructures. Higher magnification image in Figure 6.7(b) shows nanostructures growing within the grain and at the grain boundaries. This is a similar observation to the positive fractured surface. However, the nanostructures grown on the negative fractured surface appeared to grow in scattered directions and have a wider range of shapes and sizes within the same area, as shown in Figure 6.7(c). Thus, only the nanorods on the positive fractured surface was further analyzed.

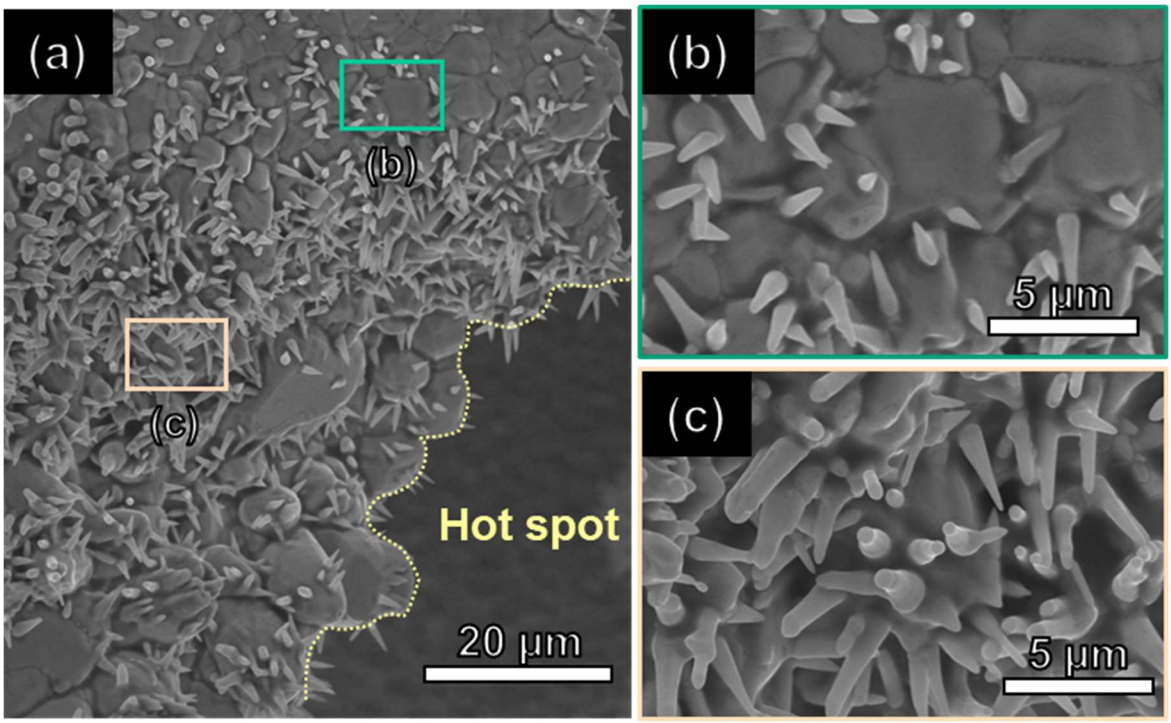

Figure 6.7 (a)-(c) SEM images of the negative fractured surface area near the hot spot showing growth of nanostructures.

To further investigate the characteristics of the nanorods grown on the positive fractured surface, Figure 6.8(a) shows a SEM image showing their overall distribution. The nanorods appear uniform in diameter and length and tend to grow in a certain pattern. Some of the areas contained dense clusters while some of the nanorods grew along a line. The clustered areas likely correspond to the growth of nanorods on a liquid phase region within the grain while the lines of nanorods were grown along the grain boundary. Figure 6.8(b) shows a TEM image of a single nanorod, where the dimensions are approximately 380 nm in diameter and 1.6 μm in height. The nanorod contained a high density of stacking faults (SF) along the growth direction of the nanorod. The SFs appear to be formed in a very periodic manner with an average spacing of 68 ± 13 nm. The selected area electron diffraction in the inset indicates that the nanorod is indeed a single crystal

and the growth axis is along c-axis, as confirmed by the high resolution TEM (HRTEM) shown in Figure 6.8(c). The HRTEM near the stacking fault region is shown in Figure 6.8(d), where the local area fast Fourier transform (FFT) contained streaks, verifying the presence of basal-plane stacking faults.

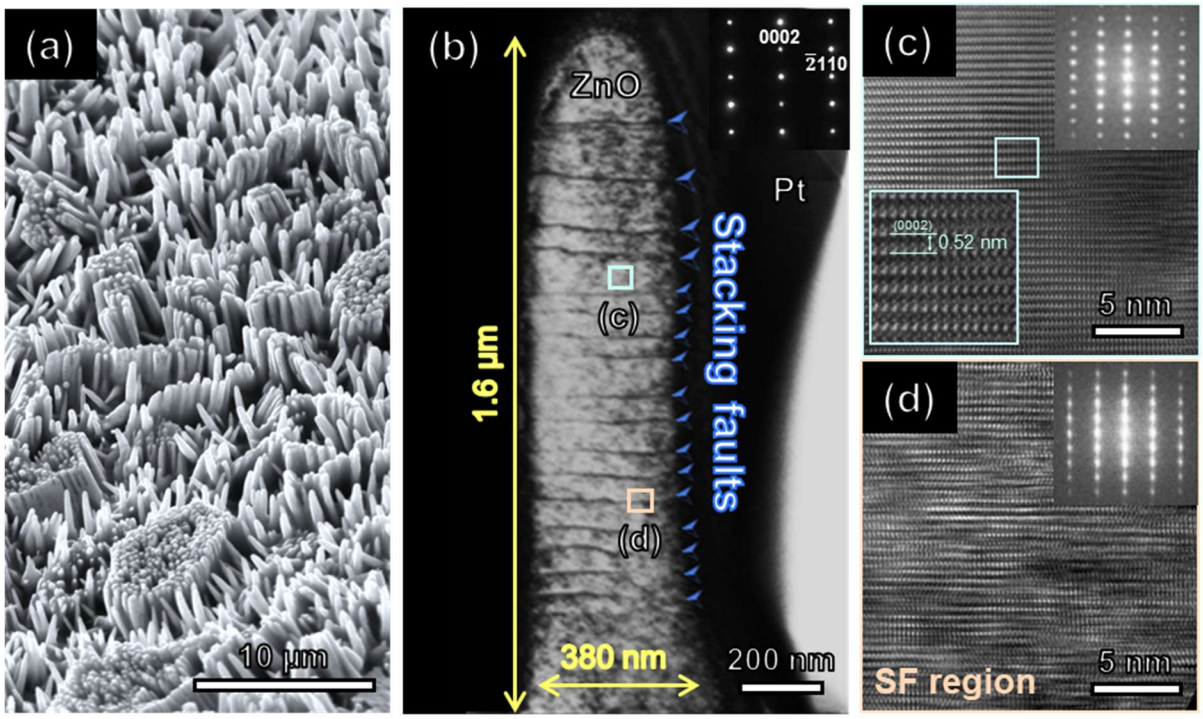

Figure 6.8 (a) SEM of the area containing a high density of nanorods showing their distribution. (b) TEM of a nanorod which contains high density stacking faults. The inset shows the selected area electron diffraction of the nanorod. (c) and (d) High resolution TEM (HRTEM) of (b), where (c) is in an area away from the stacking faults while (d) is in a stacking fault region. The HRTEM was taken from the [01-10] zone axis.

Basal-plane SFs are the most common type of stacking faults found in ZnO and the density of SFs is highly dependent on the processing method. Growth techniques which resulted in high density of SFs in ZnO are other non-equilibrium processes, such as plasma-enhanced chemical vapor deposition and rf-plasma assisted molecular beam epitaxy [220,221]. It is also possible to

produce stacking faults but in much lower density by equilibrium processes, such as metal-organic chemical vapor deposition [222]. The high density of stacking faults observed in this study is attributed to the ultrafast field-assisted growth mechanism of ZnO nanorods and the high density of point defects after flash sintering [22,191].

The defect emissions of ZnO nanostructures is a critical aspect to be used in optoelectronics and have been thoroughly studied in the literature [223]. Figure 6.9(a) shows the room temperature PL spectra for the positive and negative fractured surfaces. For both surfaces, the spectra consist of a narrow peak at 375 nm which corresponds to the ultraviolet (UV) emission or near band edge (NBE) (~3.3 eV) which is contributed from free exciton recombination. The broad peak at higher wavelengths corresponds to the deep level emissions (DLE) based on the presence of lattice defects.

As the broad peak in the DLE contained multiple peaks, the peaks were fitted using multiple Gauss distributions in Figure 6.9(b) and (c) for the positive and negative fractured surfaces, respectively. The positive fractured surface spectrum showed a green emission (565 nm) peak and large red emission (674 nm) peak. Both of these peaks are generally associated to excess oxygen interstitials, and typically seen in samples which have been annealed in air or oxygen atmospheres [224–227]. The positive fractured surface also showed a very minor violet emission peak (406 nm), which could originate from zinc interstitials [228]. On the contrary, the negative fractured surface showed strong green emissions (545 nm) with a minor orange emission (602 nm). The green emissions have been correlated with excess oxygen vacancies and observed in samples which were annealed in reduced atmospheres [224,227,228].

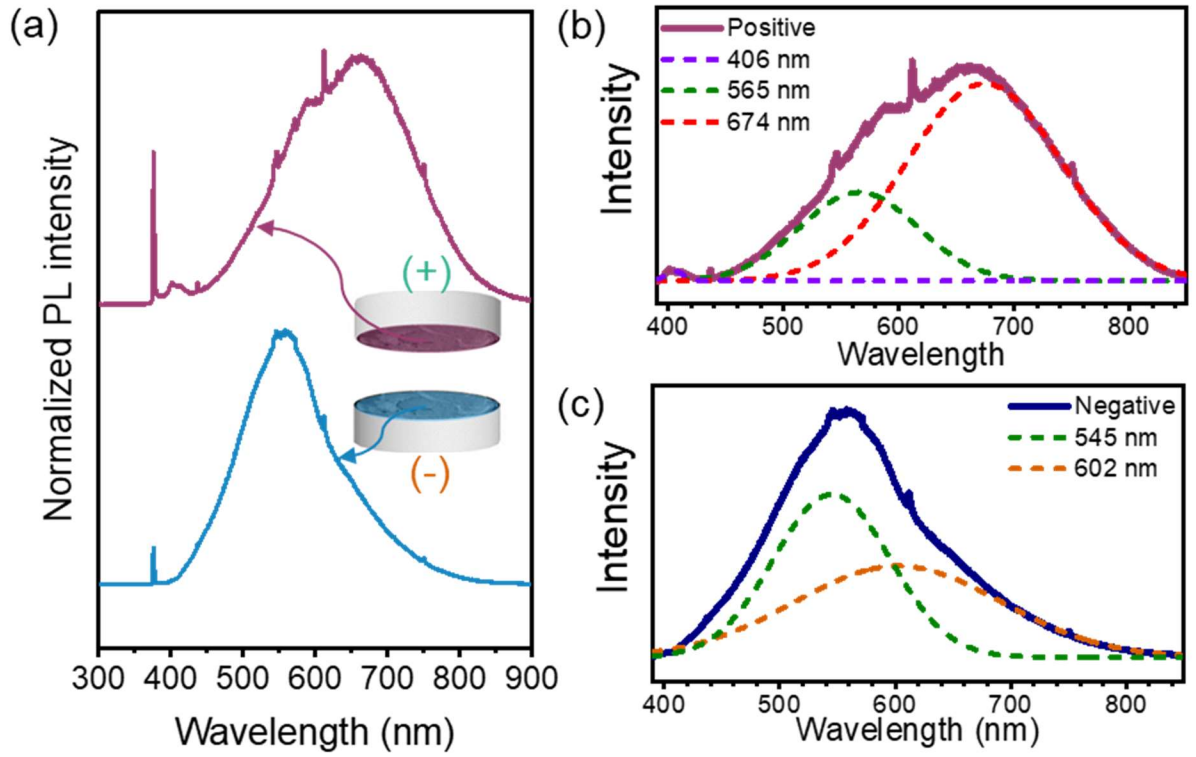

Figure 6.9 (a) Photoluminescence (PL) spectrum of the positive and negative fractured surfaces. The deep level emissions were fitted in (b) and (c) using Gaussian distributions for the positive and negative fractured surfaces respectively.

6.3.3 Growth mechanism of defective nanostructures

The literature on the growth mechanism of ZnO nanorods have been well-studied in the past two decades. In relevance to this study, the nanorods most likely grew by vapor-liquid-solid (VLS) mechanism. In order to grow by VLS mechanism, a metal catalyst (i.e. Cu or Au) is typically used to initiate the axial growth by forming a liquid-solid interface with Zn liquid and vapor [229]. This type of growth can also be self-catalyzed by forming Zn/ZnO_x liquid droplets, followed by reoxidation [230], which is most likely the case for this study since there is no involvement of external dopants.

Figure 6.10 shows the schematic of the suggested growth mechanism for the nanorods produced from this field-assisted technique. For the growth of one-dimensional nanostructures by VLS mechanism, gaseous precursors of Zn and O_2 are required. Since the current percolated through a hot spot region of the sample, extreme local temperature was achieved in this area and formed vapor products which was evident by the large void observed. It is expected that a thermal gradient exists from the hot spot region to the edge of the sample, as evidenced by the microstructure gradient. The phase diagram of Zn-O suggests that the formation of Zn/ZnO_x liquid is possible around 450 to 900°C and vapor at > 900°C in an oxygen deficient state [231]. Hence, it is more likely that liquid phase regions could form farther away from the hot spot region, and these liquid phase regions act as the nucleation sites for the nanorods to grow from. With larger liquid phase regions formed closer to the edge, this resulted in higher density arrays of nanorods observed in Figure 6.5(c3).

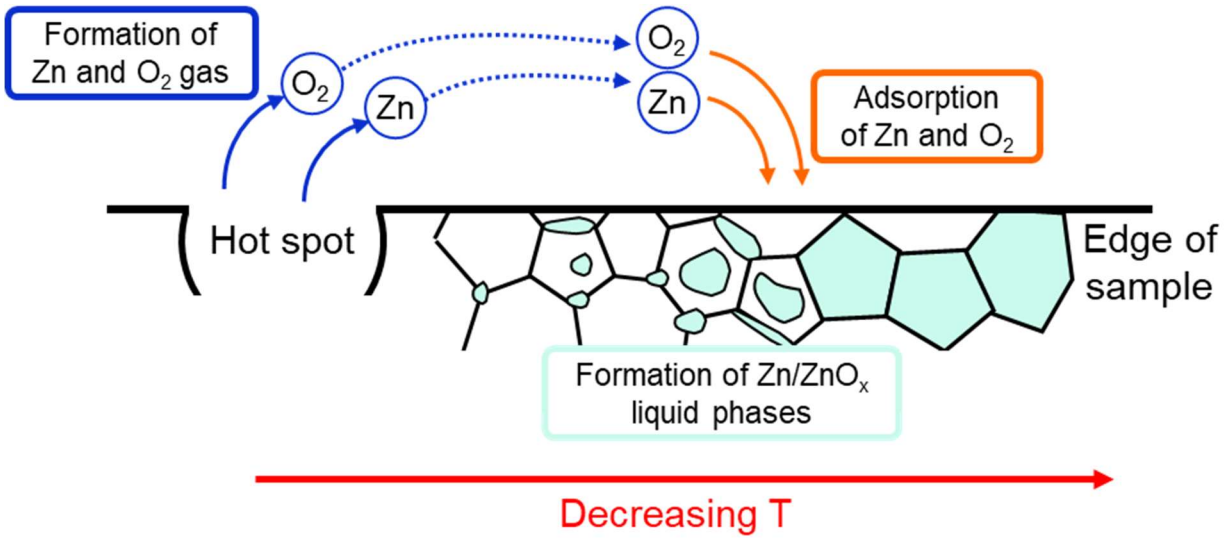

Figure 6.10 Schematic of field-assisted growth mechanism of ZnO nanorods.

Growth of ZnO structures produced by flash sintering was first evident in a study by Zhang *et al.*[20], where large rods with diameter of > 5 μm grew at the cracks approximately in the middle of the sample. Our study shows that by simply altering the flash sintering conditions, high density of ZnO nanostructures can be grown. As the previous study utilized a much higher current density (15.4 A/cm^2) [20], the estimated sample temperature should be significantly higher based on a previous temperature estimation study [38]. This increase in sample temperature could impact the growth mechanism involved and resulted in the large rods observed. Additional investigation is needed to fully understand how the growth mechanism and final morphology of the ZnO nanostructures change under other flash sintering conditions.

This demonstration suggests that the field-assisted technique offers the unique capability of forming highly defective 1D nanostructures. Flash sintering has been shown to form a variety of defects in bulk ceramics, which are not typically found in conventional sintering techniques [22,56,121]. In most ceramics, these defects are caused by the accumulation of oxygen vacancies and shows evidence of oxygen deficiency, such as sample blackening [54,100]. In this study, the presence of point defects assisted the reduction of ZnO to Zn/ZnO_x liquid phases and Zn gas vapor under low temperatures. This has also led to contrasting photoluminescence emissions on the fractured surfaces and nanostructures containing high density of stacking faults. This shows tremendous potential for this field-assisted technique to grow nanostructures containing high density of defects that do not exist in the nanostructures processed using equilibrium processes.

6.4 Conclusions

This study demonstrates the feasibility of growing ZnO 1D nanostructures containing high density of defects using a non-equilibrium field-assisted growth technique. This technique can

produce extreme local temperatures and high concentrations of point defects, which led to the growth of nanostructures on fractured surfaces. These ZnO nanostructures grew by a self-catalyzed VLS mechanism and had contrasting characteristics on each fractured surface. The positive fractured surface contained well-aligned ZnO nanorods which were uniform in shape and size, and contained high density of stacking faults. Room temperature photoluminescence showed a strong excitonic UV emission with a red emission for the surface containing nanorods. On the contrary, the negative fractured surface contained more scattered nanostructures with variant shapes and sizes, and exhibited weak UV emission and strong green emission. This technique demonstrates a possible method to introduce defects into 1D nanostructures and could potentially be implemented for other ceramic systems if it experiences a similar VLS-based growth at elevated temperatures.

CHAPTER 7. FORMATION OF LIQUID PHASE AND NANOSTRUCTURES IN FLASH SINTERED ZnO

This chapter contains text and figures published in a journal article titled "Formation of liquid phase and nanostructures in flash sintered ZnO" by X.L. Phuah, W. Rheinheimer, Akriti, L. Dou & H. Wang, Scripta Mat, 2021, 195, Pages 113719. The original article has been modified to include information from the supplemental information of the published article.

The authors would like to acknowledge the support from the U.S. Office of Naval Research (Contract number: N00014-17-1-2087 for sintering effort and N00014-20-1-2043 for TEM). W.Rheinheimer thanks the German Research Foundation for support under grant no. HO 1165/20-1 within the priority programme SPP1959 and grant no. Rh 146/1-1 within the Emmy Noether programme. Akriti acknowledges support from the Frederick N. Andrews Fellowship. L. Dou acknowledges support from Davidson School of Chemical Engineering of Purdue University.

7.1 Introduction

Flash sintering was first reported a decade ago and has gained significant attention due to its unique capability of densifying ceramics within a few seconds [16]. This technique is performed by applying an electric field to a green body during the heating process. At a certain combination of furnace temperature and electric field, the sample starts to be conductive enough and begins to flow current. This causes the sample to experience Joule heating and a thermal runaway, which rapidly increases the sample temperature over the furnace temperature. The non-equilibrium characteristics of this phenomenon has resulted in many unique features, such as a generation of high density of defects and metastable phases [22,56,121,157,232].

In a recent study, flash sintering of ZnO performed with high electric field and low current density has shown a unique capability of forming nanostructures [29]. ZnO nanostructure growth commonly occurs by the vapor-liquid-solid mechanism, which requires the presence of a liquid phase as nucleation sites. However, the formation of liquid phase in ZnO has only been observed in systems containing metallic oxide additives, where the additive has a low melting temperature

such as Bi_2O_3 (T_m~875°C) [20,233]. In this study, microstructural evidence of the formation of liquid phases and nanostructures in flash sintered ZnO is presented under various current density conditions, and correlated with the photoluminescence characteristics. The formation mechanisms of such liquid phases and nanostructures are discussed.

7.2 Experimental methods

Commercial ZnO nanopowder (US Research Nanomaterials Inc, 99.95% purity) with an average particle size of 18 nm was pressed into cylindrical green bodies (diameter of 6 mm, thickness of 3 mm, green density of ~60%). Flash sintering was performed in a horizontal push-rod dilatometer (TA Instruments DIL 801), where the green body was placed between two Pt coils as contact which were connected to a DC power supply (Sorensen DLM 300-2). While the furnace was heating to 900°C at 25°C/min, an electric field of 600 V/cm was applied across the sample. The power supply automatically switches from voltage to current control when the current density reaches the preset limit during heating. In this study, three samples with a current density limit of 1, 2 and 3 A/cm^2 were compared. The steady state current was held for 60 seconds before turning off the power supply. The furnace was cooled at 25°C/min after reaching the furnace temperature of 900°C. The microstructure of the fractured surface was characterized by a Quanta 650 FEG scanning electron microscope (SEM). Photoluminescence (PL) was performed at room temperature using a Coherent OBIS laser with a wavelength of 375 nm and collected by a SpectraPro HRS-300 spectrometer.

7.3 Results and discussion

The furnace temperature and linear shrinkage measured by the dilatometer are shown in Figure 7.1(a) during the entire heating process. At approximately 750°C, both abrupt current flow

and shrinkage were observed for all samples. The sample experienced more total shrinkage with higher current densities due to the higher expected sample temperature caused by the higher power dissipation. Figure 7.1(b) shows the electric field and current density curves between 29 and 31 minutes of the heating process. When the power supply is turned off after the holding time, a drop of sample temperature and a slight dip in the linear shrinkage curves is evident in Figure 7.1(a).

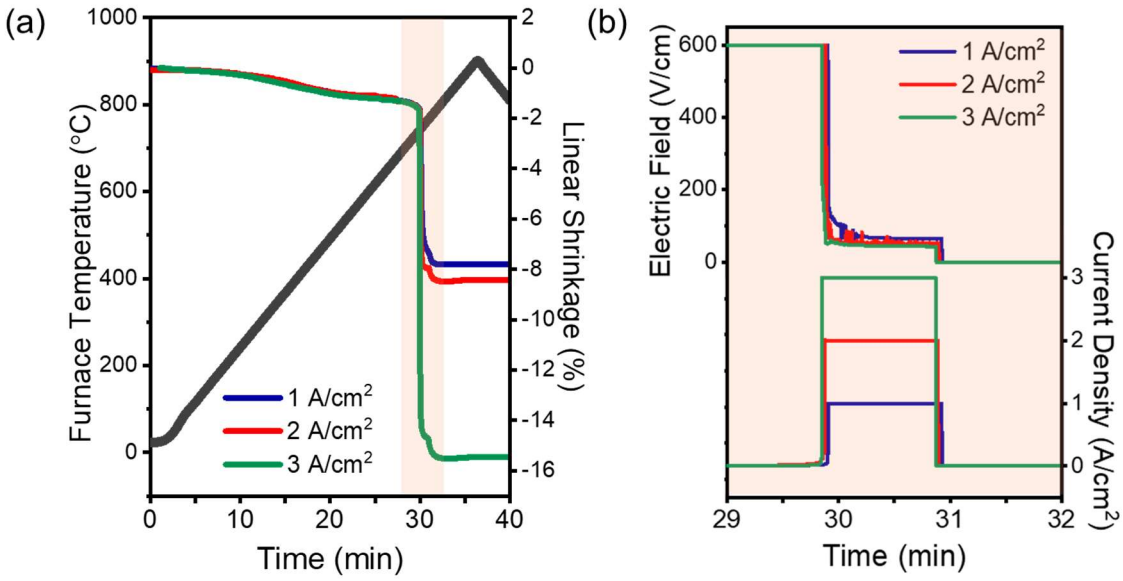

Figure 7.1 (a) Furnace temperature and linear shrinkage measured by the dilatometer during flash sintering with current density limits of 1, 2 and 3 A/cm^2. (b) Electric field and current density curves between 29 and 31 minutes, where the power supply switches from voltage to current control.

In previous flash sintering studies of ZnO, the minimum current density required to reach high relative densities (> 95%) is at least 4 A/cm^2 [20,22,36]. Instead, by using a combination of very high electric field and low current densities, very fast shrinkage occurred, along with fracture approximately midway through the sample and parallel to the electrodes (Figure 7.2(a)). A previous study showed a large void and the growth of nanostructures in the vicinity of the void on

the positive fractured surface [29]. Thus, in this study, only the positive fractured surface was further investigated for each current density.

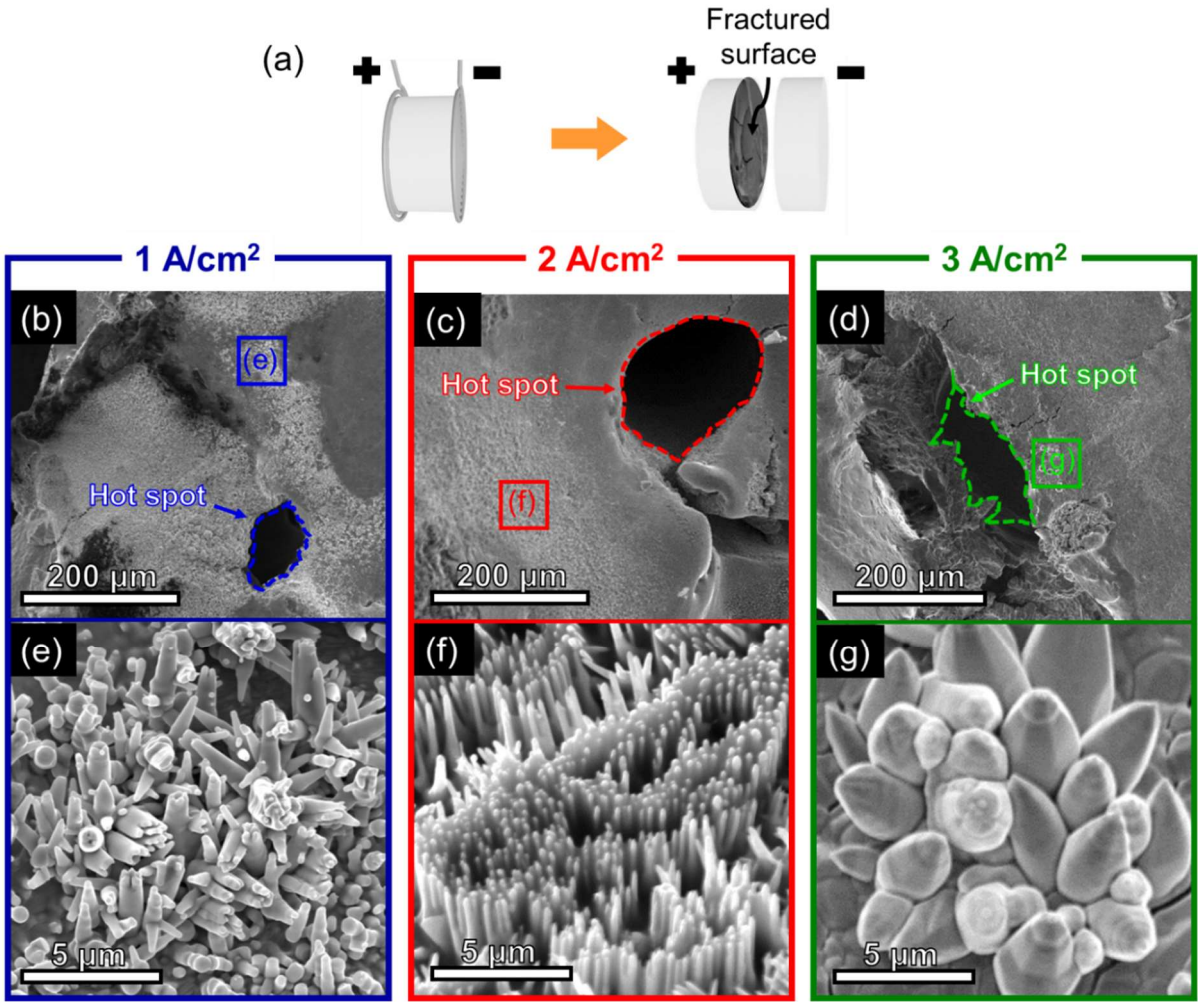

Figure 7.2 (a) Schematic of sample fracture low magnification SEM of samples with current density (b) 1 A/cm2, (c) 2 A/cm^2 and (d) 3 A/cm^2, showing the overall morphology of fractured surface (positive) containing large void. (c) Higher magnification of the area marked by the box in (b) showing the various morphology of nano- and microstructure formed.

Figure 7.2(b)-(d) show low magnification SEM images of the positive fractured surfaces of samples with current density of 1, 2 and 3 A/cm^2, respectively. In each of the images, a large void with a diameter of several hundred microns was observed, which is the result of a hotspot as discussed later. Figure 7.2(e)-(g) show the areas near the void, where the growth of nano- and microstructures were observed. These structures had different morphology at each current density. For the sample with a current density limit of 1 A/cm^2, the nanostructures resembled tetrapods, while using a current density limit of 2 A/cm^2 formed well-aligned nanorods. On the contrary, current density limit of 3 A/cm^2 results only in the growth of large rods with diameters of 3 to 5 μm containing hexagonal facets and tapered pyramidal ends. This contrasting observation suggests different growth mechanisms occurring between the low (1 and 2 A/cm^2) and high current densities (3 A/cm^2).

The low current density samples containing nanostructures were further analyzed to investigate the growth mechanism. Figure 7.3(a) shows a gradient of microstructure between the nanostructures region and the hot spot. This image revealed that the nanostructures grew on very large grains (~3 to 10 μm) and mostly around the grain boundaries. In some areas, the nanostructure also grew within the grains but less frequently. Upon closer inspection of the large grains without nanostructures, liquid phase regions were observed, as shown in Figure 7.3(b) and (c) for samples with current density limits of 1 A/cm^2 and 2 A/cm^2, respectively.

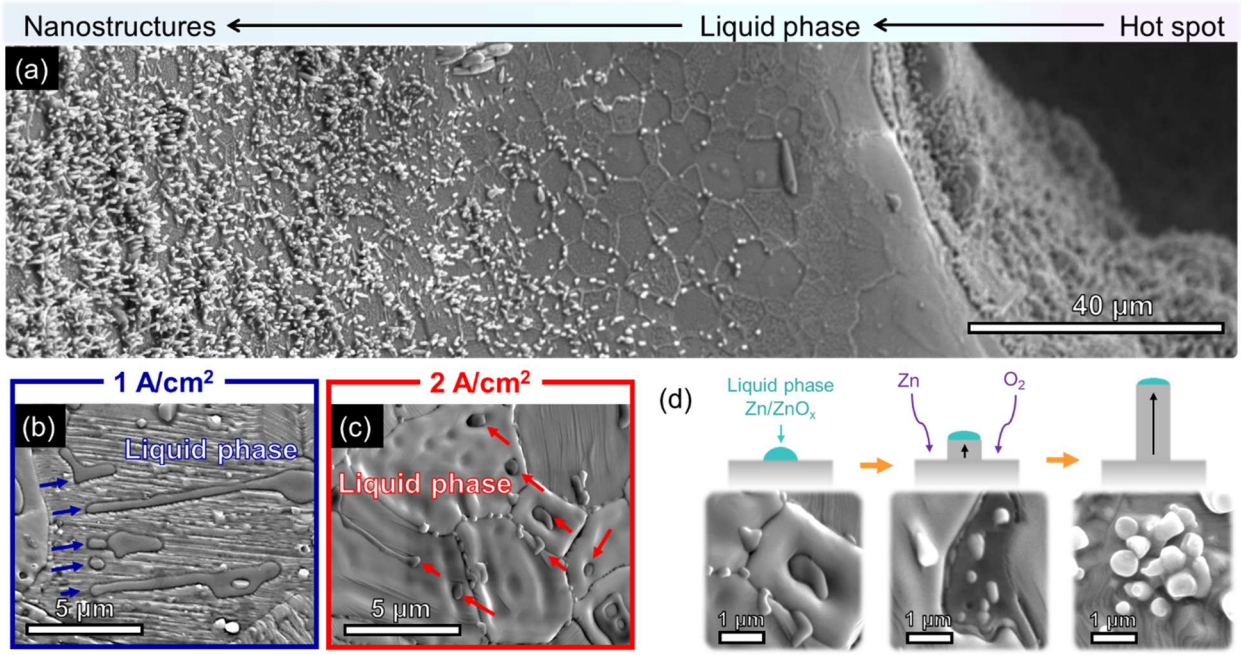

Figure 7.3 (a) SEM showing the gradient in microstructure which exist between the nanostructures and the hot spot areas for the 2 A/cm^2 sample. The grains with less growth of nanostructures showed liquid phase present in the grains and at the grain boundaries for both (b) 1 A/cm^2 and (c) 2 A/cm^2 samples. (d) Schematic of the vapor-liquid-solid mechanism.

Growth mechanisms of ZnO nanostructures have been explained by vapor-liquid solid (VLS) or vapor-solid (VS) mechanisms. Although the mechanism is difficult to distinguish and it is possible for both mechanisms to occur in the present case, the direct microstructural evidence of liquid phase shown in the lower current density samples points towards the VLS mechanism. The VLS mechanism is usually associated with the use of a metal catalyst, where the Zn vapor forms a liquid alloy with metal on the substrate and the supersaturation of the liquid will lead to axial growth by precipitation [234]. This can also occur without the use of a catalyst, but would first require the nucleation of Zn/ZnO$_x$ liquid phase [235,236]. In our study, liquid phases observed in Figure 7.3(b) and (c) are likely to act as the self-catalyst sites for the growth of nanostructures in the low current density samples, as sketched in Figure 7.3(d).

The nanostructures observed for the lower current density samples are different, as shown in Figure 7.2(e) and (f). It is most likely that their contrasting morphology is due to local fluctuations in temperature and oxygen partial pressure between the samples. The 1 A/cm^2 sample formed a complex tetrapod-like crystal, which can be grown in similar conditions for nanorods or nanowires [237]. The preference for growing in a tetrapod structure is related to the structure of the core [238], which is still currently under investigation. The nanostructures in 2 A/cm^2 also appear to have smaller dimensions, which are likely due to the high areal density of nanostructure of growth [230].

In contrast, the VS mechanism occurs by direct absorption of gas phase onto the solid surface and is likely experienced by the sample with higher current density. Low magnification SEM of the 3 A/cm^2 sample shown in Figure 7.4 did not exhibit any liquid phase and the growth of microstructures occurred very scarcely. VS typically occurs at a much slower rate as the nucleation conditions are less favorable without the liquid phase [239]. Additionally, structures produced by the VS mechanism has shown more inhomogeneity. This can be attributed to local thermal fluctuations at the growth front and mobility differences of atoms absorbed on various planes [240,241].

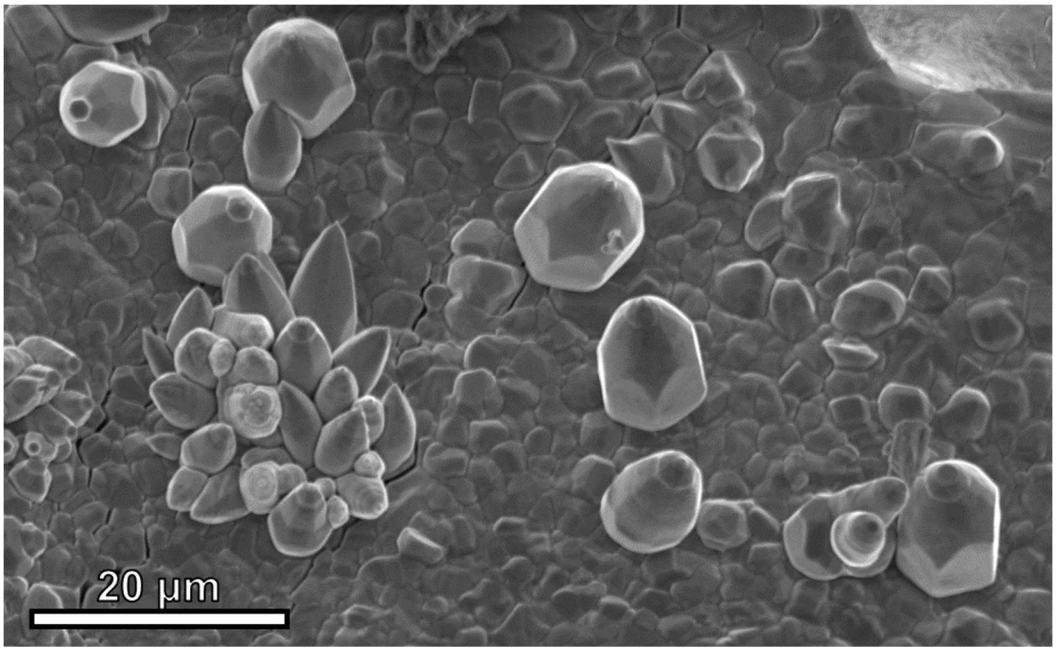

Figure 7.4 Low magnification SEM showing the distribution of microstructure growth for the sample with current density limit of 3 A/cm^2.

To understand the occurrence of nanostructures during flash sintering, first the formation of the crack needs to be addressed. As shown in Figure 7.2, cracking is associated with the formation of a hot spot. The hot spot is the result of having a preferred current percolation pathway which causes local overheating. This phenomenon is typically observed in large cross-sectional samples and extreme flash conditions such as high electric fields and current densities [242] The formation of a large void as evident in Figure 7.2 would also suggest that thermodynamic conditions resulted in the formation of liquid or gas phase of ZnO, i.e., the ZnO was driven off-stoichiometric and/or the temperature increased to above 2000°C [231]. Due to volume changes arising from phase transformations, the formation of cracks and sample fracture are likely to occur. While the reason for the cracking remains unclear, it seems clear that it occurred in the beginning of flash sintering, when strong temperature gradients and high temperatures develop as

nanostructures could not have formed otherwise. Note that the cracking event is not visible in the densification curves in Figure 7.1(a).

Within the crack, the thermodynamic conditions were such that nanorods formed [29]. As nanostructures in ZnO are usually associated with point defects, the point defect concentrations were analyzed at the positive fractured surface of all three samples by room temperature photoluminescence (PL) as shown in Figure 7.5(a). Typical PL spectra for ZnO consist of a UV or near band-edge (NBE) peak and one or several broad emission peaks in the visible range from deep level emissions (DLE) [243]. The peak at 375 nm corresponds to the UV emission, which is based on free exciton emission, while the broad overlapping peaks above 375 nm correspond to visible emissions from point defects. The ratio of UV to visible emission showed a decreasing trend with increasing current densities, as a higher current density results in a higher point defect concentration.

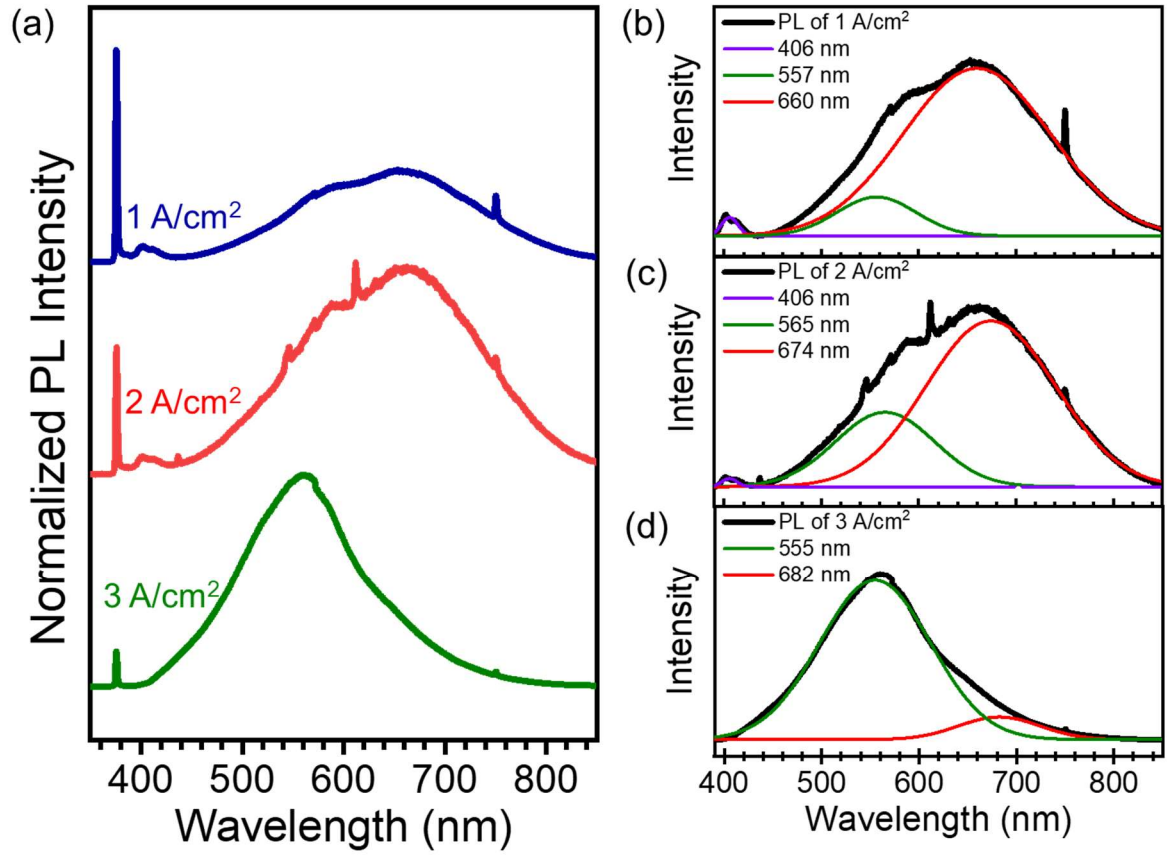

Figure 7.5 (a) Room temperature photoluminescence (PL) spectra measured on the positive fractured surface for 1, 2 and 3 A/cm^2. Deconvolution of the visible emission is shown for (b) 1 A/cm^2, (c) 2 A/cm^2 and (d) 3 A/cm^2.

To investigate the origin of DLE peaks, deconvolution of the visible region was performed for all three samples in Figure 7.5(b)-(d) using Gaussian fitting. Three peaks are identified at about 406 nm, 560 nm and 670 nm corresponding to V'_{Zn}, V_O° and O'_i, respectively [244,245]. While the position of these three peaks changes slightly with varying current limits, the relative intensities change strongly. The peak at 410 nm (V'_{Zn}) disappears completely at 3 A/cm². The peak at 650nm (O'_i) decreases as well with increasing current limit, but the peak at 550 nm (V_O°) increases significantly. Accordingly, the PL spectra indicate the following effects with increasing current

limit: an overall increasing surface defect concentration, a relative decrease of $[V'_{Zn}]$ and $[O'_i]$ and a relative increase of $[V_O^{\circ}]$. These changes agree well with a reduction of the surface [244] and with the occurrence of a liquid phase as observed in Fig. 3 that only exists between 692K and 1179K in reducing conditions [231].

Based on these defect characteristics, it is likely that a surface reduction of the positive crack surface occurred during flash sintering either by electromigration or by nucleation of point defects. Electromigration [69,155,246] and a reduction [47,54,247] are well-known for flash sintering and seems the most likely source. The electric field in the sample could migrate oxygen vacancies away from the positive electrode (i.e. towards the positive side of the crack). Zn vacancies could migrate towards the negative electrode (i.e. away from the positive side of the crack).

7.4 Conclusions

In summary, flash sintering of ZnO under various current densities were investigated. All samples experienced a hot spot with a large void and fracture which occurred parallel to the electrodes as a result from the volume changes from phase transformations to gas and/or liquid phase(s). Samples with current densities 1 and 2 A/cm^2 resulted in a field assisted growth of nanostructures in the vicinity of the hot spot. The growth occurred by the VLS mechanism due to the observation of liquid phases forming within the grains and at the grain boundaries. Increasing the current density to 3 A/cm^2 results in no liquid phase formation. Instead the inhomogeneous microstructures were formed by the VS mechanism. The PL emission indicates an overall increase of point defects with increasing current density, a relative decrease of $[V'_{Zn}]$ and $[O'_i]$ and a relative increase of $[V_O^{\circ}]$ indicating a reduction of the positive side of the crack during flash sintering. This

reduction is likely to be caused by electromigration. This work documents the impacts of electric fields and currents during flash sintering on the stoichiometry of ZnO. The results offer new pathways to design non-stoichiometric materials with new functionalities, and field-assisted growth of nanostructures in ZnO.

CHAPTER 8. SUMMARY AND FUTURE OUTLOOKS

Overall, this dissertation presents detailed work on flash sintering of ZnO and its growth of nanostructures. Flash sintering is an important advanced ceramic processing technique due its significant reduction in energy and time compared to conventional sintering. It is also capable of introducing non-equilibrium defects due to the ultra-high heating rates, and impact of electric field and current. The detailed work in this dissertation studying the microstructure and defects in flash sintered ZnO will allow tailored defects density and grain sizes to be achieved for a wide range of applications. In addition, the growth of ZnO nanostructures through flash sintering presents a new and exciting direction for flash sintering applications. The major findings are summarized below:

1. A controlled current ramp can be used to linearly increase the current during Stage II. This parameter acts as similarly to heating rate and can be used to slow down the ultra-fast heating rate during flash sintering for a more controlled densification process. While other flash sintered ceramic systems have shown evidence of extended defects, this study showed the first evidence of stacking faults in ZnO system.
2. The type of current, whether DC or AC, can significantly impact both the microstructure and defects in flash sintered ZnO. DC flash sintering resulted in gradient microstructure and defect redistribution, while AC flash sintering was mostly homogeneous and had similar defects characteristics compared to conventionally sintered sample.
3. The growth of 1D ZnO nanostructures through flash sintering was demonstrated. By applying a high electric field and limiting a low current, ZnO nanostructures

grew near the hot spot through the vapor-liquid-solid mechanism. These nanostructures are unique compared to other equilibrium technique since they contained high density of basal-plane stacking faults and exhibited ultraviolet excitonic emission with yellow-red emission at room temperature.

4. The growth mechanism of ZnO nanostructures during flash sintering was investigated by varying the current densities. Formation of liquid phase and nanostructures were observed only at low current densities, but not at high current densities. The change in current densities impacted the resulting structure morphology and also the point defects concentrations.

For future systematic flash sintering studies, employment of various *in situ* characterization techniques could be helpful in revealing detailed information of the temperature and defect profile of the ZnO systems. *In situ* techniques with ultra-fast temporal resolution will be important to help investigation during the transient stage (Stage II) of flash sintering. Direct observation through *in situ* TEM to investigate the impact of external fields, such as simultaneous heating and biasing, would also help to elucidate further details on the defect formation and propagation.

While the ZnO studies in this dissertation focus on optical properties, there are other properties which could be enhanced from the presence of extended defects for future opportunities. As shown in the recent work by Cho *et al.*, the mechanical properties of flash sintered ZnO was investigated and showed a higher flow stress compared to conventionally sintered ZnO. Improvement in ceramic deformability was also observed in other flash sintered ceramics, including 3YSZ [146] and TiO_2 [57]. Ceramics are known to be extremely hard and brittle due to their rigid bonds and limited dislocation mobility at room temperature, but this can potentially be overcome by high density defects introduced by flash sintering [150]. It will also be important for

further investigation of properties for other flash sintered ceramic systems where defects could play a significant role.

Another important future direction for flash sintering is the upscaling of the process and modifications for complex shape materials. Recent efforts have been made into modifying the static single sample process into a dynamic continuous process [110] and contactless process [111,248,249]. Flash sintering also brings additional engineering questions to the possibility of processing complex shape samples due to the electrode configuration and current pathway. Several studies have shown the adaptations to various geometries such as thick and thin films [49,250], and most recently gear-shaped samples [106]. These demonstrations show great potential for combination of the flash sintering process with other techniques and open new avenues for the applications of flash sintering.

REFERENCES

[1] S.-J.L. Kang, Sintering: densification, grain growth and microstructure, Butterworth-Heinemann, 2004.

[2] K. Lu, Sintering of nanoceramics, Int. Mater. Rev. 53 (2008) 21–38. doi:10.1179/174328008X254358.

[3] M.N. Rahaman, Ceramic Processing and Sintering, CRC Press, 2007. doi:10.1201/9781315274126.

[4] R.J. Brook, Fabrication Principles for the Production of Ceramics With Superior Mechanical Properties., Proc. Br. Ceram. Soc. 32 (1982) 7–24. https://pascal-francis.inist.fr/vibad/index.php?action=getRecordDetail&idt=PASCAL8130524431.

[5] D.-J. Chen, M.J. Mayo, Rapid Rate Sintering of Nanocrystalline ZrO2-3 mol% Y2O3, J. Am. Ceram. Soc. 79 (1996) 906–912. doi:10.1111/j.1151-2916.1996.tb08524.x.

[6] B.C. Kim, J.H. Lee, J.J. Kim, T. Ikegami, Rapid rate sintering of nanocrystalline indium tin oxide ceramics: Particle size effect, Mater. Lett. 52 (2002) 114–119. doi:10.1016/S0167-577X(01)00377-9.

[7] I.-W. Chen, X.-H. Wang, I.-W. Chen, X.-H. Wang, Sintering dense nanocrystalline ceramics without final-stage grain growth, Nature. 404 (2000) 168–171. doi:10.1038/35004548.

[8] M. Biesuz, S. Grasso, V.M. Sglavo, What's new in ceramics sintering? A short report on the latest trends and future prospects, Curr. Opin. Solid State Mater. Sci. 24 (2020) 100868. doi:10.1016/j.cossms.2020.100868.

[9] N. Kuramoto, H. Taniguchi, Transparent AIN ceramics, J. Mater. Sci. Lett. 3 (1984) 471–474. doi:10.1007/BF00720974.

[10] Y. Li, Y. Liu, V. V. Fedorov, S.B. Mirov, Y. Wu, Hot-pressed chromium doped zinc sulfide infrared transparent ceramics, Scr. Mater. 125 (2016) 15–18. doi:10.1016/j.scriptamat.2016.07.027.

[11] J. Wang, J. Ma, J. Zhang, P. Liu, D. Luo, D. Yin, D. Tang, L.B. Kong, Yb:Y 2 O 3 transparent ceramics processed with hot isostatic pressing, Opt. Mater. (Amst). 71 (2017) 117–120. doi:10.1016/j.optmat.2016.04.029.

[12] I. Tanaka, G. Pezzotti, T. Okamoto, Y. Miyamoto, M. Koizumi, Hot Isostatic Press Sintering and Properties of Silicon Nitride without Additives, J. Am. Ceram. Soc. 72 (1989) 1656–1660. doi:10.1111/j.1151-2916.1989.tb06298.x.

[13] R.A. Alliegro, L.B. Coffin, J.R. Tinklepaugh, Pressure-Sintered Silicon Carbide, J. Am. Ceram. Soc. 39 (1956) 386–389. doi:10.1111/j.1151-2916.1956.tb15609.x.

[14] Z.A. Munir, U. Anselmi-Tamburini, M. Ohyanagi, The effect of electric field and pressure on the synthesis and consolidation of materials: A review of the spark plasma sintering method, J. Mater. Sci. 41 (2006) 763–777. doi:10.1007/s10853-006-6555-2.

[15] S. Ghosh, A.H. Chokshi, P. Lee, R. Raj, A Huge Effect of Weak dc Electrical Fields on Grain Growth in Zirconia, J. Am. Ceram. Soc. 92 (2009) 1856–1859. doi:10.1111/j.1551-2916.2009.03102.x.

[16] M. Cologna, B. Rashkova, R. Raj, Flash Sintering of Nanograin Zirconia in <5 s at 850°C, J. Am. Ceram. Soc. 93 (2010) 3556–3559. doi:10.1111/j.1551-2916.2010.04089.x.

[17] M. Trunec, K. Maca, Compaction and Pressureless Sintering of Zirconia Nanoparticles, J. Am. Ceram. Soc. 90 (2007) 2735–2740. doi:10.1111/j.1551-2916.2007.01781.x.

[18] R.I. Todd, E. Zapata-Solvas, R.S. Bonilla, T. Sneddon, P.R. Wilshaw, Electrical characteristics of flash sintering: Thermal runaway of Joule heating, J. Eur. Ceram. Soc. 35 (2015) 1865–1877. doi:10.1016/j.jeurceramsoc.2014.12.022.

[19] C. Schmerbauch, J. Gonzalez-Julian, R. Röder, C. Ronning, O. Guillon, Flash sintering of nanocrystalline zinc oxide and its influence on microstructure and defect formation, J. Am. Ceram. Soc. 97 (2014) 1728–1735. doi:10.1111/jace.12972.

[20] Y. Zhang, J.-I. Jung, J. Luo, Thermal runaway, flash sintering and asymmetrical microstructural development of ZnO and ZnO–Bi2O3 under direct currents, Acta Mater. 94 (2015) 87–100. doi:10.1016/j.actamat.2015.04.018.

[21] X. Wang, Y. Zhu, R. Huang, H. Mei, Z. Jia, Flash sintering of ZnO ceramics at 50 °C under an AC field, Ceram. Int. 45 (2019) 24909–24913. doi:10.1016/j.ceramint.2019.08.142.

[22] X.L. Phuah, H.H. Wang, H. Charalambous, S.K. Jha, T. Tsakalakos, X. Zhang, H.H. Wang, Comparison of the grain growth behavior and defect structures of flash sintered ZnO with and without controlled current ramp, Scr. Mater. 162 (2019) 251–255. doi:10.1016/j.scriptamat.2018.11.009.

[23] Y. Zhang, J. Nie, J. Luo, Flash sintering activated by bulk phase and grain boundary complexion transformations, Acta Mater. 181 (2019) 544–554. doi:10.1016/j.actamat.2019.10.009.

[24] H. Bicer, B. Beyoglu, T.E. Ozdemir, J. Okasinski, T. Tsakalakos, Direct in situ observation of electric field assisted densification of ZnO by energy dispersive X-ray diffraction, Ceram. Int. 45 (2019) 7614–7618. doi:10.1016/j.ceramint.2019.01.057.

[25] J. Liu, X. Li, X. Wang, R. Huang, Z. Jia, Alternating current field flash sintering 99% relative density ZnO ceramics at room temperature, Scr. Mater. 176 (2020) 28–31. doi:10.1016/j.scriptamat.2019.09.026.

[26] J. Cho, X.L. Phuah, J. Li, Z. Shang, H. Wang, H. Charalambous, T. Tsakalakos, A.K. Mukherjee, H. Wang, X. Zhang, Temperature effect on mechanical response of flash-sintered ZnO by in-situ compression tests, Acta Mater. 200 (2020) 699–709. doi:10.1016/j.actamat.2020.09.029.

[27] Y. Mei, S. Pandey, W. Long, J. Liu, S. Zhong, L. Zhang, S. Du, D. Xu, Processing and characterizations of flash sintered ZnO-Bi2O3-MnO2 varistor ceramics under different electric fields, J. Eur. Ceram. Soc. 40 (2020) 1330–1337. doi:10.1016/j.jeurceramsoc.2019.11.013.

[28] B. Cui, J. Niu, P. Peng, L. Shi, S. Du, J. Liu, D. Xu, Flash sintering preparation and electrical properties of ZnO–Bi2O3-M (M = Cr2O3, MnO2 or Co2O3) varistor ceramics, Ceram. Int. 46 (2020) 14913–14918. doi:10.1016/j.ceramint.2020.03.018.

[29] X.L. Phuah, J. Cho, Akriti, L. Dou, W. Rheinheimer, R.E. García, X. Zhang, H. Wang, Field-assisted growth of one-dimensional ZnO nanostructures with high defect density, Nanotechnology. 32 (2021) 095603. doi:10.1088/1361-6528/abcb2f.

[30] X.L. Phuah, W. Rheinheimer, Akriti, L. Dou, H. Wang, Formation of liquid phase and nanostructures in flash sintered ZnO, Scr. Mater. 195 (2021) 113719. doi:10.1016/j.scriptamat.2020.113719.

[31] Y. Zhang, J. Luo, Promoting the flash sintering of ZnO in reduced atmospheres to achieve nearly full densities at furnace temperatures of <120 °C, Scr. Mater. 106 (2015) 26–29. doi:10.1016/j.scriptamat.2015.04.027.

[32] A.G. Storion, J.A. Ferreira, S.C. Maestrelli, E. Maria de Jesus Agnolon Pallone, Influence of the forming method on flash sintering of ZnO ceramics, Ceram. Int. 47 (2021) 965–972. doi:10.1016/j.ceramint.2020.08.210.

[33] J. Niu, H. She, Z. Liu, M. Cheng, J. Xu, J. Liu, G. Chen, B. Tang, D. Xu, A current-controlled flash sintering processing leading to dense and fine-grained typical multi-element ZnO varistor ceramics, J. Alloys Compd. 876 (2021) 160124. doi:10.1016/j.jallcom.2021.160124.

[34] H. Gao, T.J. Asel, J.W. Cox, Y. Zhang, J. Luo, L.J. Brillson, Native point defect formation in flash sintered ZnO studied by depth-resolved cathodoluminescence spectroscopy, J. Appl. Phys. 120 (2016) 105302. doi:10.1063/1.4962316.

[35] J. Nie, Y. Zhang, J.M. Chan, S. Jiang, R. Huang, J. Luo, Two-step flash sintering of ZnO: Fast densification with suppressed grain growth, Scr. Mater. 141 (2017) 6–9. doi:10.1016/j.scriptamat.2017.07.015.

[36] Y. Zhang, J. Nie, J.M. Chan, J. Luo, Probing the densification mechanisms during flash sintering of ZnO, Acta Mater. 125 (2017) 465–475. doi:10.1016/j.actamat.2016.12.015.

[37] J. Luo, The scientific questions and technological opportunities of flash sintering: From a case study of ZnO to other ceramics, Scr. Mater. 146 (2018) 260–266. doi:10.1016/j.scriptamat.2017.12.006.

[38] H. Charalambous, S.K. Jha, R.T. Lay, A. Cabales, J. Okasinski, T. Tsakalakos, Investigation of temperature approximation methods during flash sintering of ZnO, Ceram. Int. 44 (2018) 6162–6169. doi:10.1016/j.ceramint.2017.12.250.

[39] H. Charalambous, S.K. Jha, K.H. Christian, R.T. Lay, T. Tsakalakos, Flash Sintering using Controlled Current Ramp, J. Eur. Ceram. Soc. 38 (2018) 3689–3693. doi:10.1016/j.jeurceramsoc.2018.04.003.

[40] J. Nie, Y. Zhang, J.M. Chan, R. Huang, J. Luo, Water-assisted flash sintering: Flashing ZnO at room temperature to achieve ~ 98% density in seconds, Scr. Mater. 142 (2018) 79–82. doi:10.1016/j.scriptamat.2017.08.032.

[41] X. Hao, Y. Liu, Z. Wang, J. Qiao, K. Sun, A novel sintering method to obtain fully dense gadolinia doped ceria by applying a direct current, J. Power Sources. 210 (2012) 86–91. doi:10.1016/j.jpowsour.2012.03.006.

[42] T. Jiang, Z. Wang, J. Zhang, X. Hao, D. Rooney, Y. Liu, W. Sun, J. Qiao, K. Sun, Understanding the flash sintering of rare-earth-doped ceria for solid oxide fuel cell, J. Am. Ceram. Soc. 98 (2015) 1717–1723. doi:10.1111/jace.13526.

[43] M. Biesuz, G. Dell'Agli, L. Spiridigliozzi, C. Ferone, V.M. Sglavo, Conventional and field-assisted sintering of nanosized Gd-doped ceria synthesized by co-precipitation, Ceram. Int. 42 (2016) 11766–11771. doi:10.1016/j.ceramint.2016.04.097.

[44] L. Spiridigliozzi, M. Biesuz, G. Dell'Agli, E. Di Bartolomeo, F. Zurlo, V.M. Sglavo, Microstructural and electrical investigation of flash-sintered Gd/Sm-doped ceria, J. Mater. Sci. 52 (2017) 7479–7488. doi:10.1007/s10853-017-0980-2.

[45] S.K. Jha, H. Charalambous, H.H. Wang, X.L. Phuah, C. Mead, J. Okasinski, H.H. Wang, T. Tsakalakos, In-situ observation of oxygen mobility and abnormal lattice expansion in ceria during flash sintering, Ceram. Int. 44 (2018) 15362–15369. doi:10.1016/j.ceramint.2018.05.186.

[46] L. Spiridigliozzi, L. Pinter, M. Biesuz, G. Dell'Agli, G. Accardo, V.M. Sglavo, Gd/Sm-Pr co-doped ceria: A first report of the precipitation method effect on flash sintering, Materials (Basel). 12 (2019). doi:10.3390/ma12081218.

[47] T.P. Mishra, R.R.I. Neto, G. Speranza, A. Quaranta, V.M. Sglavo, R. Raj, O. Guillon, M. Bram, M. Biesuz, Electronic conductivity in gadolinium doped ceria under direct current as a trigger for flash sintering, Scr. Mater. 179 (2020) 55–60. doi:10.1016/j.scriptamat.2020.01.007.

[48] T.P. Mishra, R.R.I. Neto, R. Raj, O. Guillon, M. Bram, Current-rate flash sintering of gadolinium doped ceria: Microstructure and Defect generation, Acta Mater. 189 (2020) 145–153. doi:10.1016/j.actamat.2020.02.036.

[49] X.L. Phuah, H.H. Wang, Z. Qi, S. Misra, M. Kalaswad, H.H. Wang, Field-assisted heating of Gd-doped ceria thin film, J. Am. Ceram. Soc. 103 (2020) 2309–2314. doi:10.1111/jace.16949.

[50] S.K. Jha, R. Raj, The effect of electric field on sintering and electrical conductivity of Titania, J. Am. Ceram. Soc. 97 (2014) 527–534. doi:10.1111/jace.12682.

[51] S.K. Jha, J.M. Lebrun, K.C. Seymour, W.M. Kriven, R. Raj, Electric field induced texture in titania during experiments related to flash sintering, J. Eur. Ceram. Soc. 36 (2016) 257–261. doi:10.1016/j.jeurceramsoc.2015.09.002.

[52] Y. Zhang, J. Nie, J. Luo, Effects of phase and doping on flash sintering of TiO2, J. Ceram. Soc. Japan. 124 (2016) 296–300. doi:10.2109/jcersj2.124.P4-1.

[53] B. Yoon, D. Yadav, R. Raj, E.P. Sortino, S. Ghose, P. Sarin, D. Shoemaker, Measurement of O and Ti atom displacements in TiO2 during flash sintering experiments, J. Am. Ceram. Soc. 101 (2018) 1811–1817. doi:10.1111/jace.15375.

[54] H. Charalambous, S.K. Jha, H.H. Wang, X.L. Phuah, H.H. Wang, T. Tsakalakos, Inhomogeneous reduction and its relation to grain growth of titania during flash sintering, Scr. Mater. 155 (2018) 37–40. doi:10.1016/j.scriptamat.2018.06.017.

[55] H. Charalambous, S.K. Jha, X.L. Phuah, H.H. Wang, H.H. Wang, J.S. Okasinski, T. Tsakalakos, In situ measurement of temperature and reduction of rutile titania using energy dispersive x-ray diffraction, J. Eur. Ceram. Soc. 38 (2018) 5503–5511. doi:10.1016/j.jeurceramsoc.2018.08.032.

[56] H. Wang, X.L. Phuah, H. Charalambous, S.K. Jha, J. Li, T. Tsakalakos, X. Zhang, H. Wang, Staged microstructural study of flash sintered titania, Materialia. 8 (2019) 100451. doi:10.1016/j.mtla.2019.100451.

[57] J. Li, J. Cho, J. Ding, H. Charalambous, S. Xue, H. Wang, X.L. Phuah, J. Jian, X. Wang, C. Ophus, T. Tsakalakos, R.E. García, A.K. Mukherjee, N. Bernstein, C.S. Hellberg, H. Wang, X. Zhang, Nanoscale stacking fault–assisted room temperature plasticity in flash-sintered TiO2, Sci. Adv. 5 (2019) eaaw5519. doi:10.1126/sciadv.aaw5519.

[58] M. Jongmanns, D.E. Wolf, Element-specific displacements in defect-enriched TiO2: Indication of a flash sintering mechanism, J. Am. Ceram. Soc. 103 (2020) 589–596. doi:10.1111/jace.16696.

[59] Q. Wang, C.S. Watts, C.E. Athanasiou, Z. Dai, M. Hu, B.W. Sheldon, N.P. Padture, The effect of atmosphere on the flash-sintering of nanoscale titania ceramics, Scr. Mater. 199 (2021) 113894. doi:10.1016/j.scriptamat.2021.113894.

[60] A. Karakuscu, M. Cologna, D. Yarotski, J. Won, J.S.C. Francis, R. Raj, B.P. Uberuaga, Defect structure of flash-sintered strontium titanate, J. Am. Ceram. Soc. 95 (2012) 2531–2536. doi:10.1111/j.1551-2916.2012.05240.x.

[61] F. Lemke, W. Rheinheimer, M.J. Hoffmann, A comparison of power controlled flash sintering and conventional sintering of strontium titanate, Scr. Mater. 130 (2017) 187–190. doi:10.1016/j.scriptamat.2016.12.008.

[62] Y. Nakagawa, H. Yoshida, A. Uehashi, T. Tokunaga, K. Sasaki, T. Yamamoto, Electric current-controlled synthesis of BaTiO3, J. Am. Ceram. Soc. 100 (2017) 3843–3850. doi:10.1111/jace.14938.

[63] R. Shi, Y. Pu, W. Wang, Y. Shi, J. Li, X. Guo, M. Yang, Flash sintering of barium titanate, Ceram. Int. 45 (2019) 7085–7089. doi:10.1016/j.ceramint.2018.12.211.

[64] B. Ma, Y. Zhu, K. Wang, Z. Sun, D. Liu, G. Shao, J. Liu, Y. Wang, Microstructure and dielectric property of flash sintered SiO2-coated BaTiO3 ceramics, Scr. Mater. 170 (2019) 1–5. doi:10.1016/j.scriptamat.2019.05.019.

[65] R. Umemura, T. Tokunaga, T. Yamamoto, Flash sintering for BaTiO3 with square alternating current field including zero-field duration, J. Ceram. Soc. Japan. 128 (2020) 1018–1023. doi:10.2109/jcersj2.20181.

[66] R. Shi, Y. Pu, J. Ji, J. Li, X. Guo, W. Wang, M. Yang, Correlation between flash sintering and dielectric breakdown behavior in donor-doped barium titanate ceramics, Ceram. Int. 46 (2020) 12846–12851. doi:10.1016/j.ceramint.2020.02.055.

[67] K. Ren, S. Huang, Y. Cao, G. Shao, Y. Wang, The densification behavior of flash sintered BaTiO3, Scr. Mater. 186 (2020) 362–365. doi:10.1016/j.scriptamat.2020.05.005.

[68] N. Shomrat, S. Baltianski, E. Dor, Y. Tsur, The influence of doping on flash sintering conditions in SrTi1−xFexO3−δ, J. Eur. Ceram. Soc. 37 (2017) 179–188. doi:10.1016/j.jeurceramsoc.2016.07.037.

[69] W. Rheinheimer, X.L. Phuah, H.H. Wang, F. Lemke, M.J. Hoffmann, H.H. Wang, The role of point defects and defect gradients in flash sintering of perovskite oxides, Acta Mater. 165 (2019) 398–408. doi:10.1016/j.actamat.2018.12.007.

[70] B. Kayaalp, K. Klauke, M. Biesuz, A. Iannaci, V.M. Sglavo, M. D'Arienzo, H. Noei, S. Lee, W. Jung, S. Mascotto, Surface Reconstruction under the Exposure of Electric Fields Enhances the Reactivity of Donor-Doped SrTiO3, J. Phys. Chem. C. 123 (2019) 16883–16892. doi:10.1021/acs.jpcc.9b04620.

[71] K. Klauke, B. Kayaalp, M. Biesuz, A. Iannaci, V.M. Sglavo, M. D'Arienzo, S. Lee, J. Seo, W.C. Jung, S. Mascotto, Enhancement of the SrTiO3 Surface Reactivity by Exposure to Electric Fields, ChemNanoMat. 5 (2019) 948–956. doi:10.1002/cnma.201900201.

[72] J.C. M'Peko, J.S.C. Francis, R. Raj, Field-assisted sintering of undoped BaTiO3: Microstructure evolution and dielectric permittivity, J. Eur. Ceram. Soc. 34 (2014) 3655–3660. doi:10.1016/j.jeurceramsoc.2014.04.041.

[73] A. Uehashi, K. Sasaki, T. Tokunaga, H. Yoshida, T. Yamamoto, Formation of secondary phase at grain boundary of flash-sintered BaTiO3 Akinori, Microscopy. 63 (2014) i19–i20. doi:10.1093/jmicro/dfu059.

[74] A. Uehashi, H. Yoshida, T. Tokunaga, K. Sasaki, T. Yamamoto, Enhancement of sintering rates in BaTiO3 by controlling of DC electric current, J. Ceram. Soc. Japan. 123 (2015) 465–468. doi:10.2109/jcersj2.123.465.

[75] H. Yoshida, A. Uehashi, T. Tokunaga, K. Sasaki, T. Yamamoto, Formation of grain boundary second phase in BaTiO3 polycrystal under a high DC electric field at elevated temperatures, J. Ceram. Soc. Japan. 124 (2016) 388–392. doi:10.2109/jcersj2.15259.

[76] M. Cologna, J.S.C. Francis, R. Raj, Field assisted and flash sintering of alumina and its relationship to conductivity and MgO-doping, J. Eur. Ceram. Soc. 31 (2011) 2827–2837. doi:10.1016/j.jeurceramsoc.2011.07.004.

[77] M. Biesuz, V.M. Sglavo, Flash sintering of alumina: Effect of different operating conditions on densification, J. Eur. Ceram. Soc. 36 (2016) 2535–2542. doi:10.1016/j.jeurceramsoc.2016.03.021.

[78] M. Biesuz, P. Luchi, A. Quaranta, V.M. Sglavo, Theoretical and phenomenological analogies between flash sintering and dielectric breakdown in α-alumina, J. Appl. Phys. 120 (2016). doi:10.1063/1.4964811.

[79] M. Biesuz, V.M. Sglavo, Current-induced abnormal and oriented grain growth in corundum upon flash sintering, Scr. Mater. 150 (2018) 82–86. doi:10.1016/j.scriptamat.2018.03.004.

[80] J. Gonzalez-Julian, O. Guillon, Effect of Electric Field/Current on Liquid Phase Sintering, J. Am. Ceram. Soc. 98 (2015) 2018–2027. doi:10.1111/jace.13571.

[81] C. McLaren, W. Heffner, R. Tessarollo, R. Raj, H. Jain, Electric field-induced softening of alkali silicate glasses, Appl. Phys. Lett. 107 (2015) 1–6. doi:10.1063/1.4934945.

[82] W. Lerdprom, C. Li, D.D. Jayaseelan, S.J. Skinner, W.E. Lee, Temperature dependence of electrical conductivity of a green porcelain mixture, J. Eur. Ceram. Soc. 37 (2017) 343–349. doi:10.1016/j.jeurceramsoc.2016.08.019.

[83] C. McLaren, B. Roling, R. Raj, H. Jain, Mechanism of electric field-induced softening (EFIS) of alkali silicate glasses, J. Non. Cryst. Solids. 471 (2017) 384–395. doi:10.1016/j.jnoncrysol.2017.06.025.

[84] M.O. Prado, M. Biesuz, M. Frasnelli, F.E. Benedetto, V.M. Sglavo, Viscous flow flash sintering of porous silica glass, J. Non. Cryst. Solids. 476 (2017) 60–66. doi:10.1016/j.jnoncrysol.2017.09.024.

[85] R. Ma, D. Erb, K. Lu, Flash pyrolysis of polymer-derived SiOC ceramics, J. Eur. Ceram. Soc. 38 (2018) 4906–4914. doi:10.1016/j.jeurceramsoc.2018.07.010.

[86] L. Pinter, M. Biesuz, V.M. Sglavo, T. Saunders, J. Binner, M. Reece, S. Grasso, DC-electro softening in soda lime silicate glass: An electro-thermal analysis, Scr. Mater. 151 (2018) 14–18. doi:10.1016/j.scriptamat.2018.03.028.

[87] L. Wang, K. Lu, Phase development of silicon oxycarbide nanocomposites during flash pyrolysis, J. Mater. Sci. 54 (2019) 6073–6087. doi:10.1007/s10853-019-03315-z.

[88] K. Lu, D. Erb, K. Bawane, N. Yang, Comparison of traditional and flash pyrolysis of different carbon content silicon oxycarbides, J. Eur. Ceram. Soc. 39 (2019) 3035–3041. doi:10.1016/j.jeurceramsoc.2019.03.051.

[89] A.M. Raftery, J.G. Pereira da Silva, D.D. Byler, D.A. Andersson, B.P. Uberuaga, C.R. Stanek, K.J. McClellan, Onset conditions for flash sintering of UO2, J. Nucl. Mater. 493 (2017) 264–270. doi:10.1016/j.jnucmat.2017.06.022.

[90] D.J. Sprouster, E. Kardoulaki, R. Weidner, A.M. Raftery, M. Elbakhshwan, R. Pokharel, H.M. Reiche, D.D. Byler, S.K. Ghose, E. Dooryhee, K.J. McClellan, L.E. Ecker, In situ X-ray characterization of uranium dioxide during flash sintering, Materialia. 2 (2018) 176–182. doi:10.1016/j.mtla.2018.07.006.

[91] J.A. Valdez, D.D. Byler, E. Kardoulaki, J.S.C. Francis, K.J. McClellan, Flash sintering of stoichiometric and hyper-stoichiometric urania, J. Nucl. Mater. 505 (2018) 85–93. doi:10.1016/j.jnucmat.2018.03.049.

[92] R.R. Ingraci Neto, K.J. McClellan, D.D. Byler, E. Kardoulaki, Controlled current-rate AC flash sintering of uranium dioxide, J. Nucl. Mater. 547 (2021) 152780. doi:10.1016/j.jnucmat.2021.152780.

[93] W. Straka, S. Amoah, J. Schwartz, Densification of thoria through flash sintering, MRS Commun. 7 (2017) 677–682. doi:10.1557/mrc.2017.70.

[94] E. Bichaud, J.M. Chaix, C. Carry, M. Kleitz, M.C. Steil, Flash sintering incubation in Al2O3/TZP composites, J. Eur. Ceram. Soc. 35 (2015) 2587–2592. doi:10.1016/j.jeurceramsoc.2015.02.033.

[95] S.K. Jha, J.M. Lebrun, R. Raj, Phase transformation in the alumina-titania system during flash sintering experiments, J. Eur. Ceram. Soc. 36 (2016) 733–739. doi:10.1016/j.jeurceramsoc.2015.10.006.

[96] D. Kok, S.K. Jha, R. Raj, M.L. Mecartney, Flash sintering of a three-phase alumina, spinel, and yttria-stabilized zirconia composite, J. Am. Ceram. Soc. 100 (2017) 3262–3268. doi:10.1111/jace.14818.

[97] D. Kok, D. Yadav, E. Sortino, S.J. McCormack, K.-P. Tseng, W.M. Kriven, R. Raj, M.L. Mecartney, α-Alumina and spinel react into single-phase high-alumina spinel in <3 seconds during flash sintering, J. Am. Ceram. Soc. 100 (2018) 3262–3268. doi:10.1111/jace.15927.

[98] W. Ji, J. Zhang, W. Wang, Z. Fu, R. Todd, The microstructural origin of rapid densification in 3YSZ during ultra-fast firing with or without an electric field, J. Eur. Ceram. Soc. 40 (2020) 5829–5836. doi:10.1016/j.jeurceramsoc.2020.07.027.

[99] S.W. Kim, S.G. Kim, J. Il Jung, S.J.L. Kang, I.W. Chen, Enhanced grain boundary mobility in yttria-stabilized cubic zirconia under an electric current, J. Am. Ceram. Soc. 94 (2011) 4231–4238. doi:10.1111/j.1551-2916.2011.04800.x.

[100] M. Biesuz, L. Pinter, T. Saunders, M. Reece, J. Binner, V. Sglavo, S. Grasso, Investigation of Electrochemical, Optical and Thermal Effects during Flash Sintering of 8YSZ, Materials (Basel). 11 (2018) 1214. doi:10.3390/ma11071214.

[101] Y. Dong, On the Hotspot Problem in Flash Sintering, (2017) 1–8. http://arxiv.org/abs/1702.05565.

[102] M. Yu, S. Grasso, R. Mckinnon, T. Saunders, M.J. Reece, Review of flash sintering: materials, mechanisms and modelling, Adv. Appl. Ceram. 116 (2017) 24–60. doi:10.1080/17436753.2016.1251051.

[103] M.C. Steil, D. Marinha, Y. Aman, J.R.C. Gomes, M. Kleitz, From conventional ac flash-sintering of YSZ to hyper-flash and double flash, J. Eur. Ceram. Soc. 33 (2013) 2093–2101. doi:10.1016/j.jeurceramsoc.2013.03.019.

[104] I. R. Lavagnini, J. V. Campos, J.A. Ferreira, E.M.J. Eliria, Microstructural evolution of 3YSZ flash-sintered with current ramp control, J. Am. Ceram. Soc. 103 (2020) 3493–3499. doi:10.1111/jace.17037.

[105] J. V. Campos, I.R. Lavagnini, J.G. Pereira da Silva, J.A. Ferreira, R. V. Sousa, R. Mücke, O. Guillon, E.M.J.A. Pallone, Flash sintering scaling-up challenges: Influence of the sample size on the microstructure and onset temperature of the flash event, Scr. Mater. 186 (2020) 1–5. doi:10.1016/j.scriptamat.2020.04.022.

[106] B. Yang, J. Cho, X.L. Phuah, H. Wang, X. Zhang, Flash sintering of additively manufactured 3YSZ gears, J. Am. Ceram. Soc. (2021) jace.17835. doi:10.1111/jace.17835.

[107] L.B. Caliman, R. Bouchet, D. Gouvea, P. Soudant, M.C. Steil, Flash sintering of ionic conductors: The need of a reversible electrochemical reaction, J. Eur. Ceram. Soc. 36 (2016) 1253–1260. doi:10.1016/j.jeurceramsoc.2015.12.005.

[108] M. Yoshida, S. Falco, R.I. Todd, Measurement and modelling of electrical resistivity by four-terminal method during flash sintering of 3YSZ, J. Ceram. Soc. Japan. 126 (2018) 579–590. doi:10.2109/jcersj2.17256.

[109] M. Biesuz, J. Dong, S. Fu, Y. Liu, H. Zhang, D. Zhu, C. Hu, S. Grasso, Thermally-insulated flash sintering, Scr. Mater. 162 (2019) 99–102. doi:10.1016/j.scriptamat.2018.10.042.

[110] E. Sortino, J.M. Lebrun, A. Sansone, R. Raj, Continuous flash sintering, J. Am. Ceram. Soc. 101 (2018) 1432–1440. doi:10.1111/jace.15314.

[111] J. Dong, Z. Wang, X. Zhao, M. Biesuz, T. Saunders, Z. Zhang, C. Hu, S. Grasso, Contactless flash sintering based on cold plasma, Scr. Mater. 175 (2020) 20–23. doi:10.1016/j.scriptamat.2019.08.039.

[112] J.S.C. Francis, R. Raj, Flash-sinterforging of nanograin zirconia: Field assisted sintering and superplasticity, J. Am. Ceram. Soc. 95 (2012) 138–146. doi:10.1111/j.1551-2916.2011.04855.x.

[113] S. Grasso, T. Saunders, H. Porwal, O. Cedillos-Barraza, D.D. Jayaseelan, W.E. Lee, M.J. Reece, Flash Spark Plasma Sintering (FSPS) of Pure ZrB_2, J. Am. Ceram. Soc. 97 (2014) 2405–2408. doi:10.1111/jace.13109.

[114] M. Biesuz, R. Sedlák, T. Saunders, A. Kovalčíková, J. Dusza, M. Reece, D. Zhu, C. Hu, S. Grasso, Flash spark plasma sintering of 3YSZ, J. Eur. Ceram. Soc. 39 (2019) 1932–1937. doi:10.1016/j.jeurceramsoc.2019.01.017.

[115] J. Zou, S. Grasso, L.F. Liu, H. Bin Ma, M. Reece, J. Binner, Flash spark plasma sintering of HfB2 ceramics without pre-sintering, Scr. Mater. 156 (2018) 115–119. doi:10.1016/j.scriptamat.2018.07.026.

[116] S. Grasso, E.Y. Kim, T. Saunders, M. Yu, A. Tudball, S.H. Choi, M. Reece, Ultra-Rapid Crystal Growth of Textured SiC Using Flash Spark Plasma Sintering Route, Cryst. Growth Des. 16 (2016) 2317–2321. doi:10.1021/acs.cgd.6b00099.

[117] S. Grasso, T. Saunders, H. Porwal, B. Milsom, A. Tudball, M. Reece, I.W. Chen, Flash Spark Plasma Sintering (FSPS) of α and β SiC, J. Am. Ceram. Soc. 99 (2016) 1534–1543. doi:10.1111/jace.14158.

[118] S.K. Jha, K. Terauds, J.-M. Lebrun, R. Raj, Beyond flash sintering in 3 mol % yttria stabilized zirconia, J. Ceram. Soc. Japan. 124 (2016) 283–288. doi:10.2109/jcersj2.15248.

[119] J.S.C. Francis, R. Raj, Influence of the field and the current limit on flash sintering at isothermal furnace temperatures, J. Am. Ceram. Soc. 96 (2013) 2754–2758. doi:10.1111/jace.12472.

[120] J.S.C. Francis, M. Cologna, R. Raj, Particle size effects in flash sintering, J. Eur. Ceram. Soc. 32 (2012) 3129–3136. doi:10.1097/01.CCM.0000284750.62544.29.

[121] H. Wang, X.L. Phuah, J. Li, T.B. Holland, K.S.N. Vikrant, Q. Li, C.S. Hellberg, N. Bernstein, R.E. García, A. Mukherjee, X. Zhang, H. Wang, Key microstructural characteristics in flash sintered 3YSZ critical for enhanced sintering process, Ceram. Int. 45 (2019) 1251–1257. doi:10.1016/j.ceramint.2018.10.007.

[122] D. Liu, Y. Cao, J. Liu, Y. Gao, Y. Wang, Effect of oxygen partial pressure on temperature for onset of flash sintering 3YSZ, J. Eur. Ceram. Soc. 38 (2018) 817–820. doi:10.1016/j.jeurceramsoc.2017.09.009.

[123] K.S. Naik, V.M. Sglavo, R. Raj, Flash sintering as a nucleation phenomenon and a model thereof, J. Eur. Ceram. Soc. 34 (2014) 4063–4067. doi:10.1016/j.jeurceramsoc.2014.04.043.

[124] K.S.N. Vikrant, H. Wang, A. Jana, H. Wang, R.E. García, Flash sintering incubation kinetics, Npj Comput. Mater. (2020) 1–8. doi:10.1038/s41524-020-00359-7.

[125] W. Qin, H. Majidi, J. Yun, K. van Benthem, Electrode Effects on Microstructure Formation During FLASH Sintering of Yttrium-Stabilized Zirconia, J. Am. Ceram. Soc. 99 (2016) 2253–2259. doi:10.1111/jace.14234.

[126] W. Ji, B. Parker, S. Falco, J.Y. Zhang, Z.Y. Fu, R.I. Todd, Ultra-fast firing: Effect of heating rate on sintering of 3YSZ, with and without an electric field, J. Eur. Ceram. Soc. 37 (2017) 2547–2551. doi:10.1016/j.jeurceramsoc.2017.01.033.

[127] S. Grasso, Y. Sakka, N. Rendtorff, C. Hu, G. Maizza, H. Borodianska, O. Vasylkiv, Modeling of the temperature distribution of flash sintered zirconia, J. Ceram. Soc. Japan. 119 (2011) 144–146. doi:10.2109/jcersj2.119.144.

[128] X.L. Phuah, J. Jian, H. Wang, X. Wang, X. Zhang, H. Wang, Ultra-high heating rate effects on the sintering of ceramic nanoparticles: an in situ TEM study, Mater. Res. Lett. 9 (2021) 373–381. doi:10.1080/21663831.2021.1927878.

[129] W. Rheinheimer, X.L. Phuah, L. Porz, M. Scherer, J. Cho, H. Wang, The interplay of high heating rate sintering and plasticity: Does flash sintering involve plastic flow?, (2021) under review.

[130] H. Yoshida, Y. Sasaki, Low temperature and high strain rate superplastic flow in structural ceramics induced by strong electric-field, Scr. Mater. 146 (2018) 173–177. doi:10.1016/j.scriptamat.2017.11.042.

[131] C. Cao, Y. Sasaki, R. Mücke, K. Morita, O. Guillon, Experimental confirmation of the symmetric sintering behavior under compressive/tensile loading combined with electrical field, Scr. Mater. 187 (2020) 137–141. doi:10.1016/j.scriptamat.2020.05.003.

[132] M. Biesuz, P. Luchi, A. Quaranta, A. Martucci, V.M. Sglavo, Photoemission during flash sintering: An interpretation based on thermal radiation, J. Eur. Ceram. Soc. 37 (2017) 3125–3130. doi:10.1016/j.jeurceramsoc.2017.03.050.

[133] M. Biesuz, V.M. Sglavo, Beyond flash sintering: How the flash event could change ceramics and glass processing, Scr. Mater. 187 (2020) 49–56. doi:10.1016/j.scriptamat.2020.05.065.

[134] R. Raj, Joule heating during flash-sintering, J. Eur. Ceram. Soc. 32 (2012) 2293–2301. doi:10.1016/j.jeurceramsoc.2012.02.030.

[135] J.M. Lebrun, R. Raj, A first report of photoemission in experiments related to flash sintering, J. Am. Ceram. Soc. 97 (2014) 2427–2430. doi:10.1111/jace.13130.

[136] K. Terauds, J.M. Lebrun, H.H. Lee, T.Y. Jeon, S.H. Lee, J.H. Je, R. Raj, Electroluminescence and the measurement of temperature during Stage III of flash sintering experiments, J. Eur. Ceram. Soc. 35 (2015) 3195–3199. doi:10.1016/j.jeurceramsoc.2015.03.040.

[137] M. Schie, S. Menzel, J. Robertson, R. Waser, R.A. De Souza, Field-enhanced route to generating anti-Frenkel pairs in HfO2, Phys. Rev. Mater. 2 (2018). doi:10.1103/PhysRevMaterials.2.035002.

[138] R. Chaim, Liquid Film Capillary Mechanism for Densification of Ceramic Powders during Flash Sintering, Materials (Basel). 9 (2016) 280. doi:10.3390/ma9040280.

[139] R. Chaim, Effect of the liquid fragility on flash sintering behavior of oxide nanoparticles, Scr. Mater. 178 (2020) 261–263. doi:10.1016/j.scriptamat.2019.11.046.

[140] J. Narayan, A new mechanism for field-assisted processing and flash sintering of materials, Scr. Mater. 69 (2013) 107–111. doi:10.1016/j.scriptamat.2013.02.020.

[141] J. Narayan, Grain growth model for electric field-assisted processing and flash sintering of materials, Scr. Mater. 68 (2013) 785–788. doi:10.1016/j.scriptamat.2013.01.008.

[142] S. V. Egorov, A.G. Eremeev, V. V. Kholoptsev, I. V. Plotnikov, K.I. Rybakov, A.A. Sorokin, Y. V. Bykov, On the correlation between the thermal instability onset and the flash sintering event, Scr. Mater. 174 (2020) 68–71. doi:10.1016/j.scriptamat.2019.08.032.

[143] J. Nie, C. Hu, Q. Yan, J. Luo, Discovery of electrochemically induced grain boundary transitions, Nat. Commun. 12 (2021) 1–10. doi:10.1038/s41467-021-22669-0.

[144] H. Yoshida, P. Biswas, R. Johnson, M.K. Mohan, Flash-sintering of magnesium aluminate spinel (MgAl2O4) ceramics, J. Am. Ceram. Soc. 100 (2017) 554–562. doi:10.1111/jace.14616.

[145] C.A. Grimley, A.L.G. Prette, E.C. Dickey, Effect of boundary conditions on reduction during early stage flash sintering of YSZ, Acta Mater. 174 (2019) 271–278. doi:10.1016/j.actamat.2019.05.001.

[146] J. Cho, Q. Li, H. Wang, Z. Fan, J. Li, S. Xue, K.S.N. Vikrant, H. Wang, T.B. Holland, A.K. Mukherjee, R.E. García, X. Zhang, High temperature deformability of ductile flash-sintered ceramics via in-situ compression, Nat. Commun. 9 (2018) 1–9. doi:10.1038/s41467-018-04333-2.

[147] J.A. Downs, Mechanism of flash sintering in cubic zirconia, University of Toronto, 2013.

[148] J. Janek, C. Korte, Electrochemical blackening of yttria-stabilized zirconia - Morphological instability of the moving reaction front, Solid State Ionics. 116 (1999) 181–195. doi:10.1016/s0167-2738(98)00415-9.

[149] R.E.W. Casselton, Blackening in yttria stabilized zirconia due to cathodic processes at solid platinum electrodes, 4 (1974) 25–48.

[150] X.L. Phuah, J. Cho, T. Tsakalakos, A.K. Mukherjee, H. Wang, X. Zhang, Defects in flash-sintered ceramics and their effects on mechanical properties, MRS Bull. 46 (2021) 44–51. doi:10.1557/s43577-020-00014-y.

[151] S. Jo, R. Raj, Transition to electronic conduction at the onset of flash in cubic zirconia, Scr. Mater. 174 (2020) 29–32. doi:10.1016/j.scriptamat.2019.07.043.

[152] V. Esposito, D.W. Ni, D. Marani, F. Teocoli, K.T.S. Thydén, D.Z. De Florio, F.C. Fonseca, Accelerated ceria-zirconia solubilization by cationic diffusion inversion at low oxygen activity, J. Mater. Chem. A. 4 (2016) 16871–16878. doi:10.1039/c6ta06308j.

[153] Y. Dong, I.-W. Chen, Oxygen potential transition in mixed conducting oxide electrolyte, Acta Mater. 156 (2018) 399–410. doi:10.1016/j.actamat.2018.06.014.

[154] K.S.N. Vikrant, X.L. Phuah, J. Lund, H. Wang, C.S. Hellberg, N. Bernstein, W. Rheinheimer, C.M. Bishop, H. Wang, R.E. García, Modeling of flash sintering of ionic ceramics, MRS Bull. 46 (2021) 67–75. doi:10.1557/s43577-020-00012-0.

[155] W. Rheinheimer, J.P. Parras, J.-H. Preusker, R.A. De Souza, M.J. Hoffmann, Grain growth in strontium titanate in electric fields: The impact of space-charge on the grain-boundary mobility, J. Am. Ceram. Soc. 102 (2019) 3779–3790. doi:10.1111/jace.16217.

[156] B.F. Donovan, D.M. Long, A. Moballegh, N. Creange, E.C. Dickey, P.E. Hopkins, Impact of intrinsic point defect concentration on thermal transport in titanium dioxide, Acta Mater. 127 (2017) 491–497. doi:10.1016/j.actamat.2017.01.018.

[157] J.M. Lebrun, T.G. Morrissey, J.S.C. Francis, K.C. Seymour, W.M. Kriven, R. Raj, Emergence and extinction of a new phase during on-off experiments related to flash sintering of 3YSZ, J. Am. Ceram. Soc. 98 (2015) 1493–1497. doi:10.1111/jace.13476.

[158] J.M. Lebrun, S.K. Jha, S.J. McCormack, W.M. Kriven, R. Raj, H. Chan, Broadening of Diffraction Peak Widths and Temperature Nonuniformity During Flash Experiments, J. Am. Ceram. Soc. 99 (2016) 3429–3434. doi:10.1111/jace.14326.

[159] J.M. Lebrun, C.S. Hellberg, S.K. Jha, W.M. Kriven, A. Steveson, K.C. Seymour, N. Bernstein, S.C. Erwin, R. Raj, In-situ measurements of lattice expansion related to defect generation during flash sintering, J. Am. Ceram. Soc. 100 (2017) 4965–4970. doi:10.1111/jace.15071.

[160] E.K. Akdoğan, I. Şavkliyildiz, H. Biçer, W. Paxton, F. Toksoy, Z. Zhong, T. Tsakalakos, Anomalous lattice expansion in yttria stabilized zirconia under simultaneous applied electric and thermal fields: A time-resolved in situ energy dispersive x-ray diffractometry study with an ultrahigh energy synchrotron probe, J. Appl. Phys. 113 (2013). doi:10.1063/1.4811362.

[161] H. Charalambous, S.K. Jha, J. Okasinski, T. Tsakalakos, Spectral analysis and temperature measurement during flash sintering under AC electric field, Materialia. 6 (2019) 100273. doi:10.1016/j.mtla.2019.100273.

[162] H. Charalambous, S. Krishn, R.T. Lay, A. Cabales, J. Okasinski, T. Tsakalakos, Investigation of temperature approximation methods during fl ash sintering of ZnO, Ceram. Int. 44 (2018) 6162–6169. doi:10.1016/j.ceramint.2017.12.250.

[163] M.A.B. Wassel, L.A. Pérez-Maqueda, E. Gil-Gonzalez, H. Charalambous, A. Perejon, S.K. Jha, J. Okasinski, T. Tsakalakos, Anisotropic lattice expansion determined during flash sintering of BiFeO3 by in-situ energy-dispersive X-ray diffraction, Scr. Mater. 162 (2019) 286–291. doi:10.1016/j.scriptamat.2018.11.028.

[164] L.A. Perez-Maqueda, E. Gil-Gonzalez, M.A. Wassel, S.K. Jha, A. Perejon, H. Charalambous, J. Okasinski, P.E. Sanchez-Jimenez, T. Tsakalakos, Insight into the BiFeO3 flash sintering process by in-situ energy dispersive X-ray diffraction (ED-XRD), Ceram. Int. 45 (2019) 2828–2834. doi:10.1016/j.ceramint.2018.07.293.

[165] T.E. Özdemir, E.K. Akdoğan, İ. Şavklıyıldız, H. Biçer, M. Örnek, Z. Zhong, T. Tsakalakos, Electric field effect on chemical and phase equilibria in nano-TiB2–TiO2–TiBO3 system at <650 °C: an in situ time-resolved energy dispersive x-ray diffraction study with an ultrahigh energy synchrotron probe, J. Mater. Res. 32 (2017) 482–494. doi:10.1557/jmr.2016.466.

[166] B. Yoon, D. Yadav, S. Ghose, P. Sarin, R. Raj, On the synchronicity of flash sintering and phase transformation, J. Am. Ceram. Soc. 102 (2019) 3110–3116. doi:10.1111/jace.16335.

[167] B. Yoon, D. Yadav, S. Ghose, R. Raj, Reactive flash sintering: MgO and α-Al2O3 transform and sinter into single-phase polycrystals of MgAl2O4, J. Am. Ceram. Soc. 102 (2018) jace.15974. doi:10.1111/jace.15974.

[168] V. Avila, B. Yoon, R.R. Ingraci Neto, R.S. Silva, S. Ghose, R. Raj, L.M. Jesus, Reactive flash sintering of the complex oxide Li0.5La0.5TiO3 starting from an amorphous precursor powder, Scr. Mater. 176 (2020) 78–82. doi:10.1016/j.scriptamat.2019.09.037.

[169] V. Avila, B. Yoon, S. Ghose, R. Raj, L.M. Jesus, Phase evolution during reactive flash sintering of Li6.25Al0.25La3Zr2O12 starting from a chemically prepared powder, J. Eur. Ceram. Soc. 41 (2021) 4552–4557. doi:10.1016/j.jeurceramsoc.2021.02.054.

[170] H. Majidi, K. Van Benthem, Consolidation of partially stabilized ZrO2 in the presence of a noncontacting electric field, Phys. Rev. Lett. 114 (2015) 1–5. doi:10.1103/PhysRevLett.114.195503.

[171] D. Schwarzbach, J. Gonzalez-Julian, O. Guillon, V. Roddatis, C.A. Volkert, Towards In-Situ Electron Microscopy Studies of Flash Sintering, Ceramics. 2 (2019) 472–487. doi:10.3390/ceramics2030036.

[172] R. Muccillo, E.N.S. Muccillo, Light emission during electric field-assisted sintering of electroceramics, J. Eur. Ceram. Soc. 35 (2015) 1653–1656. doi:10.1016/j.jeurceramsoc.2014.11.013.

[173] G. Liu, D. Liu, J. Liu, Y. Gao, Y. Wang, Asymmetric temperature distribution during steady stage of flash sintering dense zirconia, J. Eur. Ceram. Soc. 38 (2018) 2893–2896. doi:10.1016/j.jeurceramsoc.2018.02.012.

[174] J.H. Yu, B.A. McWilliams, T.C. Parker, Densification behavior of flash sintered boron suboxide, J. Am. Ceram. Soc. 101 (2018) 4976–4982. doi:10.1111/jace.15776.

[175] J. Park, I.-W. Chen, In Situ Thermometry Measuring Temperature Flashes Exceeding 1,700°C in 8 mol% Y2O3-Stablized Zirconia Under Constant-Voltage Heating, J. Am. Ceram. Soc. 96 (2013) 697–700. doi:10.1111/jace.12176.

[176] B. Yoon, V. Avila, R. Kathiria, L.M. Jesus, Effects of powder dispersion on reactive flash sintering of 8 mol% yttria-stabilized zirconia and MgAl2O4 composites, Scr. Mater. 189 (2020) 117–121. doi:10.1016/j.scriptamat.2020.08.009.

[177] G.M. Jones, M. Biesuz, W. Ji, S.F. John, C. Grimley, C. Manière, C.E.J. Dancer, Promoting microstructural homogeneity during flash sintering of ceramics through thermal management, MRS Bull. 46 (2021) 59–66. doi:10.1557/s43577-020-00010-2.

[178] O. Guillon, R.A. De Souza, T.P. Mishra, W. Rheinheimer, Electric-field-assisted processing of ceramics: Nonthermal effects and related mechanisms, MRS Bull. 46 (2021) 52–58. doi:10.1557/s43577-020-00008-w.

[179] Z.L. Wang, Zinc oxide nanostructures: growth, properties and applications, J. Physics：Condensed Matter. 16 (2004) 829–858. doi:10.1088/0953-8984/16/25/R01.

[180] D. Brandon, W.D. Kaplan, Microstructural Characterization of Materials, John Wiley & Sons, Ltd, Chichester, UK, 2008. doi:10.1002/9780470727133.

[181] J.I. Goldstein, D.E. Newbury, J.R. Michael, N.W.M. Ritchie, J.H.J. Scott, D.C. Joy, Scanning Electron Microscopy and X-Ray Microanalysis, Springer New York, New York, NY, 2018. doi:10.1007/978-1-4939-6676-9.

[182] Y. Yan, G.M. Dalpian, M.M. Al-Jassim, S.H. Wei, Energetics and electronic structure of stacking faults in ZnO, Phys. Rev. B - Condens. Matter Mater. Phys. 70 (2004) 1–4. doi:10.1103/PhysRevB.70.193206.

[183] K.A. Alim, V.A. Fonoberov, M. Shamsa, A.A. Balandin, Micro-Raman investigation of optical phonons in ZnO nanocrystals, J. Appl. Phys. 97 (2005). doi:10.1063/1.1944222.

[184] R.L. de S. e. Silva, A. Franco, Raman spectroscopy study of structural disorder degree of ZnO ceramics, Mater. Sci. Semicond. Process. 119 (2020). doi:10.1016/j.mssp.2020.105227.

[185] M. Cologna, A.L.G. Prette, R. Raj, Flash-sintering of cubic yttria-stabilized zirconia at 750°C for possible use in SOFC manufacturing, J. Am. Ceram. Soc. 94 (2011) 316–319. doi:10.1111/j.1551-2916.2010.04267.x.

[186] A.L.G. Prette, M. Cologna, V. Sglavo, R. Raj, Flash-sintering of Co2MnO4 spinel for solid oxide fuel cell applications, J. Power Sources. 196 (2011) 2061–2065. doi:10.1016/j.jpowsour.2010.10.036.

[187] A. Gaur, V.M. Sglavo, Flash sintering of (La, Sr)(Co, Fe)O3-Gd-Doped CeO2 composite, J. Am. Ceram. Soc. 98 (2015) 1747–1752. doi:10.1111/jace.13532.

[188] S.K. Jha, X.L. Phuah, J. Luo, C.P. Grigoropoulos, H. Wang, E. García, B. Reeja-Jayan, The effects of external fields in ceramic sintering, J. Am. Ceram. Soc. 102 (2018) jace.16061. doi:10.1111/jace.16061.

[189] R. Muccillo, E.N.S. Muccillo, Electric field-assisted flash sintering of tin dioxide, J. Eur. Ceram. Soc. 34 (2014) 915–923. doi:10.1016/j.jeurceramsoc.2013.09.017.

[190] M. Schirra, R. Schneider, A. Reiser, G.M. Prinz, M. Feneberg, J. Biskupek, U. Kaiser, C.E. Krill, K. Thonke, R. Sauer, Stacking fault related 3.31-eV luminescence at 130-meV acceptors in zinc oxide, Phys. Rev. B - Condens. Matter Mater. Phys. 77 (2008) 1–10. doi:10.1103/PhysRevB.77.125215.

[191] D. Gerthsen, D. Litvinov, T. Gruber, C. Kirchner, A. Waag, Origin and consequences of a high stacking fault density in epitaxial ZnO layers, Appl. Phys. Lett. 81 (2002) 3972–3974. doi:10.1063/1.1523151.

[192] Y. Yamashita, T. Kurachi, T. Tokunaga, H. Yoshida, T. Yamamoto, Blue photo luminescence from 3 mol%Y2O3-doped ZrO2 polycrystals sintered by flash sintering under an alternating current electric field, J. Eur. Ceram. Soc. 40 (2020) 2072–2076. doi:10.1016/j.jeurceramsoc.2019.12.060.

[193] R. Muccillo, E.N.S. Muccillo, An experimental setup for shrinkage evaluation during electric field-assisted flash sintering: Application to yttria-stabilized zirconia, J. Eur. Ceram. Soc. 33 (2013) 515–520. doi:10.1016/j.jeurceramsoc.2012.09.020.

[194] W. Qin, J. Yun, A.M. Thron, K. van Benthem, Temperature gradient and microstructure evolution in AC flash sintering of 3 mol% yttria-stabilized zirconia, Mater. Manuf. Process. 32 (2017) 549–556. doi:10.1080/10426914.2016.1232814.

[195] G.C. Yi, C. Wang, W. Il Park, ZnO nanorods: Synthesis, characterization and applications, Semicond. Sci. Technol. 20 (2005). doi:10.1088/0268-1242/20/4/003.

[196] H. Conrad, D. Yang, Effect of the strength of an AC electric field compared to DC on the sintering rate and related grain size of zirconia (3Y-TZP), Mater. Sci. Eng. A. 559 (2013) 591–594. doi:10.1016/j.msea.2012.08.146.

[197] V. Russo, M. Ghidelli, P. Gondoni, C.S. Casari, A. Li Bassi, Multi-wavelength Raman scattering of nanostructured Al-doped zinc oxide, J. Appl. Phys. 115 (2014). doi:10.1063/1.4866322.

[198] G.G. Miranda, R.L. de Sousa e Silva, H.V. dos Santos Pessoni, A. Franco, Raman spectroscopy study of Ga-doped ZnO ceramics: An estimative of the structural disorder degree, Phys. B Condens. Matter. 606 (2021) 1–6. doi:10.1016/j.physb.2020.412726.

[199] N.O. Korsunska, L.V. Borkovska, B.M. Bulakh, L.Y. Khomenkova, V.I. Kushnirenko, I.V. Markevich, The influence of defect drift in external electric field on green luminescence of ZnO single crystals, J. Lumin. 102–103 (2003) 733–736. doi:10.1016/S0022-2313(02)00634-8.

[200] J. Wang, L. Gao, Photoluminescence properties of nanocrystalline ZnO ceramics prepared by pressureless sintering and spark plasma sintering, J. Am. Ceram. Soc. 88 (2005) 1637–1639. doi:10.1111/j.1551-2916.2005.00259.x.

[201] W. Liu, L. Zhang, F. Kong, K. Wu, S. Li, J. Li, Enhanced voltage gradient and energy absorption capability in ZnO varistor ceramics by using nano-sized ZnO powders, J. Alloys Compd. 828 (2020) 154252. doi:10.1016/j.jallcom.2020.154252.

[202] C.L. Cramer, W. Li, Z.H. Jin, J. Wang, K. Ma, T.B. Holland, Techniques for Mitigating Thermal Fatigue Degradation, Controlling Efficiency, and Extending Lifetime in a ZnO Thermoelectric Using Grain Size Gradient FGMs, J. Electron. Mater. 47 (2018) 866–872. doi:10.1007/s11664-017-5879-9.

[203] S.G.M. Carvalho, E.N.S. Muccillo, R. Muccillo, AC Electric Field Assisted Pressureless Sintering Zirconia: 3 mol% Yttria Solid Electrolyte, Phys. Status Solidi Appl. Mater. Sci. 215 (2018) 1–5. doi:10.1002/pssa.201700647.

[204] L. Vayssieres, Growth of arrayed nanorods and nanowires of ZnO from aqueous solutions, Adv. Mater. 15 (2003) 464–466. doi:10.1002/adma.200390108.

[205] Q. Wan, Q.H. Li, Y.J. Chen, T.H. Wang, X.L. He, J.P. Li, C.L. Lin, Fabrication and ethanol sensing characteristics of ZnO nanowire gas sensors, Appl. Phys. Lett. 84 (2004) 3654–3656. doi:10.1063/1.1738932.

[206] P. Yang, H. Yan, S. Mao, R. Russo, J. Johnson, R. Saykally, N. Morris, J. Pham, R. He, H.J. Choi, Controlled growth of ZnO nanowires and their optical properties, Adv. Funct. Mater. 12 (2002) 323–331. doi:10.1002/1616-3028(20020517)12:5<323::AID-ADFM323>3.0.CO;2-G.

[207] B. Liu, H.C. Zeng, Hydrothermal synthesis of ZnO nanorods in the diameter regime of 50 nm, J. Am. Chem. Soc. 125 (2003) 4430–4431. doi:10.1021/ja0299452.

[208] J.-J. Wu, S.-C. Liu, Low-Temperature Growth of Well-Aligned ZnO Nanorods by Chemical Vapor Deposition, Adv. Mater. 14 (2002) 215–218. doi:10.1002/1521-4095(20020205)14:3<215::AID-ADMA215>3.0.CO;2-J.

[209] W.I. Park, D.H. Kim, S.W. Jung, G.C. Yi, Metalorganic vapor-phase epitaxial growth of vertically well-aligned ZnO nanorods, Appl. Phys. Lett. 80 (2002) 4232–4234. doi:10.1063/1.1482800.

[210] W. Wu, G. Hu, S. Cui, Y. Zhou, H. Wu, Epitaxy of vertical ZnO nanorod arrays on highly (001)-oriented ZnO seed monolayer by a hydrothermal route, Cryst. Growth Des. 8 (2008) 4014–4020. doi:10.1021/cg800210m.

[211] Q. Li, V. Kumar, Y. Li, H. Zhang, T.J. Marks, R.P.H. Chang, Fabrication of ZnO nanorods and nanotubes in aqueous solutions, Chem. Mater. 17 (2005) 1001–1006. doi:10.1021/cm048144q.

[212] Y.J. Xing, Z.H. Xi, Z.Q. Xue, X.D. Zhang, J.H. Song, R.M. Wang, J. Xu, Y. Song, S.L. Zhang, D.P. Yu, Optical properties of the ZnO nanotubes synthesized via vapor phase growth, Appl. Phys. Lett. 83 (2003) 1689–1691. doi:10.1063/1.1605808.

[213] Y. Ding, Z.L. Wang, Structures of planar defects in ZnO nanobelts and nanowires, Micron. 15 (2009) 1156–1157. doi:10.1017/S1431927609092290.

[214] P. Gao, Z.L. Wang, Self-assembled nanowire-nanoribbon junction arrays of ZnO, J. Phys. Chem. B. 106 (2002) 12653–12658. doi:10.1021/jp0265485.

[215] V. Khranovskyy, A.M. Glushenkov, Y. Chen, A. Khalid, H. Zhang, L. Hultman, B. Monemar, R. Yakimova, Crystal phase engineered quantum wells in ZnO nanowires, Nanotechnology. 24 (2013) 215202. doi:10.1088/0957-4484/24/21/215202.

[216] M.R. He, J. Zhu, Defect-dominated diameter dependence of fracture strength in single-crystalline ZnO nanowires: In situ experiments, Phys. Rev. B - Condens. Matter Mater. Phys. 83 (2011) 1–4. doi:10.1103/PhysRevB.83.161302.

[217] C. Geng, Y. Jiang, Y. Yao, X. Meng, J.A. Zapien, C.S. Lee, Y. Lifshitz, S.T. Lee, Well-Aligned ZnO Nanowire Arrays Fabricated on Silicon Substrates, Adv. Funct. Mater. 14 (2004) 589–594. doi:10.1002/adfm.200305074.

[218] Y.C. Kong, D.P. Yu, B. Zhang, W. Fang, S.Q. Feng, Ultraviolet-emitting ZnO nanowires synthesized by a physical vapor deposition approach, Appl. Phys. Lett. 78 (2001) 407–409. doi:10.1063/1.1342050.

[219] J.A. Downs, V.M. Sglavo, Electric field assisted sintering of cubic zirconia at 390°C, J. Am. Ceram. Soc. 96 (2013) 1342–1344. doi:10.1111/jace.12281.

[220] D. Bekermann, A. Gasparotto, D. Barreca, L. Bovo, A. Devi, R.A. Fischer, O.I. Lebedev, C. MacCato, E. Tondello, G. Van Tendeloo, Highly oriented ZnO nanorod arrays by a novel plasma chemical vapor deposition process, Cryst. Growth Des. 10 (2010) 2011–2018. doi:10.1021/cg1002012.

[221] H.P. Sun, X.Q. Pan, X.L. Du, Z.X. Mei, Z.Q. Zeng, Q.K. Xue, Microstructure and crystal defects in epitaxial ZnO film grown on Ga modified (0001) sapphire surface, Appl. Phys. Lett. 85 (2004) 4385–4387. doi:10.1063/1.1811393.

[222] M.-C.C. Jeong, S.-W.W. Lee, J.-M.M. Seo, J.-M.M. Myoung, The effect of stacking fault formation on optical properties in vertically aligned ZnO nanowires, Nanotechnology. 18 (2007) 305701. doi:10.1088/0957-4484/18/30/305701.

[223] A.B. Djurišić, Y.H. Leung, K.H. Tam, Y.F. Hsu, L. Ding, W.K. Ge, Y.C. Zhong, K.S. Wong, W.K. Chan, H.L. Tam, K.W. Cheah, W.M. Kwok, D.L. Phillips, Defect emissions in ZnO nanostructures, Nanotechnology. 18 (2007) 095702. doi:10.1088/0957-4484/18/9/095702.

[224] A.B. Djurišić, Y.H. Leung, K.H. Tam, L. Ding, W.K. Ge, H.Y. Chen, S. Gwo, Green, yellow, and orange defect emission from ZnO nanostructures: Influence of excitation wavelength, Appl. Phys. Lett. 88 (2006) 28–31. doi:10.1063/1.2182096.

[225] Y.H. Leung, A.B. Djurišić, Z.T. Liu, D. Li, M.H. Xie, W.K. Chan, Defect photoluminescence of ZnO nanorods synthesized by chemical methods, J. Phys. Chem. Solids. 69 (2008) 353–357. doi:10.1016/j.jpcs.2007.07.029.

[226] C. Chandrinou, N. Boukos, C. Stogios, A. Travlos, PL study of oxygen defect formation in ZnO nanorods, Microelectronics J. 40 (2009) 296–298. doi:10.1016/j.mejo.2008.07.024.

[227] S.A. Studenikin, N. Golego, M. Cocivera, Fabrication of green and orange photoluminescent, undoped ZnO films using spray pyrolysis, J. Appl. Phys. 84 (1998) 2287–2294. doi:10.1063/1.368295.

[228] C.H. Ahn, Y.Y. Kim, D.C. Kim, S.K. Mohanta, H.K. Cho, A comparative analysis of deep level emission in ZnO layers deposited by various methods, J. Appl. Phys. 105 (2009) 1–6. doi:10.1063/1.3054175.

[229] M.H. Huang, Y. Wu, H. Feick, N. Tran, E. Weber, P. Yang, Catalytic Growth of Zinc Oxide Nanowires by Vapor Transport, Adv. Mater. 13 (2001) 113–116. doi:10.1002/1521-4095(200101)13:2<113::AID-ADMA113>3.0.CO;2-H.

[230] S. Li, X. Zhang, B. Yan, T. Yu, Growth mechanism and diameter control of well-aligned small-diameter ZnO nanowire arrays synthesized by a catalyst-free thermal evaporation method, Nanotechnology. 20 (2009) 495604. doi:10.1088/0957-4484/20/49/495604.

[231] J. Li, L.L. Kerr, Thermodynamic modeling of native defects in ZnO, Opt. Mater. (Amst). 35 (2013) 1213–1217. doi:10.1016/j.optmat.2013.01.014.

[232] H. Charalambous, S.K. Jha, J.S. Okasinski, T. Tsakalakos, Generation of electric-field stabilized zirconium monoxide secondary phase within cubic zirconia, Scr. Mater. 190 (2021) 22–26. doi:10.1016/j.scriptamat.2020.08.026.

[233] D. Dey, R.C. Bradt, Grain Growth of ZnO during Bi2O3 Liquid-Phase Sintering, J. Am. Ceram. Soc. 75 (1992) 2529–2534. doi:10.1111/j.1151-2916.1992.tb05607.x.

[234] Y. Wu, P. Yang, Direct observation of vapor-liquid-solid nanowire growth, J. Am. Chem. Soc. 123 (2001) 3165–3166. doi:10.1021/ja0059084.

[235] M. Wei, D. Zhi, J.L. MacManus-Driscoll, Self-catalysed growth of zinc oxide nanowires, Nanotechnology. 16 (2005) 1364–1368. doi:10.1088/0957-4484/16/8/064.

[236] B.D. Yao, Y.F. Chan, N. Wang, Formation of ZnO nanostructures by a simple way of thermal evaporation, Appl. Phys. Lett. 81 (2002) 757–759. doi:10.1063/1.1495878.

[237] Y.K. Mishra, R. Adelung, ZnO tetrapod materials for functional applications, Mater. Today. 21 (2018) 631–651. doi:10.1016/j.mattod.2017.11.003.

[238] W.D. Yu, X.M. Li, X.D. Gao, Homogeneous-catalytic synthesis of tetrapodlike ZnO nanocrystals and their photoluminescence properties, Chem. Phys. Lett. 390 (2004) 296–300. doi:10.1016/j.cplett.2004.04.032.

[239] D.A. Grynko, A.N. Fedoryak, O.P. Dimitriev, A. Lin, R.B. Laghumavarapu, D.L. Huffaker, Growth of CdS nanowire crystals: Vapor-liquid-solid versus vapor-solid mechanisms, Surf. Coatings Technol. 230 (2013) 234–238. doi:10.1016/j.surfcoat.2013.06.058.

[240] R.L. Schwoebel, A diffusion model for filamentary crystal growth, J. Appl. Phys. 38 (1967) 1759–1765. doi:10.1063/1.1709757.

[241] S. Ambrosini, M. Fanetti, V. Grillo, A. Franciosi, S. Rubini, Vapor-liquid-solid and vapor-solid growth of self-catalyzed GaAs nanowires, AIP Adv. 1 (2011) 042142. doi:10.1063/1.3664133.

[242] C. Ferraro, E. Garcia-Tunon, S. Barg, M. Miranda, N. Ni, R. Bell, E. Saiz, SiC porous structures obtained with innovative shaping technologies, J. Eur. Ceram. Soc. 38 (2018) 823–835. doi:10.1016/j.jeurceramsoc.2017.09.048.

[243] K. Vanheusden, W.L. Warren, C.H. Seager, D.R. Tallant, J.A. Voigt, B.E. Gnade, Mechanisms behind green photoluminescence in ZnO phosphor powders, J. Appl. Phys. 79 (1996) 7983–7990. doi:10.1063/1.362349.

[244] X.L. Wu, G.G. Siu, C.L. Fu, H.C. Ong, Photouminescence and cathodoluminescence studies of stoichiometric and oxygen-deficient ZnO films, Appl. Phys. Lett. 78 (2001) 2285–2287. doi:10.1063/1.1361288.

[245] Y. Li, G.W. Meng, L.D. Zhang, F. Phillipp, Ordered semiconductor ZnO nanowire arrays and their photoluminescence properties, Appl. Phys. Lett. 76 (2000) 2011–2013. doi:10.1063/1.126238.

[246] W. Rheinheimer, M. Fülling, M.J. Hoffmann, Grain growth in weak electric fields in strontium titanate: Grain growth acceleration by defect redistribution, J. Eur. Ceram. Soc. 36 (2016) 2773–2780. doi:10.1016/j.jeurceramsoc.2016.04.033.

[247] Y. Dong, H. Wang, I.W. Chen, Electrical and hydrogen reduction enhances kinetics in doped zirconia and ceria: I. grain growth study, J. Am. Ceram. Soc. 100 (2017) 876–886. doi:10.1111/jace.14615.

[248] C. Wang, D. Wu, S. Grasso, T. Saunders, E. Castle, H. Yan, M.J. Reece, Growth of SiC platelets using contactless flash technique, J. Ceram. Soc. Japan. 124 (2016) 845–847. doi:10.2109/jcersj2.16160.

[249] T. Saunders, S. Grasso, M.J. Reece, Ultrafast-Contactless Flash Sintering using Plasma Electrodes, Sci. Rep. 6 (2016) 1–6. doi:10.1038/srep27222.

[250] V. Avila, R. Raj, Flash sintering of ceramic films: The influence of surface to volume ratio, J. Am. Ceram. Soc. 102 (2019) 3063–3069. doi:10.1111/jace.16298.

PUBLICATIONS

1. **X. L. Phuah,** B. Yang, H. Charlaambous, T. Tsakalakos, X. Zhang & H. Wang (2021), "Microstructure and defect gradients in DC and AC flash sintered ZnO", Ceramics International, in press.

2. **X. L. Phuah**, J. Jian, H. Wang, X. Wang, X. Zhang & H. Wang (2021), "Ultra-high heating rate effects on the sintering of ceramic nanoparticles: An in situ TEM study", Materials Research Letters, 9, 373-381.

3. **X. L. Phuah**, W. Rheinheimer, Akriti, L. Dou & H. Wang (2021), "Formation of liquid phase and growth of nanostructures during flash sintering of ZnO", Scripta Materialia, 195, 113719.

4. **X. L. Phuah**, J. Cho, T. Tsakalakos, A. K. Mukherjee, H. Wang & X. Zhang (2021), "Defects in flash-sintered ceramics and their impact on mechanical properties", MRS Bulletin, 46, 44-51.

5. W. Rheinheimer, **X. L. Phuah**, L. Porz, M. Scherer, J. Cho & H. Wang (2021), "The interplay of high heating rate sintering and plasticity: Does flash sintering involve plastic flow?" under review.

6. B. Yang, J. Cho, **X. L. Phuah**, H. Wang & X. Zhang (2021), "Flash sintering of additively manufactured 3YSZ gears", Journal of American Ceramic Society, 104, 3828-3832.

7. H. Charalambous, S. K. Jha, K.S.N. Vikrant, R. E. García, **X. L. Phuah**, H. Wang, H. Wang, A. Mukherjee & T. Tsakalakos (2021), "Electric field-induced grain boundary degradation mechanism in yttria stabilized zirconia", Scripta Materialia, 204, 114130.

8. J. Lu, R. Paldi, Y. Pachaury, D. Zhang, H. Wang, M. Kalaswad, X. Sun, J. Liu, **X. L. Phuah**, X. Zhang, A. A. El-Azab & H. Wang (2021), "Ordered hybrid metamaterial of $La_{0.7}Sr_{0.3}MnO_3$-Au vertically aligned nanocomposites achieved on templated $SrTiO_3$ substrate", Materials Today Nano, 100121.

9. R. Paldi, X. Sun, **X. L. Phuah**, J. Lu, X. Zhang & Haiyan Wang (2020), "Deposition pressure-induced microstructure control and plasmonic property tuning in hybrid ZnO-Ag_xAu_{1-x} thin films", Nanoscale Advances, 3, 2780-2878.

10. K. S. N. Vikrant, **X. L. Phuah**, J. Lund, H. Wang, C. S. Hellberg, N. Bernstein, W. Rheinheimer, C. M. Bishop, H. Wang, & R. E. García (2021). "Modeling of flash sintering of ionic ceramics", MRS Bulletin, 46, 67-75.

11. R. Paldi, Z. Qi, S. Misra, J. Lu, X. Sun, **X. L. Phuah**, M. Kalaswad, J. Bischoff, D. W. Branch, A. Siddiqui & Haiyan Wang (2020), "Nanocomposite-seeded epitaxial growth of single-domain lithium niobate thin films for surface acoustic wave devices", Advanced Photonics Research, 2000149.

12. **X. L. Phuah**, J. Cho, Akriti, L. Dou, W. Rheinheimer, R. E. García, X. Zhang & H. Wang (2020), "Field-assisted growth of one-dimensional ZnO nanostructures with high density defects", Nanotechnology, 32, 095603.

13. **X. L. Phuah**, H. Wang, B. Zhang, J. Cho, X. Zhang & H. Wang (2020), "Ceramic material processing towards future space habitat: Electric current-assisted sintering of lunar regolith simulant", Materials, 13, 4128.

14. **X. L. Phuah**, H. Wang, Z. Qi, S. Misra, M. Kalaswad & H. Wang (2020), "Field-assisted heating of Gd-doped ceria thin film", Journal of American Ceramic Society, 103, 2309-2314.

15. J. Cho, **X. L. Phuah**, J. Li, Z. Shang, H. Wang, H. Charalambous, T. Tsakalakos, A. K. Mukherjee, H. Wang & X. Zhang (2020), "Temperature effect on mechanical response of flash sintered ZnO by in-situ compression tests", Acta Materialia, 200, 699-709.

16. L. Su, S. K. Jha, **X. L. Phuah**, J. Xu, N. Nakamura, S. Zhang, H. Wang, J. S. Okasinski & B. Reeja-Jayan (2020), "Engineering lithium ion battery cathodes for high voltage applications using electromagnetic excitation", Journal of Materials Science, 55, 12177-12190.

17. D. Zhang, Z. Qi, J. Jian, J. Huang, **X. L. Phuah**, X. Zhang & H. Wang (2020), "Thermal stability of Au-BaTiO3 hybrid metamaterial via ex situ and in situ heating study", ACS Applied Nano Materials, 3(2), 1431-1437.

18. **X. L. Phuah**, H. Wang, H. Charalambous, S. K. Jha, T. Tsakalakos, X. Zhang & H. Wang (2019), "Comparison of the grain growth behavior and defect structures of flash sintered ZnO with and without controlled current ramp", Scripta Materialia, 162, 251-255.

19. H. Wang*, **X. L. Phuah***, H. Charalambous, S. K. Jha, J. Li, T. Tsakalakos, X. Zhang & H. Wang (2019), "Staged microstructural study of flash sintered titania", Materialia, 8, 100451.

20. S. K. Jha, N. Nakamura, S. Zhang, L. Su, **X. L. Phuah**, H. Wang, H. Wang, J. S. Okasinski, A. McGaughey & B. Reeja-Jayan (2019), "Defect-mediated anisotropic lattice expansion in ceramics as evidence for non-thermal coupling between electromagnetic fields and matter", Advanced Engineering Materials, 21(12), 1900762.

21. J. Huang, X. Wang, **X. L. Phuah**, P. Lu, Z. Qi & H. Wang (2019), "Plasmonic Cu nanostructures in ZnO as hyperbolic metamaterial thin films", Materials Today Nano, 8, 100052.

22. J. Li, J. Cho, J. Ding, H. Charalambous, S. Xue, H. Wang, **X. L. Phuah**, J. Jian, X. Wang, C. Ophus, T. Tsakalakos, R. E. García, A. Mukherjee, N. Bernstein, C. S. Hellberg, H. Wang & X. Zhang (2019), "Nanoscale stacking-fault-assisted room temperature plasticity in flash-sintered TiO_2", Science Advances, 9 (5).

23. W. Rheinheimer, **X. L. Phuah**, H. Wang, F. Lemke, M. J. Hoffmann & H. Wang (2019), "The role of point defects and defect gradients in flash sintering of perovskite oxides", Acta Materialia, 165, 398-408.

24. H. Wang, **X. L. Phuah**, J. Li, T. B. Holland, K.S.N. Vikrant, Q. Li, C. S. Hellberg, N. Bernstein, R. E. García, A. Mukherjee, X. Zhang & H. Wang (2019), "Key microstructural characteristics in flash sintered 3YSZ critical for enhanced sintering process", Ceramics International, 45, 1251-1257.

25. S. K. Jha, **X. L. Phuah**, J. Luo, C. P. Grigoropoulos, H. Wang, R. E. García & B. Reeja-Jayan (2018), "The effects of external fields in ceramic processing", Journal of American Ceramic Society, 102, 5-31.

26. H. Charalambous, S.K. Jha, **X. L. Phuah**, H. Wang, H. Wang, J. Okasinski & T. Tsakalakos (2018), "In situ measurement of temperature and reduction of rutile titania using energy dispersive x-ray diffraction", Journal of European Ceramics Society, 38, 5503-5511.

27. H. Charalambous, S. K. Jha, H. Wang, **X. L. Phuah**, H. Wang & T. Tsakalakos (2018), "Inhomogeneous reduction and its relation to grain growth of titania during flash sintering", Scripta Materialia, 155, 37-40.

28. S. K. Jha, H. Charalambous, C. Meade, H. Wang, **X. L. Phuah**, J. Okasinski, H. Wang & T. Tsakalakos (2018), "In situ observation of oxygen mobility and abnormal lattice expansion in ceria during flash sintering", Ceramics International, 44, 15362-15369.

29. A. D. Dysart, **X. L. Phuah**, L. K. Shrestha, K. Ariga & V. G. Pol (2018), "Room and elevated temperature lithium-ion storage in structurally tailored submicron carbon spheres with mechanistic elucidation", Carbon, 134, 334-344.

30. A. E. Brenner, A. A. Peña, **X. L. Phuah**, C. Petorak, B. Thompson & R. W. Trice (2017), "Cyclic ablation of high-emissivity Sm-doped ZrB_2/SiC coatings on alumina substrates", Journal of European Ceramic Society, 38, 1137-1142.

31. A. A. Alazemi, A. D. Dysart, **X. L. Phuah**, V. G. Pol & F. Sadeghi (2016), "MoS_2 nanolayer coated carbon spheres as an oil additive for enhanced tribological performance", Carbon, 110, 367-377.

* equal contribution